AD_____

Award Number: DAMD17-96-1-6139

TITLE: X-Photon-to-Information Conversion Efficiency in Digital Telemammography

PRINCIPAL INVESTIGATOR: Bradley D. Clymer, Ph.D.
Celeste B. Williams

CONTRACTING ORGANIZATION: The Ohio State University
Research Foundation
Columbus, Ohio 43210-1063

REPORT DATE: December 2000

TYPE OF REPORT: Final

PREPARED FOR: U.S. Army Medical Research and Materiel Command
Fort Detrick, Maryland 21702-5012

REPORT DOCUMENTATION PAGE

Form Approved
OMB No. 074-0188

1. AGENCY USE ONLY (Leave blank)	2. REPORT DATE	3. REPORT TYPE AND DATES COVERED
	December 2000	Final (1 Jun 96 - 30 Nov 00)

4. TITLE AND SUBTITLE
X-Photon-to-Information Conversion Efficiency in Digital Telemammography

5. FUNDING NUMBERS
DAMD17-96-1-6139

6. AUTHOR(S)
Bradley D. Clymer, Ph.D.
Celeste B. Williams

7. PERFORMING ORGANIZATION NAME(S) AND ADDRESS(ES)
The Ohio State University Research Foundation
Columbus, Ohio 43210-1063

E-MAIL:
clymer.1@osu.edu

8. PERFORMING ORGANIZATION REPORT NUMBER

9. SPONSORING / MONITORING AGENCY NAME(S) AND ADDRESS(ES)
U.S. Army Medical Research and Materiel Command
Fort Detrick, Maryland 21702-5012

10. SPONSORING / MONITORING AGENCY REPORT NUMBER

11. SUPPLEMENTARY NOTES

12a. DISTRIBUTION / AVAILABILITY STATEMENT
Approved for public release; distribution unlimited

12b. DISTRIBUTION CODE

13. ABSTRACT *(Maximum 200 Words)*

Imaging techniques used for diagnosis and detection of breast cancer are all performed by deforming the breast. This deformation permits improved diagnostic imaging of the breast, however, the imaging techniques do not take into account the biomechanical nature of breast tissue. This is largely due to the fact that the biomechanical behavior of breast tissue is not fully understood. Since malignant masses tend to be stiffer than normal tissue, an understanding of the normal and pathological biomechanical nature of breast tissue may provide more accurate discrimination of breast masses. Also, an understanding of the biomechanical properties of breast tissue may be used to develop more accurate breast models.

The purpose of our study was to noninvasively characterize the *in vivo* force-deformation behavior of normal breast tissue under static compressive loads, with the aim of performing finite element computer simulations of tissue deformations. We present a new method to obtain *in vivo* deformation data by using magnetic resonance imaging to detect displacement. With small incremental compressions, corresponding displacement can be easily mapped between deformed (compressed) and undeformed (uncompressed) images. Material properties of breast tissue were evaluated by fitting the uniaxial compression data to various constitutive SEDF models.

14. SUBJECT TERMS
Breast Cancer

15. NUMBER OF PAGES
209

16. PRICE CODE

17. SECURITY CLASSIFICATION OF REPORT	18. SECURITY CLASSIFICATION OF THIS PAGE	19. SECURITY CLASSIFICATION OF ABSTRACT	20. LIMITATION OF ABSTRACT
Unclassified	Unclassified	Unclassified	Unlimited

Table of Contents

THE BIOMECHANICS OF NORMAL BREAST TISSUE

DISSERTATION

Presented in Partial Fulfillment of the Requirements for

the Degree Doctor of Philosophy in the Graduate

School of The Ohio State University

By

Celeste Benay Williams B.S., M.S.

*****

The Ohio State University
2000

Dissertation Examination Committee:

Professor Bradley Clymer, Advisor

Professor Petra Schmalbrock

Professor Somnath Ghosh

Approved by

_____

Advisor
Biomedical Engineering Graduate
Program

ABSTRACT

Early detection and diagnosis of breast cancer can result in improved long-term survival and fewer deaths through more effective and less traumatic treatment. Presently, the imaging techniques used for diagnosis and detection of breast cancer are all performed by deforming the breast from its original shape. The deformation employed by such imaging techniques permit improved diagnostic imaging of the breast, however, the imaging techniques do not take into account the biomechanical nature of breast tissue. This is largely due to the fact that the biomechanical behavior of breast tissue is not fully understood, and no standard *in vivo* or *in vitro* testing of soft tissue exists. Since malignant masses tend to be stiffer than normal tissue, an understanding of the normal and pathological biomechanical nature of breast tissue may provide more accurate discrimination of breast masses (*e.g.*, elastography). Also, an understanding of the biomechanical properties of breast tissue may be used to develop more accurate breast models. Biomechanically-based models can be used to develop computer algorithms to accurately mimic the deformation of breast tissue undergoing external forces typically

generated during diagnosis procedures. Such models will better aid in surgical biopsies, breast conservation procedures, and may improve the prognosis for breast cancer patients.

The purpose of our study was to noninvasively characterize the *in vivo* force-deformation behavior of normal breast tissue under static compressive loads, with the aim of performing finite element computer simulations of tissue deformations. We present a new method to obtain *in vivo* deformation data by using magnetic resonance imaging to detect displacement. With small incremental compressions, corresponding displacement could be easily mapped between deformed (compressed) and undeformed (uncompressed) images. Material properties of breast tissue were evaluated by fitting the uniaxial compression data to various constitutive models.

The initial investigation into the mechanical behavior of normal breast tissue shows that under static compressive loading, breast tissue exhibits nonlinear properties similar to other soft tissues. The constitutive relationships most suitable for uniaxial test data of breast tissue are large-elastic deformation and incompressible models, such as Mooney-Rivlin and Blatz, with the Mooney-Rivlin model providing the best fit to varying tissue densities.

DEDICATED

WITH HIGHEST PRAISE, TO A MERCIFUL SAVIOR

WITH LOVE, TO WONDERFUL PARENTS

WITH GRATITIDUE, TO CARING FAMILY AND FRIENDS

AND WITH UTMOST RESPECT, TO A WISE AND STRONG FRIEND,

MY MOTHER.

ACKNOWLEDGEMENTS

I wish to thank my advisors Professors Bradley Clymer and Petra Schmalbrock, for taking on a graduate student in mid-program and guiding me on with encouragement. I did not think that I would be able to find a mentor at OSU, but instead I found two very creative, innovative and extremely challenging mentors.

I thank Dr. Morton Friedman for his guidance and support during the upheaval in the Biomedical Engineering department. I thank Dr. Manula Waldron for teaching me to think like a biomedical engineer.

I wish to thank Professor Somanath Ghosh for graciously agreeing to sit on my committee and for his insight into biomechanics.

I thank Dr. Greg Washington, Dr. Kikuo Fujimura, Don Streadley, Dennis Sessena, and Jim Guliani for their help and support of my research work. The team at the Ohio Supercomputing Center are the best. I am grateful for the computer time afforded me by Don Streadley.

Again I must acknowledge and thank my parents for their love, support and faith.

This research was supported by the Department of Defense Breast Cancer Research award # DAMD17-96-1-6139.

VITA

Born in Jefferson County, Birmingham, Alabama on August, 27. Attended Lincoln Elementary and A.H. Parker High School.

EDUCATION

M.S., Electrical Engineering, Auburn University, Auburn, AL
GPA 3.45/4.0

Thesis research, "*A Study of the Nature and Characteristics of Light Radiation in Reverse-Biased Silicon PN Junctions*"

B.S., Physics, Auburn University, Auburn, AL
GPA 3.47/4.0

Graduated with honors.

PUBLICATIONS/PRESENTATIONS

1. Williams, C., Clymer, B., Schmalbrock, P., "*Biomechanics of Normal Breast Tissue: Preliminary study of in vivo force-deformation relationship*" ,submitted to Journal of Biomechanics, June 2000.

2. Williams, C., Clymer, B., Schmalbrock, P., "*Biomechanics of Normal Breast Tissue: Preliminary study of in vivo force-deformation relationship*", Poster at DoD Era of Hope Breast Cancer Conference, June 2000.

3. Williams, C., Clymer, B., Schmalbrock, P., "*Biomechanics of Breast Tissue: Tissue deformation and visualization*", Presentation at 1999 Proceedings of 70th Scientific Meeting and Exhibition of the International Society for Magnetic Resonance in Medicine, May 1999.

4. Chakeres, D., Schmalbrock, P., Clymer, B., Deak, G., Williams, C., "*MR Surface Coil Image*

Correction Using an Integrated Positional Reference System", 84th Scientific Assembly and Annual Meeting of the Radiological Society of North America, p.516, 1998.

5. Williams, C., Clymer, B., Fujimura, K., Schmalbrock, P., "*Preliminary Study of Shape Deformation of Normal Breast Tissue*", ", Poster at 84th Scientific Assembly and Annual Meeting of the Radiological Society of North America, p.524, April 1998.

6. Williams, C., Clymer, B., Fujimura, K., Schmalbrock, P., "*Preliminary Study of Shape Deformation of Normal Breast Tissue*", Presentation at 1998 Annual Fall Meeting of the Biomedical Engineering Society, October 1998.

7. Williams, C., Clymer, B., Schmalbrock, P., "*Preliminary Study of Shape Deformation of Normal Breast Tissue*", Poster at Women's Health Conference, The Ohio State University, 1997.

8. Williams, C., Danschevar, K., *"Characterization of Reverse-Biased Silicon PN Junctions"*, Presentation at Proceedings of IEEE Southeastern Conference, 1988.

9. Williams, C., "*Study of DLTS on Irradiated Devices*", Universal Energy Systems, 1988.

TABLE OF CONTENTS

LIST OF TABLES

LIST OF FIGURES

CHAPTER 1

INTRODUCTION

Breast examination is an important procedure because breast cancer is the leading cause of death by cancer in women less than 50 years of age [Fentiman, 98]. The incidence of breast cancer has increased in many western countries in the last ten years. It is estimated that nearly one in twelve women will develop breast cancer at some point in their lives [Dixon, 1998]. Because the disease is not associated with manifest signs or symptoms when it is minimal and localized, and there is no current cure, mass screenings for asymptomatic women are recommended for early detection. Although mass screening, as well as the criteria for screening, are still debated [Watmough, 97], screening mammography is widely accepted as an effective means for decreasing breast cancer mortality. The malignancy potential of breast cancer varies considerably from patient to patient. Hence, prognosis depends on a variety of conditions such as genetic makeup of the cancer, and initial detection cancer stage. The detection of early stage or primary cancer refers to detection of lesions less than 1cm and without axillary node invasion.

Local primary cancer has a better prognosis than invasive metastatic cancer. The prognosis is associated with the presence or absence of metatastic cancer in the axillary lymph nodes at the time of diagnosis [Eisenberg, 1989]. Early detection, diagnosis, and prognosis of breast cancer can result in improved long term survival and fewer deaths through more effective and less traumatic treatment.

Presently, the imaging techniques used for diagnosis and detection of breast cancer are all performed by deforming the breast from its original shape. The deformation employed by such imaging techniques permits improved diagnostic imaging of the breast, however, the imaging techniques do not take into account the biomechanical nature of breast tissue. This is largely because the biomechanical behavior of breast tissue is not fully understood, and no standard *in vivo* or *in vitro* testing of soft tissue exists. Since malignant masses tend to be harder than benign masses on palpation, an understanding of the normal and pathological biomechanical nature of breast tissue may provide more accurate discrimination of breast masses. Also, an understanding of the biomechanical properties of breast tissue may be used to develop more accurate breast models. Such biomechanically-based models can be used to develop computer algorithms so that the initial images obtained by shape deformation can be transformed into images that represent the breast in an undeformed state. Such images will better aid in surgical biopsies and breast conservation procedures, and may improve the prognosis for breast cancer patients.

The purpose of our work is to noninvasively study with MRI and characterize the mechanical properties of normal breast tissue by examining the stress-strain relationship. This dissertation describes investigations into the *in vivo* displacement and force-deformation relationship of normal breast tissue undergoing mild compressive forces under static loading conditions similar to those used in mammography.

1.1 SIGNIFICANCE

The information gained from the understanding of biomechanical behavior of *in vivo* tissue may serve as a diagnostic tool in surgery planning, computer aided diagnosis, and mammographic compression by making better breast models. Such models may be useful for predictive computer simulations of tissue displacement, assessing tissue changes in serial mammograms, and aiding elastography (i.e., remote palpation).

1.2 ORGANIZATION OF THESIS

Chapters two and three provide a detailed background for the foundation of the research work. The anatomy of the human breast and diagnosis and treatment of breast cancer is discussed in chapter two. Chapter three gives a brief description of the general mechanics, mechanical properties of materials and how the principles are applied to biological tissues.

Chapters four, five and six describe the experimental procedures and analysis of the research work. Instead of the body of the text being divided up in the such subsections as methods, results and discussions, each chapter describes specific and separate experiments, with each chapter presenting the introduction, methods, results and discussion of the experiments. Chapter four describes the breast magnetic resonance imaging (MRI), deformation, and tissue displacements studies. Studies on force analysis, strain and the constitutive relationships of soft tissue are discussed in Chapter five. Chapter six is abut the investigation into computer simulation of deformation and describes the morphing and finite element analysis. Chapter seven provides an overall analysis of the research work.

CHAPTER 2

BASIC UNDERSTANDING OF BREAST TISSUE AND BREAST EXAMINATION

2.1 Anatomy of the Breast

The shape of the breast varies from female to female, with the left breast being typically larger that the right. The breast shape is hemispheric in adult women and becomes more pendulous with age. The breast is located in the superficial fascia between the second rib and sixth intercostal cartilage, and it is superficial to the major pectoralis muscle [Lawrence, 1999]. The breast is a composite of mechanically different materials. The normal breast is composed of glandular tissue, supportive connective fibrous tissue, and adipose tissue. A simplified diagram of the anatomy of the breast is shown in figure 2.1

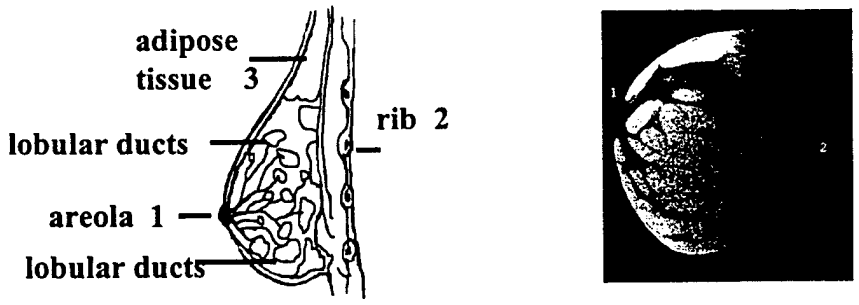

(a) (b)

Figure 2.1: Comparison of (a) Schematic of breast anatomy; with (b) Sagittal MR image. Dark regions are glandular tissue, and the bright regions are adipose tissue. 1 is in the areola and nipple region; 2 shows where the rib is located; 3 in the region of adipose tissue.

The breast can be divided into three major structures. These are the skin, subcutaneous tissue and corpus mammae. The corpus mammae is the breast mass that remains after removing the skin, connective tissue and the deep attachments [Lawrence, 1999]. Cooper's ligaments are such attachments. These ligaments are triangularly shaped and stretch between the mammary gland, skin, and pectineal ligament. On radiograph images, the elastic ligaments appear as a honeycomb-like lattice structure around which variable amounts of adipose and glandular tissues are enclosed.

The corpus mammae can be divided into the parenchyma and the stroma. The parenchyma includes the duct lobular units, which are the tree-like branching structures in which the ducts terminate into clusters of glandular sacs known as lobules, (see figure

2.1). Each ductal unit is embedded in adipose tissue and drains into the areola. The structural arrangements consist of 12-18 major duct lobular systems branching from the areola. The lobes are separated by connective tissue structures that attach to the skin, (*i.e.*, Cooper's ligaments). The ductal system comprises about 10-15% of the total breast mass. The remaining 85% is mostly adipose tissue. The adipose tissue is essential for the proliferation and differentiation of the mammary epithelium by providing the space, support and control for elongation of ducts [Lawrence, 1999]. It was thought that each major duct was autonomous with no communication between them, but some have reported that there appears to be some interaction [Cardenosa, 1995]. Since the branching structures are not a true radial pattern, the branching from the nipple is both unpredictable and irregular. Thus, it is not possible to isolate a single duct. As the ducts branch and become smaller, the epithelium becomes a single layer of cells. In the smaller ducts and terminal glands, there is a low flattened layer of cells called myoepithelial cells. Cancer tends to develop in these ductal cellular regions [Cardenosa, 1995].

The stroma includes the connective tissue, adipose tissue, blood vessels, lymphatics, and nerves. The areola is the darkly pigmented area surrounding the nipple and its size can increase during pregnancy. The edges of the areola are slightly elevated due to the 15-20 openings of the ducts of Montgomery glands. Subcutaneous tissues around the nipple contain smooth muscle, and contraction of the smooth muscle induces occlusion of the duct openings and erection of the nipple.

The histology of the breast changes with age. In postmenopausal women, glandular and fibrous tissues degenerate and the amount of adipose tissue increases. The terminal glands may almost totally disappear in postmenopausal women. The influence of hormonal variations changes the histology of the breast. For example, when estrogen hormone levels are high, the duct epithelium actively grows (proliferates) and the ducts become dilated and increase in tissue mass [Lawrence, 1999]. Because of the changes in breast structure, the mechanical properties of the breast should be expected to vary between post and premenopausal women.

2.2 **Breast Disease and Malignancies**

Fibrocystic disease is a very common disease of the breast. This disease may involve the overgrowth of the fibrous stroma and abnormal epithelial growth. The disease is accompanied by formation of cysts and /or duct epithelial hyperplasia. That is, an increase in the number of constituent cells causes an increase of tissue mass in the duct epithelium. When seen in this form, such abnormal tissue growth is benign growth rather than malignant, however the masses may appear on mammograms. On the other hand, a variant of fibrocystic disease called epithelial hyperplasia is often an antecedent to breast cancer. True epithelial hyperplasia affects the lining of the ducts [Slauson, 1990]. It is considered to be the histologic variant of a form of fibrocystic disease that increases the risk of the subsequent development of cancer [Slauson,1990]. Since not all epithelial

hyperplasias are malignant, it is difficult for conventional mammography to distinguish between the benign growths and malignant lesions.

Another common benign condition is fibroadenoma, which is a growth made up of both glandular and fibrous tissues. Fibroadenoma, which develops from a whole lobule, grows from a small nodule and can reach up to 15 cm in diameter. These growths are encapsulated and are freely movable from the surrounding breast substance. Approximately 12% of all palpable breast masses are fibroadenomas [Dixon, 1998]. Fibroadenomas may be diagnosed and separated from cancer, however fibroadenomas should not always be left alone and disregarded because they are benign. Fibroadenomas should be closely watched because they can grow extremely large. Usually if fibroadenomas are found, mammograms are recommended to be taken every six to twelve months [Cardensoa, 1995, Dixon, 1998].

Many benign breast lesions are in the lobules. For example, cysts are caused by the dilation and fusion of adjacent lobules into a fluid-filled pocket. Also, proliferating lobes can form adenosis tumors [Cardenosa, 1995].

Carcinoma of the breast implies a malignancy arising in the glandular regions and the duct epithelium of the breast. Malignant lesions are seen as distortions of the normal

ductal structural patterns and they point away from the nipple. Over 85% of breast malignancies arise in the ducts [Slauson 1990, Dixon 1998].

Ductal carcinomas are divided into two classes: 1) noninfiltrating (intra ductal) carcinomas, and 2) infiltrating carcinomas. The occurrence of DCIS (ductal carcinoma *in situ*) began to increase in the early 1980's. It is found nearly 12% of the time among women ages 30 to 39. By 1992, DCIS was routinely treated by mastectomy or lumpectomy [Dixon,1998].

Lobular carcinoma is a relatively distinct morphological form of breast cancer that arises in the terminal ductals of the breast lobule. These lesions are distinct from other carcinomas of the breast in that they originate in the terminal acini (glands), and unlike DCIS, lobular carcinoma tends to occur in pure form [Dixon, 1998, Slauson,1990].

2.2.1 Genetic Basis of Breast Cancer

Although it is impossible to predict who will develop breast cancer, diagnosis and breast cancer prognosis depend on the genetic makeup of the cancer that is being treated. Transformed cells of malignancies possess the ability to proliferate in an unrestrained manner. Such cells also possess the ability to overexpress, or secrete, their own endogenous growth factors. Growth factors are cellular messengers which signal to cells

that it is time to divide. Some growth factors which normal and malignant cells respond to are epidermal growth factor, EGF, fibroblast growth factor, FGF, and transforming growth factor alpha, TGFA [Callahan, 1990]. Growth factors act as oncogenes, which when activated, signal uncontrolled cell proliferation.

The Her-2/Neu oncogene is amplified in some 10% to 40% of primary breast cancers. Such cancers show a high resistance to chemotherapy. The gene amplification results in the overexpression of the protein product, tyrosine kinase. Tyrosine kinase is a secondary messenger in the proliferation signal pathway and the overexpression of this protein leads to uncontrolled cell division and growth. The Her-2/Neu oncogene amplification is not seen in germline DNA, (*i.e.*, the mutation is not hereditary) [Callahan, 1990].

Familial breast cancers occur in cancer-prone families due to germline mutations of the P53 gene. This leads to the inactivation of the tumor suppressor gene, P53. The expressed protein product of P53 is a transcription factor. Tumor suppressor genes (TSG) normally produce proteins that restrain cell division. When a TSG is lost or mutated, the control that it had on cell growth is lost. This can trigger uncontrolled cell divisions and lead to cancer [Callahan, 1990].

Many tumors express antigens that are recognized by T-cells, but are not found on normal cells. The antigens are called tumor specific antigens, TSA or tumor associated antigens, TAA. These T-antigens represent an altered T-antigen to the host immune system. The host immune system will only attack the antigens that it recognizes as foreign. Not all of the altered T-antigens will cause an immunocytoxic reaction. There is a need, therefore, not only to identify the TAA, but also to find a way of presenting them to the immune system [Callahan, 1990].

Cancers not clearly distinguished by mammography, may be characterized using new approaches and targets in the diagnosis, prognosis and treatment of breast cancer. Quantitative or qualitative differences in the level of expression of growth factors, growth factor receptors, specific intracellular signal transduction proteins, and T-antigens can potentially be used as diagnostic and prognostic markers for various stages of breast cancer.

2.2.2 Cancer Growth Pattern

The uncontrolled growth pattern of fibrous tissue initiated by transformed epithelial cells in the breast is what causes malignant lesions to have a dense hard consistency. Generally, a malignancy grows in the direction of least mechanical resistance [Chen *et al.*, 1995]. When the surrounding tissue is firm and dense, such as

glandular tissue, tumors cells tend to grow in the clefts between the fibrous regions and ductal carcinoma develops [Chen *et al.*, 1995, Slauson, 1990]. Physical signs of malignancy involve asymmetry between left and right breast, and skin or nipple changes. Other signs include deposits of micro-calcifications, and dense masses of spiculated or stellate tissue.

The calcific deposits are seen as small clustered grains irregular in size, shape and density, and are positioned toward the nipple. For breast cancer detection, calcifications, often significantly less than one millimeter in size, are of great importance [Bassett, 1995]. The presence of stellate and spiculated masses is one of the most distinct mammographic characteristics of breast malignancy, however mammography still cannot differentiate well between benign and malignant lesions.

It is well known that malignancies have different mechanical properties than normal tissue. The fact that malignant masses tend to be harder than normal tissue is the basis for detection by palpation. An understanding of the normal and pathological biomechanical nature of breast tissue may provide more accurate discrimination of breast masses [Chen *et al*, 1995, Fowlkes *et al*, 1995, Garra *et al*, 1997]. Tissue hardness approximates the tissue shear (Young's) elastic modulus, and the modulus differs between normal tissue and malignant lesions [Chen, 1995, Fowlkes,1995, Garra, 1997]. Manual palpation is successful in detecting large (>10 cm) lesions as well as lesions that

are close to the surface. Therefore breast self examinations (BSE) are strongly recommended by the American College of Radiology (ACR) and the National Cancer Institute (NCI). However, for deep, small lesions, some type of imaging modality is required for detection.

2.3 **Detection of Breast Cancer (Imaging)**

Patient prognosis is greatly improved by early detection and diagnosis of breast cancer. The mortality rate can also be reduced by early detection [Simonetti, 1998]. Conventional x-ray mammography is currently the imaging modality used for soft tissue radiographic diagnosis of breast malignancies. Mammography has been reported to reduce breast cancer mortality by about 30% in women older that 50 years and by 17% in women in the age group 40 to 50 years [Dixon, 1998]. Although the value of mammography is often assessed differently by radiologists, internists and surgeons, it is presently the most sensitive, cost-effective and noninvasive way to detect nonpalpable malignancies in the breast. Likewise, advances in screen-film systems and compressions have reduced the radiation exposure risks and improved quality of mammography.

2.3.1 Standard X ray Mammography

In mammography, the breast is positioned between two plates and compressed while being exposed to ionizing radiation. Mammography has high sensitivity for detecting malignant lesions less than 1 cm. However the modality is not perfect. The modality has a sensitivity of 88%, but about 75% of mammographically detected lesions are not malignant [Harms, 1999]. Most detection schemes attempt to detect masses and microcalcifications. Typical breast cancer screenings and diagnosis follow the procedures outlined in figure 2.2. There are many steps in the diagnosis and treatment of a mass or lesion found on a mammogram. Indeterminate lesions are examined with ultrasound and if they are still suspicious, various biopsy procedures, such as core and fine needle aspiration are recommended.

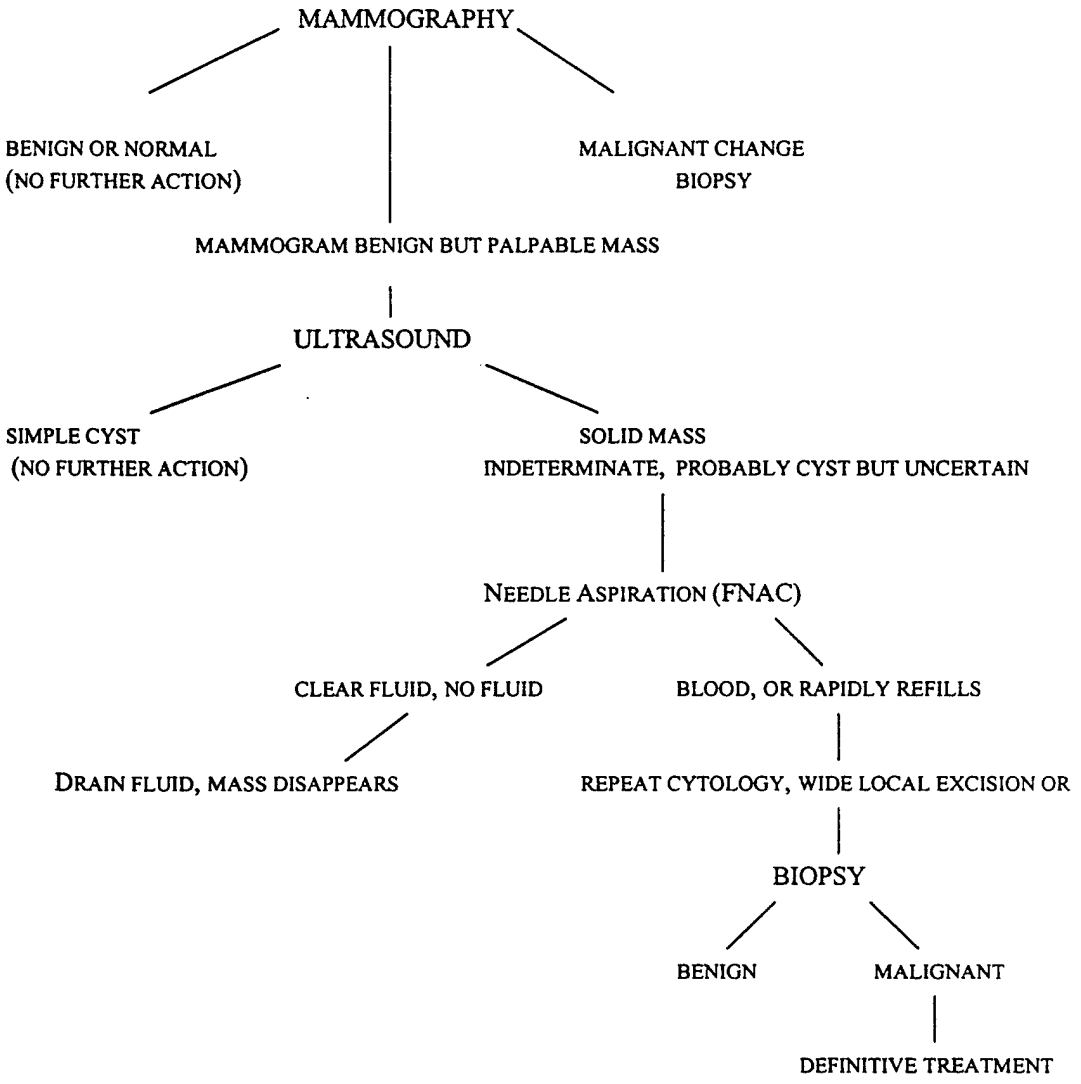

Figure 2.2 Schematic diagram for conventional detection and diagnosis of lesion. As shown in the diagram, if a mass is not distinguishable as a cyst, biopsies (either Core or FNAC) are recommended.

2.3.1.1 Equipment

In conventional radiography, screen-film techniques are employed to enhance differential absorption of the x-ray beam in the similar tissues in the breast and to lower patient dose. Such technical advances have lead to a reduction in radiation risks with the total glandular dose never exceeding 4 mGy. A dose of less than 1 mGy is standard. In order to image small density differences in soft tissue and obtain maximum contrast, low kVp x-rays ranging from 25 – 27 kVp are used along with scatter reduction grids [Bassett, 1995]. With high contrast, attenuation differences between breast tissues are readily viewed on radiographic images. Glandular tissues are displayed as white to light gray, and adipose tissue is seen as black to dark gray. To evaluate breast lesions and increase image quality, each breast is compressed in the cranial-caudal (CC) and oblique medial-lateral (MLO) orientations. Such views give information about the density and location of lesions.

2.3.1.2 Compression and Positioning

Positioning of the breast varies according to the diagnostic (two views or three views, screening or biopsy) and imaging modality requirements. But over the years, with a better understanding of breast tissue, breast positioning has evolved to image as much of the breast tissue as possible. On the CC views of the breast tissue, all of the posteromedial tissue should be included and the retroglandular fat should outline the

breast tissue [Cardenosa, 1995, Bassett, 1995]. Also the nipple should be located at the midline of the image. The retroglandular fat region is seen as a dark region at the posterior edge of the radiographic image. In some cases, the pectoral muscle is seen as a white crescent shaped region posterior to the retroglandular fat in CC views. The pectoral muscle is often not seen on images of older women because of muscle atrophy [Cardenosa, 1995].

Since the breast is attached to the pectoral muscle, the muscle is readily seen on MLO images as a convex density (*i.e.*, dense white region) extending from the top of the image to the level of the nipple or below it. With appropriate positioning, a perpendicular line should extend from the pectoral muscle to the nipple [Bassett, 1995]. A well positioned MLO view is able to show nearly all of the breast tissue. Observation of the retroglandular fat indicates that all of the fibroglandular tissue is included in the image. The MLO and CC views should complement each other with as much tissue as possible being included in the images. Repositioning and exaggerated views should be done if initial views indicate more axillary tissue is present.

Another technique employed to improve image quality and contrast in mammography is compression of the breast. Compression decreases tissue thickness, separates the overlapping structures and increases lesion detection. The uniform thickness obtained by compression allows the exposure of the entire breast on a single

image, and reduces the radiation absorbed by breast tissue; thereby reducing the radiation dose as well as radiation scatter. The amount of compressive force can range from 49 N to 186 N, with breast thickness ranging from 10 mm to 88 mm after compression [Sullivan 1991]. The compression lasts for about six seconds [Eklund, 1995]. The American College of Radiology recommends that maximum compression force be no greater than 200 N (45 lbs) [Sullivan, 1991]. Inadequate mammographic positioning can contribute to discomfort during compression. With conventional positioning, the compression paddle is controlled and brought down over breast. Either the maximum available force is applied at once (with a loading rate of about 33 N/sec) or the technologist applies the force until the breast is compressed to an adequate amount [Sullivan 91]. Compressive forces are routinely used without much emphasis given to the mechanical behavior of a compressed breast.

2.3.1.3 Sensitivity

Although mass screening of breast cancer has been introduced in most western countries, distinguishable differences exist between the number of projections, length of intervals, and age requirement. However, there is agreement that mammography is never used in routine screening of women less than 35 years of age. Breast tissue tends to be

very dense in younger women. The ionizing radiation in mammography is carcinogenic and it is often necessary to increase the effective x-ray beam energies in order to penetrate denser breast tissue.

It has been reported that fatty (radiolucent) tissue has a lower risk for cancer development than dense glandular tissue [Wolfe, 1976, Boyd, 1998]. However, it is possible for tumor abnormalities to be present in such dense tissue without being detected with conventional mammography. Thus, a different detection modality, usually ultrasound, is typically employed to image dense breast tissue.

Standard mammography is known to have several major limitations. Approximately 15% to 20% of breast malignancies are not detected with conventional mammography [Harms, 1999]. Other limitations of X ray mammography are that: 1) it offers little opportunity for image processing of acquired images; 2) it does not give adequate information for imaging in patients with thick or dense breast tissue, 3) it has a low positive predictive value (PPV), ranging from 15% to 30%, and 4) it cannot distinguish with absolute certainty between benign and malignant lesions [Harms, 1998].

2.3.2 Computer Aided Diagnosis

To aid with evaluation of mammographic abnormalities and to increase specificity, several techniques have been developed which classify the abnormalities by architectural patterns and appearance [Kopans 1995, Gram 1997]. Computer aided diagnosis (CAD) was introduced into clinical practice in 1995, and has helped to improve evaluation of mammograms by increasing specificity [Simonetti, 98]. Radiologists use CAD to enhance their interpretation of mammograms, so that CAD provides a second interpretation of mammograms. CAD is reported to increase the sensitivity of mammograms from 89% to 100% [Simonetti, 1998].

CAD is an indirect digitalization method in which digital images are generated by digitizing conventional film mammograms. The digital images are then analyzed for masses and calcifications on a dedicated workstation. A high resolution scanner or charge coupled device (CCD) is used to digitize the film of a breast image. In the CCD system, large-area phosphor screens are coupled to small-area photodetectors with enough of the elements to give high resolution, on the order of 10 lp/mm. The photodetectors, which are built on silicon chips, typically generate a small field of view (on the order of 5 x 5 cm). To obtain a larger field of view, the digital image is magnified to cover the whole breast. Because the quality of such digital images is limited to the quality of the information on the original film, direct digitalization is the better method for diagnostic imaging. With

the CAD algorithms, radiologists are able to perform image processing techniques, such as contrast adjustment.

The need for a better noninvasive, diagnostic imaging technique to overcome the limitations of mammography has generated interest in other imaging modalities such as direct digital mammography, ultrasound, magnetic resonance imaging, nuclear medicine imaging, positron emission tomography and optical mammography. As a supplement to mammography, these novel techniques could offer effective mass screenings of pre-clinical cancers in nonsymptomatic women; reduce the amount of healthcare costs, by reducing the number of unnecessary biopsies; and help to identify optimal treatment for individual patients.

2.3.3 Full Field Digital Mammography

Full-field digital mammography, FFDM, is a new technique currently under development for breast cancer imaging. Several direct digital mammography units are currently in clinical trials awaiting FDA approval [Simonetti, 1998]. In FFDM, fluorescent phosphor screens absorb the X rays transmitted through the breast. The screens convert the x ray photons into visible or infrared light photons that are coupled to CCD detectors by an optical fiber system. This CCD system produces a digitized electrical signal. The quality of this method is limited only by the characteristics of the

detector in the system. For imaging of the whole breast, the detector must be able to accommodate a field size of at least 24 x 30 cm, or 4000 x 5000 pixels, and a resolution of 10 line-pairs per mm or greater. There are several FFDM systems currently under investigation and at least three systems are currently involved in clinical trials for FDA approval.

2.3.4 Other Imaging Modalities

Ultrasound and magnetic resonance imaging are currently used as adjuncts to mammography. Both modalities are used to increase specificity by further characterizing lesions found on mammograms. Ultrasound imaging is routinely used to obtain information about benign lesions such as cysts, while MR imaging is used to interpret multifocal lesions. MR imaging is found to be highly accurate in the diagnosis of invasive cancer.

2.3.4.1 Ultrasound

While ultrasound (US) cannot replace mammography as a screening tool its role as a supplement to mammography is greatly valued. As a mass screening tool, ultrasound tends to be more subjective and has lower resolution than mammography. Also, hard copies of ultrasound images are of a lower quality. However, ultrasound is often used to

evaluate palpable masses of radiographically dense breasts as well as masses detected on mammograms, and it is also used to assess augmented breasts [Gordon, 1995]. For augmented breasts, ultrasound provides a cost-effective way to assess implant rupture. Also, because of the ionizing radiation of mammography, ultrasound is frequently the initial cost effective imaging method for women under 30 years old with a palpable mass and no familial history of breast cancer.

The differentiation of cysts from solid lesions is the greatest strength of ultrasound imaging. Cysts are seen as transparent objects with well demarcated edges on ultrasound images. If a lesion is a cyst, aspiration is used to determine if the fluid in the cyst is clear or bloody. The procedure becomes more complicated if the lesion is a solid. Ultrasound imaging-guided percutaneous biopsy techniques are often used with fine-needle aspiration (FNA) or core sampling to evaluate the solid lesion, (see section 2.4 on FNA and Core biopsy).

2.3.4.2 Magnetic Resonance Mammography

The development of breast coils, enhancing contrast agents and faster imaging sequences have changed the outlook of magnetic resonance imaging of the breast by increasing the sensitivity and specificity of the modality. Although there is no consensus on breast MRI techniques, breast MRI is clinically used in various applications. Such

applications include evaluating patients with implants; evaluation of chemotherapeutic response; and evaluation of multifocality and multicentricity of cancers. The introduction of gadolinium-based contrast agents increases the sensitivity of breast MRI. Breast malignancies enhance (*i.e.* uptake of the contrast agent) faster than normal tissue and thereby appear brighter than normal tissue on MR images [Kaiser, 1993, Flickinger, 1993, Gribbstad, 1994]. Enhanced MR breast imaging through contrast agents is possible because malignancies are highly vascularized. Carcinomas require a new blood supply so that they can proliferate. Most breast lesions larger than 1cm in diameter are vascularized due to the secretion of angiogenic molecules, which promote the growth of new blood vessels. Benign lesions however are comparatively poorly vascularized.

Due to its strong hydrophilia and high molecular weight, a gadolinium-based contrast agent is distributed exclusively in the extracellular space; is rapidly excreted by the kidneys; and tends to accumulate in highly vascularized tissue. Neovascularity, therefore, explains why breast cancer lesions often enhance more rapidly and intensely than benign lesions on MR images after injection of the contrast agent. The rate of enhancement is found to be dependent on the number of blood vessels in pathologic specimens [Kaiser, 1993].

Since some benign lesions, such as fibroadenomas, are also enhanced by the uptake of contrast agents, techniques such as lesion border characterization and

quantitative enhancement kinetics are often applied with breast MR imaging to increase the specificity [Schnall, 1999]. Characterization of lesion borders uses methods similar to those employed in the evaluation of mammograms in which lesions are classified by architectural features (*i.e.*, spiculated borders in malignancies and smooth borders in benign lesions). Enhancement kinetics emphasizes the difference between fast enhancement and washout in malignancies as compared to continuing enhancement in benign lesions.

As of yet, there is no single standardized protocol for MR imaging of the breast. There are a variety of techniques being used that all focus on improving the specificity and sensitivity of MR imaging of breast cancer. The literature agrees that some type of T1 weighted imaging pulse sequence must be performed before and after injection of a contrast medium [Kaiser, 1993, Harms, 1993, Gibbstad, 1994]. Also, contrast enhancement is reported to be more pronounced with the use of 3D techniques rather than 2D imaging techniques. In order to improve the specificity of MR imaging, the modality must be able to consistently resolve lesions detected by conventional mammography. Thus to be able to detect such small lesions and to analyze their architecture, high spatial resolution imaging is required.

Harms *et al* reported that high resolution images with a high signal-to-noise (SNR) ratio were obtainable through 3D techniques such as FLASH (fast low angle shot)

coupled with a fat suppression. Turkat *et al* employed a fat suppressed, spoiled GRASS (gradient-recalled acquisition in the steady state) technique to obtain dynamic MR images. It should be noted that spoiled GRASS and FLASH techniques use the same approach. The spoiled GRASS sequence was performed before and after injection of a contrast agent, such as Gd-DTPA. By measuring the percentage of signal change in lesions on the spoiled GRASS images, the authors were able to obtain a specificity of 83.3% and a sensitivity of 100%. In their study, the interpretation was based only on intensity measurements, without regard to lesion size, appearance on mammograms, or quality of borders.

Fat suppression techniques are utilized because the breast, as outlined in section 2.1, is a very fatty structure, particularly in postmenopausal women. Fat has a very short T1 relaxation time. Thus, on T1 weighted images, fat appears very bright and may therefore mask surrounding objects on the MR images because of the high signal intensity. Fat suppression techniques decrease background intensity and allow small enhancing lesions to be more easily detected. However, most fat suppression techniques do not yield uniform fat suppression over the entire breast and imperfect fat suppression could mask a lesion. One approach to suppress the high intensity signal from fat is the use of subtraction techniques. The unenhanced data set is subtracted on a pixel-by-pixel basis from a contrast-enhanced data set. This negates the high intensity fat. This technique can be utilized with any pulse sequence and can be done after the patient is

removed from the magnet. It must be noted that subtraction techniques are degraded by patient motion. However, motion is generally found to produce recognizable patterns on subtraction MR images [Kaiser, 1993, Greenstein, 1995].

MR imaging has an advantage over mammography in that it utilizes non-ionizing radiation. Also, studies have found it to perform better than conventional mammography with a sensitivity as high as 94%. The specificity is also observed to be better than mammography. MR imaging is able to detect multi-focally breast disease when the mammograms suggest unifocal disease. The true-positive detection rate for multifocal cancer was found to be as high as 88% for MR imaging. A disadvantage of MR imaging is the fact that MR imaging can not detect microcalcifications, which are a major indicator of cancer [Kaiser, 1993, Greenstein, 1995, Harms, 1995, Turket, 1995]. Further, high cost makes MRI prohibitive as a mass screening tool.

2.4 **Prognosis: Biopsies (Surgical, FNA and Core)**

Because mammography cannot easily differentiate between benign and malignant lesions, biopsies are done to assess the nature of indeterminate abnormalities detected on mammograms. The treatment of abnormalities is dependent on how lesions are categorized. Lesions are classified according to the Breast Imaging Reporting and Data System (BI-RADS) as defined by the American College of Radiology (ACR). The

classifications are divided in BI-RADS categories with category number 5 being high risk suspicious lesions that are histologically malignant.

It is estimated that more than 700,000 breast biopsies are performed every year with only one in four of the excised lesions proving to be malignant [Evans, 1995, Ikeda, 1995, Wood, 1995]. For years, the indeterminate masses identified on mammograms have been investigated using surgical biopsy. This procedure calls for image-guided localization with a hook-wire device or visible dyes to identify the position of the lesion and surgical biopsy to liberally remove the tissue around the localizing device. The tissue is then analyzed histologically under a microscope. Both radiography and ultrasound can be used as imaging guiding systems. Surgical biopsies call for close communication between the radiologist, surgeon and pathologist. Likewise, before the procedure, proper mammographic evaluation of the lesion through spot compressions is required to make sure that surgical biopsy is necessary. A major limitation of the procedure is that surgical biopsies can be very disfiguring and can lead to the necessity for reconstructive surgery. Thus, the procedure can be expensive in terms of direct and indirect costs to the patient.

Core sampling and fine-needle aspiration (FNA) are both techniques used to obtain lesion samples without a need for open surgical excision biopsy. Such techniques allow for a reduction in the number of unnecessary surgical operations, the minimization of disfigurement, and a reduction in the biopsy rate of benign to malignant impalpable

lesions [Fentiman, 1999]. Moreover, surgical biopsy is reported to fail for removal of mammographic lesions in 22 % of cases, although surgical biopsy is still recommended for high-risk lesions [Evans, 1995].

Both FNA and core biopsy involve removing lesion cells through an image-guiding procedure to localize the lesion with a needle system. FNA uses thin needles to remove cells for examination. In core biopsy, a thin core of tissue between 1cm and 2 cm in length and 1mm to 3 mm in width is obtained. FNA is a simple and inexpensive method that requires little equipment. However, it requires experienced aspirators and pathologists. Core biopsy requires more equipment but clinicians can readily carry it out because it is a more automated procedure. Also since core samples are larger and intact, pathology laboratories can readily evaluate them. Of the various biopsy procedures, surgical biopsy is the most expensive and invasive. FNA is the least expensive and offers the least information, and core biopsy lies in the middle.

Presently, more automated imaging-guided systems for FNA and core biopsy employ stereotaxic radiography. Such systems can be easily added to existing mammography units or used with dedicated prone tables. While dedicated prone units are better suited to perform biopsies, they are expensive. Stereotaxic localization uses triangulation principles to localize a lesion and to determine the depth (the z coordinate) of the breast lesion. The x and y coordinates are obtained from a single image. The breast

is imaged at two different angles, (+ 15° and –15°) to the left and right of the midline along the *x* axis, and the lesion under investigation is localized. A tiny incision, about 3 mm, is made in the skin and a spring-loaded needle shoots in and out of the tissue in 25/1000 of a second, removing core samples of the lesion [Fentiman, 1999].

2.5 Elastography of Breast Tissue

The relative success of manual palpation in the detection of breast cancer suggests that a method for remote palpation (*i.e.* sensing tissue stiffness or elasticity) could provide a diagnostic tool for detecting cancerous lesions deep within the radiodense breast [Chen, 1995, Fowlkes, 1995, Garra, 1997, Ponnekanti, 1995, Sumi, 1995]. It is of interest to have an imaging modality that can increase lesion specificity. Current work in this area include using mechanical vibrations (*i.e.*, dynamic loading conditions) to evaluate the elasticity of tissue and distinguish and localize lesions.

2.5.1 Ultrasound Elastography

Low frequency mechanical waves are used to evaluate the deformation of soft tissue by vibrating the tissue. Various techniques, such as Doppler, cross-correlation of echoes and speckle tracking have been used to measure axial stains [Cespedes, 1993,

Chen, 1995, Garra, 1997]. Lateral strains are difficult to assess with ultrasound but such out-of-plane strains can be estimated mathematically by applying assumptions about the mechanical properties of the tissues.

2.5.2 MR Elastography

Similar to ultrasound, both static deformation and propagating mechanical waves can be observed with MR. However, unlike ultrasound, MR can provide complete 3D displacement information. Early work used the frequency modulation due to motion in a gradient field as a means to observe propagating waves. Recent MR techniques to measure displacement involve the addition of motion-sensitive gradients. Such gradients cause an additional phase shift in the signal of a voxel and the displacement is related to the phase and the gradient by the equation

$$\phi = \gamma \int_0^{\tau} G_r(t) \cdot r(t) dt \qquad 2.1$$

where τ is the duration of the gradients, $G_r(t)$, after excitation, and $r(t)$ is the position of spins.

For simple harmonic motion (ω-constant), displacement of the spins about their mean position due to the mechanical wave has the form of

$$\xi(r,\theta) = \xi_o \cos(k \cdot r - \omega t + \theta) \qquad 2.2$$

where θ is the initial phase offset. A mechanical actuator driven by a synchronized wave generator supplies the mechanical waves. The waves can also be supplied by the RF pulse generator of the MR system. The gradients are switched in polarity at the same frequency as the motion (position vector) with a duration such that

$$\int_0^{\tau} G_r(t)dt = 0 \qquad 2.3$$

and the observed phase shift in the MR signal is thus

$$\phi(r,\theta) = \frac{2\gamma NT(\vec{G} \cdot \vec{\xi}_o)}{\pi} \sin(\vec{k} \cdot \vec{r} + \theta) \qquad 2.4$$

where T is the period of the mechanical excitation that is equal to $2\pi/\omega$, and N is number of gradient cycles.

Strain distribution created by the propagating wave can be computed from the phase of the MR signal. Components of the displacement vector in any direction can be estimated, and the propagating speed of the wave depends on the elasticity of the material. Measurement of the local wavelength, λ, of the wave provides information about the spatial distribution of the elastic modulus (*e.g.*, velocity = $\lambda \nu$, where ν is frequency and $\nu = \omega / 2\pi$). The wavelength, λ, varies according to stiffness of the material and input frequency. Processing of the wave image can generate a quantitative local frequency estimate map, called an elastogram. Such techniques have been used to estimate the elastic modulus of *in vivo* brain tissue [Kruse, 1999]. A problem with using a vibration wave approach to evaluating mechanical properties of soft tissues in MR is that reflections and scattering on tissue interfaces and boundaries may lead to deviations.

2.6 **Definitive Treatment Of Malignant Lesions**

Once a lesion as been biopsied and is diagnosed as malignant, it must be treated surgically. The surgical procedures for malignant lesions are: lumpectomy, with re-excision of margins or with axillary dissection; and mastectomy, with or without reconstruction. Lumpectomy is a breast conserving treatment in which a wide excision is performed to remove the lesion and some surrounding normal tissue. The surrounding tissue is examined to determine if it is free of tumor cells. If the surrounding tissue margins are not free of disease, more extensive surgery may be necessary. Often this

procedure also involves the dissection of axillary lymph nodes to ensure no cancer cells have spread to the region [Porrath ,1986, Evans, 1995, Dixon, 1998].

Total mastectomy involves the removal of the entire breast tissue with overlying skin (including the areola and nipple). A subcutaneous mastectomy is one in which the skin and areola are left intact. A radical mastectomy is one in which the pectoralis muscles and all axillary regions are removed. The most common breast cancer procedure is the total mastectomy with some limited axially dissection [Dixon, 1998].

In current practice, the planning of surgical procedures for excising malignancies involves evaluation of 2D mammograms by both the surgeon and radiologist. This process requires considerable experience and is usually accurate for well-defined abnormalities, *i.e.*, lesions that are clearly classified and focal. Problems such as multifocality are not effectively detected by present 2D imaging modalities [Guo, *et al* 1995]. Even with the 3D capabilities of MR imaging, the breast shape is deformed during imaging, since MR images are acquired with the patient in the prone position, with the breast cupped in a breast coil.

When the patient is placed supine for surgical procedures, the 3D MR images cannot adequately aid the surgeon in precise localization of the lesion. Surgeons have reported that they are unable to accurately localize a lesion in dense breasts once the patient is in a supine position [Guo, 1995]. The problem of 2D images is found in most

surgical procedures. Several investigations have been carried out to introduce the technique of 3D imaging based on computerized tomographic (CT) data into the pre-operative evaluation and planning [Guo, 1995]. Morphing of digital images such as 3-D MR prone images into 3D supine images may greatly optimize breast conservation surgeries by increasing the accuracy of surgical excision of localized lesions. This may minimize disfigurement, reduce the need for repeat operations, and increase the effectiveness of reconstructive procedures.

An understanding of the mechanical properties of breast tissue may be used to develop more accurate breast models. Such biomechanically based models can be used to develop computer algorithms which accurately mimic deformation of breast tissue undergoing external forces typically incurred in diagnosis. Such models may also better aid in surgical biopsies and breast conservation procedures, and may improve the prognosis for breast cancer patients.

CHAPTER 3

BIOMECHANICS OF SOFT TISSUE

The study of biomechanics has proven very useful to the field of orthopedics in understanding the mechanical forces of ligaments, tendons, and fractures. With such knowledge, prosthetic biomaterials have been designed and are widely used in bone injuries (*e.g.,* hip replacement, bone plates and screws). Biomechanics has also contributed to the understanding of accidental injuries and the development of equipment to protect biological systems from traumatic injuries. In addition, biomechanics is significant in the preoperative evaluation and planning of brain and spine surgeries [Park, 1992].

Knowledge of the mechanical behavior of *in vivo* breast tissue may contribute to the detection, biopsy and treatment of breast cancer. Since malignant masses tend to be harder than benign masses, an understanding of the normal and pathological biomechanical nature of breast tissue may provide more accurate discrimination of breast

masses [Chen *et al* 1995, Fowlkes *et al* 1995, Garra *et al* 1997]. As stated in section 2.5, elastography techniques use mechanical properties to localize lesions and increase specificity. For diagnosis and detection, breast biomechanics may aid in CAD (Computer Aided Diagnosis) procedures and serial screening to track changes in mammograms. Since compression forces as well as positioning may vary between the annual screening mammograms of a patient, accurate transformation algorithms based on physical principles may be used to better register and align the subsequent images. Accurate breast models developed from the mechanical behavior may better aid in surgical biopsies, pre-operative planning and breast conservation procedures, and thereby improve the prognosis for breast cancer patients.

3.1 **Theory and Definitions**

When loads or forces are applied to a material, the material tends to respond by deforming. The type of response depends on the type of load, duration of the applied load, rate of loading, and the mechanical properties of the material. Types of loading include tensile, compressive, shear, and bending forces. The mechanical and structural properties of a material are described by such parameters as elasticity, isotropy, viscosity, and plasticity. The mechanical behavior of a material is described in terms of its stress-strain or constitutive relationship. Constitutive equations describe the physical properties of materials [Fung, 1977, Fung 1993].

For a material undergoing a mechanical deformation, stress, σ, equals force per unit area of contact over which the force acts, and it is related to the strength of the material. Stress is usually expressed in Newtons per square meter (also known as Pascal or Pa) or pounds per square inch (psi). Compressive stresses are generated in response to loads that squeeze an object together, while tensile stresses are due to loads that pull an object apart. Shear stresses are due to loads that deform an object by sliding layers past each other (or in a twisting fashion).

Strain, ε, is a measurement of the corresponding deformation or displacement of the material caused by the stress. It is expressed as the ratio of the change in size of the material. Being a ratio, strain has no dimensions, but it is sometimes expressed as a percentage. Conventionally, the linear stress and strain are defined as

$$\sigma = F / A_o \quad \text{Stress}$$

$$\varepsilon = \Delta L / L_o \quad \text{Strain} \qquad \textbf{3.1}$$

where A_o is the original cross-sectional area, L_o is the original length; F is the applied force, and ΔL is the deformed length minus the original length.

For example, if a cubic volume is subjected to a compressive force normal to the top and bottom of the cubic faces in the z direction, the incremental force created on the top and bottom of the faces is

$$dF_z = \sigma_z dA_o \tag{3.2}$$

where A_o is the surface area of the cubic face, F_z is the applied force, and σ_z is the normal or axial stress. If the force is applied gradually, as in static loading, the volume element undergoes a displacement in the z direction of

$$d\Delta Z = \varepsilon_z dZ \tag{3.3}$$

where $\Delta Z = Z_o - Z$ and ε_z is the axial strain, Z_o is the original length, and Z is the deformed length.

Stress and stress as thus defined are the typical engineering definitions. For linearly elastic materials under small strains these definitions hold. However for large elastic deformation, in order for the volume of the material to remain a constant, the area must change. Therefore, the applied force acts over a different area and the stress varies. Such a stress is defined as the *true* or Cauchy stress and is expressed as

σ = Force/ Instantaneous Area 3.4

Similarly with the strain, the *true* strain is defined as

$\varepsilon = ln\,(L/L_o)$ 3.5

where L is the deformed length and L_o is the undeformed length. Because of the logarithm, this strain is sometimes referred to as the natural strain.

To specify the 3D state of a material in x, y, z rectangular coordinates, nine components of the stress and strain are necessary. These nine components form a symmetric matrix known as a tensor of rank two. The shear and normal stresses are represented as

$\sigma_{xy}\ \sigma_{xz}\ \sigma_{yx}\ \sigma_{yz}\ \sigma_{z\,x}\ \sigma_{zy}$ and $\sigma_{xx}\ \sigma_{yy}\ \sigma_{zz}$. 3.6

respectively. The strain tensor, ε_{ij} represents the 3D state of strain in a material and can be calculated from the components of the displacement vector. The displacement vector, $\boldsymbol{D}$, is defined as the displacement of a point $P\,(x, y, z)$ in the undeformed volume to the point, $P'(x', y', z')$ in the deformed volume. This vector is expressed as

$$\mathbf{D} = u\hat{\mathbf{x}} + v\hat{\mathbf{y}} + w\hat{\mathbf{z}} \qquad \textbf{3.7}$$

where the vector components are $u = x' - x$, $v = y' - y$, and $w = z' - z$. For linear elastic materials, the Cauchy strain tensor is expressed as

$$\varepsilon_{ij} = \frac{1}{2}\left(\frac{\partial D_i}{\partial j} + \frac{\partial D_j}{\partial i}\right) = \varepsilon_{ji} \qquad \textbf{3.8}$$

and the linear stress-strain relationship is expressed as

$$\sigma_{ij} = C_{ijkl}\,\varepsilon_{kl} \qquad \textbf{3.9}$$

where σ_{ij} and ε_{kl} are the stress and strain tensors, respectively, and C_{ijkl} and is a tensor of the elastic modulii [Fung,1993]. If the stress and strain relation of a material is the same in all directions, then the material is isotropic. Materials such as steel and glassy polymers are isotropic, but biological and composite materials are not. Such materials are characterized as anisotropic. Anisotropic materials can have up to 36 elastic modulus tensor components, (*i.e.*, if C_{ijkl} is symmetric then it has 36 independent elastic constants). For isotropic materials, the number of independent elastic constants can be reduced to two.

If the stress-strain behavior is plotted on a graph, the resulting curve is the mechanical response of a material to an applied load. The linear section of the curve is defined as the elastic region. In such a region, the strain increases linearly with stress and after the load is removed the material returns to its original shape. The slope of the curve in this region is called the Young's modulus or modulus of elasticity, E (*i.e.*, C_{ijkl} in equation 3.9). The Young's modulus of a linear elastic material is the ratio of the stress and strain. If the modulus is large, then the material is very stiff (*e.g.*, E of steel is 3×10^6 psi). Another material property is the shear modulus, G, which is the ratio of shear stress to shear strain. For linear, elastic materials, Young' modulus is related to the shear modulus by the expression

$$E = 2G(1+\nu) \qquad \textbf{3.10}$$

where ν is the Poisson's ratio. Poisson's ratio is defined as the negative ratio of the transverse strain to the longitudinal strain. Poisson's ratio is typically about 0.33 for stiff materials and 0.5 for rubbery materials and biological soft tissue [Park, 1992].

Equations 3.1 to 3.10 represent conditions of linear, small strain elasticity involving infinitesimal deformations. Finite strain analysis which involves large deformations and nonlinear elasticity is more complicated. The mechanical nature of biological tissue is too complex to use simple linear modeling and mathematical

modeling with tensors is encumbered when using *in vivo* experimental data collected from human subjects. *In vivo* measurements are inherently limited in the number of experimentally obtainable data points because human subjects cannot be manipulated in the same manner as *ex vivo* tissue. Thus, it is virtually impossible to evaluate completely the elastic modulii tensor, which can have up to 36 constants for some anisotropic materials.

3.2. **Material Properties**

Poisson's ratio relates the volume changes of a material to compressive forces. For materials with a Poisson's ratio of 0.3 to 0.4, the materials are defined as compressible, that is their volume increases when the materials are stretched, and decreases as the materials are contracted (*i.e.*, compressed). Incompressible materials have a Poisson's ratio of 0.5 and such materials experience no volumetric strain on extension.

Other material properties are plasticity, viscoelasticity, and isotropy. If a material exhibits a plastic behavior then after an external load is applied and removed, the material does not return back to its original shape but remains permanently deformed. Plastic deformation is independent of time. At small deformations, the response of materials

such as steel and aluminum is almost purely elastic. However, such materials can behave plastically at large deformations [Park, 1992].

Viscoelastic behavior of a material is time dependent such that the stiffness of a viscoelastic material depends on the rate of application of the load. For such materials, the stress-strain relationship depends on time, and in such materials, the mechanical energy is dissipated by conversion to heat. Viscoelastic materials have both an elastic and a viscous component to their behavior. Thus all materials can display some viscoelastic behavior. However, synthetic polymers, wood and soft tissues possess a significant viscoelastic nature. The significance of a viscoelastic response is evaluated from the creep and stress relaxation components. For viscoelastic materials, creep is defined as the slow, progressive deformation of the material under constant stress. Stress relaxation is the gradual decrease of the stress as the material is held at constant tension, or extension.

3.3 **Strain Energy Functions and the Constitutive Relationship**

For a cubic volume subjected to a compressive load (*i.e.*, force) normal to the top and bottom of the volume in the z-direction (see the example in section 3.1), the force multiplied by the distance the volume travels in the same direction is equal to the work done by the force. Therefore the work is defined as

$$dU = \tfrac{1}{2}\, dF_z\, d\Delta Z \qquad 3.11$$

$$= \tfrac{1}{2}\,(\sigma_z\, dX\, dY)\varepsilon_z\, dZ$$

$$= \tfrac{1}{2}\ \sigma_z \varepsilon_z\, dV$$

where $dV = dX\, dY\, dZ$ and dF_z is defined in equation 3.2. Provided that no energy is lost due to heat or consumed by chemical reactions, the external work done by loading is stored in the system and converted into internal energy, called strain energy. As defined in equation 3.11, this strain energy is simply the product of stress and strain for linearly elastic materials.

Because of material complexity, a frequent approach to modeling the mechanical behavior of soft tissue is by using the strain energy density function (SEDF) to describe the constitutive relationship. Fung first introduced such mathematical modeling of the stress-strain relationship to soft tissue mechanics in 1967 [see Fung, 1993], however since the 1940s, continuum mechanics and its theories have been used to develop such SEDF relationships that fit the behavior of rubber materials. The strain energy is a function of the strain components through quantities called the principal strain invariants. Different forms of the SEDF differ in how the strain invariants are calculated. The SEDF is expressed as $U = U(I_1, I_2, I_3)$ where I_1, I_2, I_3 are the strain invariants in the direction of the principal axes 1, 2, and 3. Principal axes are a special set of axes, which

at a given point in an object the shear strain components vanish. The normal strain components on the principal planes are known as the principal strains.

Strain invariants are scalar parameters that define the state of strain in a material, and they are more convenient to use than the strain tensor in modeling the constitutive relationship of *in vivo* soft tissue. Strain invariants maintain their form and values under all transformations of coordinates. The strain invariants are functions of the principal stretch (extension) ratios, λ_1, λ_2, and λ_3. The stretch ratios are characterized as the lengths of the sides of an undeformed unit volume oriented in the direction of the principal strains and are introduced to define the distortion for large (finite) deformation analysis. Recall that the principal axes are those at which the shear strain components *(i.e.,* $i \neq j$*)* vanish, and when this occurs the strain invariants are

$$I_1 = \sigma_{xx} + \sigma_{yy} + \sigma_{zz}$$

$$I_2 = \begin{vmatrix} \sigma_{yy} & \sigma_{yz} \\ \sigma_{zy} & \sigma_{zz} \end{vmatrix} + \begin{vmatrix} \sigma_{zz} & \sigma_{zx} \\ \sigma_{xz} & \sigma_{xx} \end{vmatrix} + \begin{vmatrix} \sigma_{xx} & \sigma_{xy} \\ \sigma_{yx} & \sigma_{yy} \end{vmatrix} \qquad \textbf{3.11}$$

and

$$I_3 = \begin{vmatrix} \sigma_{xx} & \sigma_{xy} & \sigma_{xz} \\ \sigma_{yx} & \sigma_{yy} & \sigma_{yz} \\ \sigma_{zx} & \sigma_{zy} & \sigma_{zz} \end{vmatrix}$$

For infinitesimal deformation of linearly elastic media, the strain invariants can be defined as

$$I_1 = \lambda^2_1 + \lambda^2_2 + \lambda^2_3 \qquad 3.12$$

$$I_2 = \lambda^2_1\lambda^2_2 + \lambda^2_2\lambda^2_3 + \lambda^2_3\lambda^2_1$$

$$I_3 = \lambda^2_1\,\lambda^2_2\,\lambda^2_3$$

The first stretch ratio is in the direction of the applied force and is defined as

$$\lambda_1 = \text{deformed length/ undeformed length} \qquad \textbf{3.13}$$

and the second and third ratios are usually estimated from the first stretch ratio, for example [Nahum, 1993]

$$\lambda_2 = \frac{1}{\sqrt{\lambda_1}} \quad \text{and} \quad \lambda_3 = \frac{1}{\sqrt{\lambda_1}} \qquad \textbf{3.13}$$

where λ_2,and λ_3 are orthogonal and in directions perpendicular to the applied force. The relationship expressed in equation 3.13, is determined by using the conservation of volume, (*i.e.*, volume of the undeformed object = volume of the deformed object). For incompressible materials, which have constant volume under deformation

$$\lambda_1 \lambda_2 \lambda_3 = 1 \qquad 3.15$$

and equations 3.12 reduce to

$$I_1 = \lambda^2_1 + \lambda^2_2 + 1/\lambda^2_1 \lambda^2_2 \qquad 3.16$$

$$I_2 = 1/\lambda^2_1 + 1/\lambda^2_2 + \lambda^2_1 \lambda^2_2$$

$$I_3 = 1$$

The expressions given in equation 3.16 are often used for finite deformation of an incompressible material.

The relationship between the stress and the strain invariants is generally evaluated by taking the partial derivative of the SEDF with respect to the stretch ratio in the desired direction [Nahum, 1993, Silver, 1987].

$$\sigma_i = \frac{\partial U}{\partial \lambda_i} \qquad 3.17$$

Several forms of the SEDF, based on logarithms or power series, have been proposed for modeling the behavior of soft tissue [Farshad *et al*, 1998, Fung, 1993, Silver, 1987]. Most abundant in the literature are the Mooney-Rivlin and Ogden models,

which model nonlinear, elastic and incompressible materials [Farshad *et al*, 1998]. Many commercial computer simulation programs are written to accept these models. The polynomial SEDF is expressed as

$$U = \sum_{i+j=1}^{N} C_{ij}(I_1 - 3)^i (I_2 - 3)^j \qquad \textbf{3.18}$$

where N is defined as the complexity of the polynomial, and the coefficients, C_{ij}, are the material parameters. The Mooney-Rivlin model is a simple form of the polynomial SEDF with N=2 and is expressed as

$$U_{\text{Mooney-Rivlin}} = C_{10}(I_1 - 3) + C_{01}(I_2 - 3) \qquad \textbf{3.19}$$

where the coefficients, C_{ij}, are the material parameters (and not the modulii as in equation 3.9). For the Mooney-Rivlin model, the strain invariants are expressed as

$$I_1 = \lambda_1^2 + 2/\lambda_1$$
$$I_2 = 2\lambda_1 + 1/\lambda_1^2. \qquad \textbf{3.20}$$

For the Mooney-Rivlin model, the stress along the direction of the applied force (*i.e.*, the 1st principal axis) can be expressed as

$$\sigma_{1,\text{ Mooney-Rivlin}} = 2C_{10}\left(\lambda_1 - \frac{1}{\lambda_1^{\,2}}\right) + 2C_{01}\left(1 - \frac{1}{\lambda_1^{\,3}}\right) \qquad \textbf{3.21}$$

The Ogden model is expressed as [Twizell and Ogden, 1983]

$$U_{\text{Ogden}} = \sum_{i=1}^{N} \frac{2A_i}{B_i^2}\left(\lambda_1^{B_i} + \lambda_2^{B_i} + \lambda_3^{B_i} - 3\right) \qquad \textbf{3.22}$$

where A and B are coefficients and the constitutive relationship is expressed as the following for N=1

$$\sigma_{1,\text{Ogden}} = \frac{2A}{B}\left(\lambda_1^{B-1} - \lambda_1^{-\frac{(B+2)}{2}}\right) \qquad \textbf{3.23}$$

where $\lambda_2 = \lambda_3$ (using equation 3.13) for uniaxial compression [Fung, 1972]. Without using equation 3.13, the stress is expressed as

$$\sigma_{1,\text{Ogden}} = \frac{2A}{B}\left(\lambda_1^{B-1}\right) \qquad \textbf{3.24}$$

The Blatz Model, an exponential SEDF that represents volume compressible materials, has the form [Fung, 1993]

$$U_{Blatz} = \gamma\left[e^{\alpha(\lambda^2-1)} - 1\right] \qquad \textbf{3.25}$$

where γ and α are the coefficients. For uniaxial experimental testing, the constitutive relationship is modeled as

$$\sigma_{1,Blatz} = \frac{\gamma}{\alpha+1}\left[\lambda_1 \exp\left[\alpha\left(\lambda_1^2 - 1\right)\right] - \frac{1}{\lambda_1^2}\exp\left[\alpha\left(\frac{1}{\lambda_1} - 1\right)\right]\right] \qquad \textbf{3.26}$$

An exponential form of the SEDF postulated by Vito for connective tissue [Vito, 1973] is

$$U_{Vito} = A\left[e^{B(I_1-3)+C(I_2-3)} - 1\right] \qquad \textbf{3.27}$$

where A, B and C are coefficients and the strain invariants are defined as

$$I_1 = \lambda_1^2 + 2/\lambda_1 \qquad \textbf{3.28}$$

$$I_2 = 2\lambda_1 + 1/\lambda_1^2.$$

$$I_3 = 1$$

and the constitutive equation is expressed as

$$\sigma_{1,\text{Vito}} = 2A\left(\lambda_1 - \frac{1}{\lambda_1^2}\right)\left(B + \frac{C}{\lambda_1}\right)\exp[B(I_1 - 3) + C(I_2 - 3)] \qquad \textbf{3.29}$$

As stated before, there are many SEDF models in the literature but initially such models were not formulated to correlate with the experimental procedures that measure the data, (*i.e.,* the stretch ratios). That is, the experimental data did not provide good fits to the postulated models. For the best data fit to the models, it is necessary to design experiments that can accommodate all of the states of strain. The Blatz model uses this approach, but the Mooney-Rivlin model does not. For the Blatz model, for example, data fit improves when using both uniaxial tensile and biaxial tests [Fung, 1972].

The testing methods that can cover the strain states along the principal axes are: 1) simple elongation, 2) pure shear, and 3) two dimensional extension (or uniaxial compression). For pure shear, $\lambda_1 = 1$, and for simple elongation, $\lambda_2 = \lambda_3$ [Fung,1993]. The stress-strain relationship for incompressible elastic materials, such as rubber, undergoing various compressive loading is a well-known problem and was first investigated by Boussinesq in 1885 [Ponnekanti, 1994]. Exact, simple solutions for the stress distribution under circular and rectangular compressors have been described since 1970 [Ponnekanti, 1994].

For biological soft tissues, it is difficult to design experiments to examine all of the states of strain because of the high complexity of the material and the environment. *Ex vivo* specimens must be handled carefully and clamping of the biological specimens is reported to be a problem [Silver, 1987]. Also, such specimens may behave differently in a synthetic lab environment. *In vivo* experimentation is complicated by the fact the tissue is not as easy to manipulate without discomfort or injury to the study subject.

3.4 **Biological Tissue Models**

Most biological tissue is generally modeled as a nonlinear, anisotropic, viscoelastic, volume incompressible continuum with a nonlinear stress-strain relationship [Fung, 1993]. Application of external forces, such as loads or gravity, to such materials causes large deformations and a change of internal (potential) energy. The particular shape of deformation is a function of both the internal strains and stresses within the tissue, and the external forces applied to soft tissue [Fung, 1993]. The elastic deformation of soft tissue has been directly associated with the change in potential energy [Fung 1993, Gallagher *et al.*, 1982, Park *et al.*, 1992, Sumi *et al.*, 1995]. Breast tissue is a composite of mechanically different materials (*e.g.*, adipose and glandular tissues) and may be modeled as a mixture of a porous matrix in an incompressible fluid using a biphasic strain energy model. Such models have been used to represent biological soft hydrated tissues

[Almeida, 1997]. The biphasic model represents the tissue as a continuum mixture composed of a solid matrix immersed in interstitial fluid.

Under some conditions of applying external loads, a pseudolinear, isotropic model of breast tissue may suffice. Under other loading conditions, a linear, isotropic and piece-wise homogenous model may also be sufficient to describe the mechanical behavior of soft tissue. [Humphey, 1993]. In such a model, breast tissue is limited to consist of two dominant non-interacting systems, one of fatty tissue and the other glandular tissue, and a gel-like isotropic matrix. In this model, the various systems of densely distributed extensible fibers are embedded in the homogenous gel matrix and both the matrix and the fibers follow gross elastic deformation [Humphey, 1993].

Under quasistatic loading conditions, soft tissues are capable of large elastic deformations, and can be characterized as hyperelastic materials, with a bulk modulus that is several orders of magnitude larger than the shear modulus [Fung, 1993, Humphey,1993]. Such materials also tend to deform in an incompressible manner. With this model, breast tissue can be modeled as a hyperelastic, isotropic, incompressible material.

3.5 Material Properties of Components of the Breast

As stated in section 2.1, the breast is a composite volume filled with adipose, glandular and various fibrous tissues. Both adipose and glandular tissues obtain their mechanical properties from collagen and elastin fibers. Elastin fibers provide elasticity to the tissue and collagen fibers provide strength [Nahum *et al* 1993]. Some variables that affect the mechanical behavior of fibrous tissues such as adipose and glandular tissue, involve 1) collagen fiber content, 2) elastin fiber content, 3) orientation of collagen fibers, and 4) distribution and type of collagen content [Silver, 1987].

At low strains, the mechanical properties of biological connective tissues can be due to either 1) the alignment of the collagen fibers, 2) expression of synovial fluids (such as in joints), or 3) deformation of elastic fibers or other components [Silver, 1977]. For example, at low strains the mechanical nature of the aorta is dominated by the deformation of elastic fibers, but in skin the mechanical behavior is largely due to the alignment of the collagen fibers [Silver, 1987]. Generally at high strains (large stretch ratios) the mechanical behavior of most connective tissues is dominated by the properties of the collagen network. At high strains, the collagen fibers are aligned and all connective tissues behave similar to tendon, however the strain at which the collagen fibers are completely aligned varies from tissue to tissue. Therefore the behavior of connective tissue is divided into three types that include: 1) oriented (aligned) collagen networks,

such as in tendon and pericardium, 2) orientable or alignable collagen fiber networks, such as in the aorta and skin, and 3) composite layers of types one and two, such as in articular cartilage [Silver, 1987].

3.6 **Finite Element Modeling**

Finite element modeling (FEM) was introduced some 30 years ago as a method for solving problems in structural mechanics. As FEM has become employed to more and more applications, it is now widely used in numerical approximations for any physical system that can be modeled by differential equations. With FEM analysis software that is currently in use, it is relatively easy to incorporate the complex material properties of biological tissue under various loading conditions. However, *in vivo* mechanical analysis of biological tissue can depend on more complicated parameters than just stress and strain, but on such complex parameters as strain rate (*i.e.*, viscoelasticity) and temperature.

Finite element models are capable of simulating a wide variety of materials, loading, and boundary conditions. With FEM, real-situation loading can be applied to the model, and the model can also be designed using experimental deformation data. FEM describes a volume or surface as a set of basic elements. The volume of an object is divided into subregions of finite elements, and each element possesses the material

properties of the object, (*e.g.*, steel, rubber, soft tissue). Associated with each element are nodes at which adjacent elements are linked together. Typical finite elements are shown in Figure 3.1. Finite element analysis involves estimating a continuous function by approximating the values at finite number of points within the domain. The accuracy of the solution increases with number of points (*i.e.*, nodes) used.

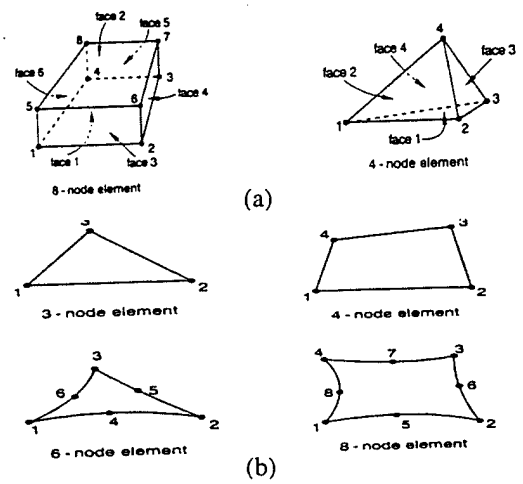

Figure 3.1 FEM elements used to model materials. (a) Solid or volume elements. (b) Shell or membrane elements.

Abaqus [Hibbitt, Karlsson & Sorenson, Inc. Pawtucket, RI.] is a widely employed FEM simulation software package that is specially designed for advanced analysis applications. It has a variety of modeling tools and it has the capability to simulate a wide variety of material properties such as: elasticity, electrical conductivity, permeability, anisotropy and diffusivity. Abaqus is used for heat transfer, stress displacement and other

types of analysis in mechanical, biomedical, and civil engineering applications. User-defined materials can be created with a subroutine interface. Abaqus can provide both time and frequency analysis in which the response can be linear or nonlinear. Such analyses include static stress and displacement as well as viscoelastic and viscoplastic responses.

Abaqus is also capable of providing nonlinear, transient, dynamic analysis of solids and structures (such as transient dynamic stress/displacement analysis and transient or steady state heat transfer analysis) using explicit time integration. It is highly effective for quasistatic applications involving discontinuous nonlinear behavior. Abaqus can also be used in analysis of coupled problems such as thermo-electrical, acoustic-mechanical, and piezoelectric systems. For example, acoustic interface elements are available to couple structural and acoustic medium models for dynamic and vibration analysis.

Standard Abaqus elements include shell, membrane, and solids, (see figure 3.1). A continuum can be modeled using the 1D, 2D and 3D continuum elements provided with reduced integration and hourglass control. A combination of elements, each with any appropriate material properties, can be used in the same analysis. Abaqus also is capable of modeling interactions between objects, such as surface-to-surface contact, with or without friction.

CHAPTER 4

INITIAL DEFORMATION STUDIES USING MRI

In order to analyze breast deformation and *in vivo* tissue displacement, it was necessary to visually observe the displacement of regions of interest. Preliminary studies were conducted on both tissue-like phantoms and a group (N=7) of healthy female subjects. Magnetic resonance imaging (MRI) was used to identify promising internal landmarks (*i.e.*, tissue) and to map their displacement. MRI was also used to characterize the imaging properties of various external landmarks, which were used to obtain localization coordinates.

In order to evaluate deformation, the human breast and various breast phantoms were deformed from their original shapes by applying external loads such as compressive and gravitational forces. While the compressive forces were applied gradually with a specially designed mechanical apparatus, gravitational forces were applied by simply moving the model or subject from a prone position to a supine position.

4.1 Breast Tissue Models: Phantoms and Human Test Subjects

4.1.1 Phantoms

Types of tissue phantoms employed in the studies were: saline breast implants, in-house gels and various breast molds. The saline implants are round, 15 cm, silicone gel-filled mammary prostheses, which are routinely used for tissue replacement following mastectomies or for breast augmentation. The prostheses possess two chambers, an inner silicone-filled envelope, and an outer envelope that is filled with normal saline. The outer envelope has low modular properties and the elasticity (*i.e.,* the stiffness of the prosthesis) can be varied by changing the volume of saline solution in this chamber. The phantoms have high signal intensity and appear very bright on MR images.

A second type of breast prosthesis used was a mold of silicone in the shape of a human breast. Such molds are routinely used for external breast augmentation. The phantom has a high signal intensity and for MRI experiments, the prosthesis was affixed to a plaster cast of a chest wall to simulate the curvature of the chest.

A biopsy training phantom was used also. Such devices are routinely used to train radiologists in fine needle aspiration (FNA) and core biopsy imaging. The model is in the shape of the breast and has a range of inclusions, which simulate lesions such as tumors

and cysts. The dark objects in the phantom represent tumor masses and the green masses represent cysts. On MR images, the dark masses appear as regions of signal voids and the green masses appear as regions of increased signal. The sizes of the signal voids are comparable to the sizes of the masses. The prosthesis is somewhat deformable, however not as deformable as healthy breast tissue. When the device is compressed, the locations of the masses move and so the device is useful for mapping displacement of the inclusions.

4.1.2 Human Subjects

To investigate deformation of normal breast tissue, a group of healthy female subjects of various ages were studied. The subjects were all premenopausal women over the age of 18. Written informed consent was obtained according to a currently active MRI protocol approved by the Ohio State University Biomedical Sciences Human Subjects Review Committee. Pregnant women and subjects with mental disabilities were excluded from the studies.

4.2 **Development of Experimental Protocol**

The role of MRI in breast cancer imaging is briefly outlined in section 2.2.1.1. As of yet, there is no single standardized protocol for MR imaging of the breast but the

literature indicates that a *T1* weighted, high resolution, fast imaging pulse sequence is necessary in order to obtain diagnostically useful MR images. All of our MR imaging was performed without using contrast agents. Therefore, the need for a fast sequence arose not from the need to monitor kinetics of a contrast agent but from the need to limit patient motion and discomfort.

4.2.1 Magnetic Resonance Imaging of Breast tissue

MR images of breast models were acquired on a 1.5 T clinical MRI system (Signa, General Electric, Milwaukee, WI) using various RF coils that included a commercial phased array breast coil, body coil, and a flat surface coil. We began our study by investigating 2D spin echo and gradient echo techniques because of their speed. A partial listing of various MRI pulse sequences investigated is given in table 4.1, (see appendix for a complete listing of all MR imaging). As shown in the table, MRI techniques included such pulse sequences as: 1) a *T1* weighted spin echo (*TR/TE* 700/10ms) with 0.4 x 0.4mm in-plane resolution and 5mm slice thickness, 2) a *T2*-weighted fat suppressed fast spin echo sequence (*TR/TE* 7000/100ms, echo-train length of 16) with 0.8x0.8mm in-plane resolution, and 3) a 2D gradient echo sequence (*TR*=11.2ms and 25ms).

TABLE 4.1. Partial List of MR Imaging Techniques					
Sequence #	1	2	3	4	5
Plane	Sagittal	Sagittal	Sagittal	Sagittal	Coronal
Pulse Sequence	2D spin echo	2D fast spin echo	2D gradient echo	3D fast gradient echo	3D fast spoiled gradient echo
TR	700 ms	7000 ms	11.2/25ms	14 ms	25 ms
TE	10 ms	100 ms	2.9/4.2 ms	2.8 ms	4.2 ms
Flip angle/ETL	n/a	16	25	20	25
Resolution	0.4x0.4 mm	0.8x0.8 mm	0.8x1.04mm	0.6x.0.6 mm	0.4x0.4 mm
Slice thickness	5 mm	5 mm	5 mm	2 mm	1.4 mm
Signal avg.	1	2	4	1	1
Scan time	3:09	5:36	2:37	:30	6:50

TABLE 4.1. Partial List of MR Imaging Sequences Used to Image the Breast.

Sequences # 1 , 2 and 3 were employed with a commercial breast coil to develop an optimal protocol to image the breast. As we studied these 2D pulse sequences, we varied the *TE* parameter, (as shown in sequence #3) to observe how the resolution changed in the vicinity of the fatty regions in the breast. These initial images were acquired with *TE's* of 2.9ms and 4.2ms. For a *TE* of 2.9ms, fat and water magnetization are out-of-phase (180 °) and thus all image volume elements that contain fat and water

give a reduced signal, leading to dark outlines between the boundaries of fatty and glandular tissue. For *TE* of 4.2 ms, fat and water magnetization are in-phase and the signal from fat and water components add up and the boundary voxels have intermediate signal. The purpose of varying *TE* was to evaluate if the dark tissue boundary outlines could provide useful landmarks. However, with the low slice resolution (*i.e.*, 2D sequences and 5 mm slice thickness), this was not useful because relatively broad dark bands were observed due to signal combination across the thick slices. Further tests with higher resolution and thinner slices (1.4 mm) proved this boundary approach was not very useful in detecting internal landmarks.

The fast 2D sequences were quickly abandoned because of the low slice resolution they produced. We moved on to 3D techniques such as gradient echo and spoiled gradient echo, and began varying such imaging parameters as slice thickness, flip angle, and *TR* times in order to optimize the imaging and accommodate the tradeoff between high resolution and acquisition time.

4.2.1.1 Optimal Imaging Protocol

After imaging with high resolution sequences such as 3D fast gradient echo (GRE) and 3D fast spoiled gradient (FSPGR) techniques, we found that the 3D fast SPGR sequence produced better images. Spoiled gradient echo techniques are faster than

standard gradient techniques because spoiled techniques produce an equilibrium of the longitudinal magnetization without coherent transverse magnetization at the end of *TR*. SPGR images have good SNR and anatomic detail and are primarily *T1* weighted with scan times of several seconds for a single slice and of 4-15 minutes for volumes [Westbrook, 1993]. For the SPGR sequence, the signal is expressed as

$$S = \frac{\sin\theta\left(1-\exp\left(-TR/T_1\right)\right)}{1-\exp\left(-TR/T_1\right)\cos\theta} \qquad \textbf{4.1}$$

where *TR* is the repetition time and θ is the flip angle. Optimal adipose and glandular tissue contrast were obtained by varying *TR* and θ. Figure 4.1 shows the signal contrast curve with *T1*=800 ms for glandular tissue and *T1*= 300 ms for adipose tissue.

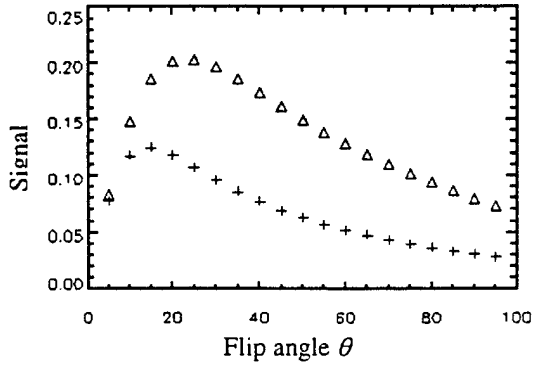

Figure 4.1 SPGR signal for glandular (+ - T1=800 ms) and adipose tissue (Δ - T1=300 ms) at *TR* = 25 ms.

The maximum signal contrast occurs for flip angles of 25° to 30°. However for such flip angles, the MR acquisition time can be as long as 13 minutes. For a more suitable acquisition time, larger flip angles are required. From the figure above, at a flip angle $\theta = 60^{\circ}$, the signal contrast is expressed as

$$S_{fat} / S_{tissue} = 2.48 \qquad \textbf{4.2}$$

For these imaging parameters, the resolution and the contrast were acceptable, with an acquisition time under seven minutes. Better contrast could be obtained by increasing the *TR*, but at the expense of increasing the imaging time. The final high resolution imaging protocol employed was a fast 3D, FSPGR (fast spoiled gradient echo) sequence, with *TE*= 4.2 ms fat/water in-phase, *TR*=25 ms, flip angle = 60 degrees, a 512 x 256 matrix and field of view =20 x20 cm^2, with an acquisition time of 6.50 minutes

4.2.2 Preliminary *In Vivo* Study of Breast Tissue

With the subject in the prone position and using the dedicated breast coil, images obtained using the optimized MR imaging protocol (sequence # 5 in table 4.1) are shown in figure 4.2.

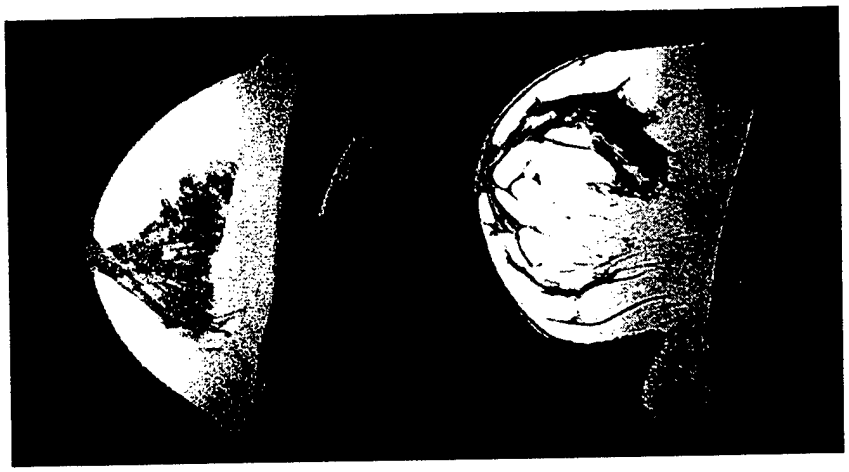

(a) (b)

Figure 4.2 MR sagittal views of the right breast for two subjects using HR optimal protocol. (a) has denser breast tissue than (b).

To reduce artifacts due to respiratory and cardiac motion, the frequency encode direction was placed in the anterior-posterior (A/P) direction and the phase encode direction to the superior-inferior (S/I) direction. The adipose tissue appears brighter with a high SNR. Glandular tissue has low signal and appears darker. The images shown in figure 4.2 were obtained from two different subjects and the high resolution MR images are clearly distinguishable, each displaying unique anatomical features. The subject in figure 4.2(a) has more glandular tissue that is more symmetrical in shape. The subject in figure 4.2(b) has less glandular tissue and more adipose. Also, the glandular tissue has a less symmetrical and more spiculated appearance in figure 4.2(b). The difference in age

between the two subjects is about four years and yet there is great variability in the amount and composition of the breast tissue.

4.2.2.1 Breath Hold Imaging

As stated before, initial imaging studies involved imaging the breast in the prone position (called the normal or undeformed state) using a commercial breast coil. In order to image the breast in a deformed state, the subject was placed in the supine position and imaged using a body coil. The supine (or deformed) image of figure 4.2(b) is shown in figure 4.3.

Figure 4.3 Supine (or the deformed) image of figure 4.2(b). Image shows aliasing and wrap-around effects due to cardiac and respiratory motion

Supine images exhibit large gross deformation but have low SNR, due to the lower sensitivity of the body coil. Supine images appear noisy because of motion artifacts due to cardiac and respiratory motion. In order to reduce the motion artifacts of the supine deformation MR images, several acquisition protocols and pulse sequences were explored for breath-hold imaging. Breath-hold imaging requires very fast pulse sequences that permit image acquisition in less than 30 seconds.

With the 3D fast gradient echo imaging sequence #4 shown table 4.1, the breast was imaged for 30 seconds with the subject holding her breath for 15 seconds. Twelve slices with 0.31 x 2.5x 2.0 mm voxel size were acquired simultaneously for both breasts. The SNR in these images was poor. Images were also obtained with a *T1* weighted fast spin echo sequence using *TE's* of 500 ms and 17 ms, an echo train length of 4, and a voxel size of 1.2 x 1.17 x 5.0 mm. While the FSE (fast spin echo) approach appears to be more promising, none of these sequences gave satisfactory results for our purposes. Further studies are indicated to improve SNR and image quality by using faster techniques. Such techniques may include faster 3D gradient echo sequences, improved fast spin echo sequences, or echo planar imaging (EPI) sequences. With such techniques, it would be possible to either increase the spatial resolution or to speed-up image acquisition, or both. Therefore such methods may provide high quality breath-hold breast imaging. Furthermore, SNR in breath hold imaging could be enhanced by using various types of coils to improve the signal.

Although the OSU MR system was updated during the course of this research with faster gradient hardware and imaging sequences such as EPI, no further study into improving breath hold imaging was done because the focus of the deformation study shifted from prone-supine deformation to uncompressed-compressed deformation.

4.2.3 Initial Compression Studies

Initially, in order to image deformation of the breast due to compressive forces, studies were performed using the commercial breast coil and Pyrex plates to compress a single breast in the cranial caudal (CC) and medial lateral (ML) directions. Because of the curvature of the breast coil, it was difficult to compress in the CC position, however large local deformations were clearly visible in the ML compression images. With the commercial breast coil, it was also difficult to supply incremental compressive loadings. Because of these findings, we decided to design an imaging device that would permit controlled, incremental changes in deformation of the breast.

4.2.3.1 *Design of Coil Holder and Compression Device*

We began the design of the imaging and compression device by testing a 16.5 cm x 15 cm flat surface coil in a quick and simple method. The coil was placed between Plexiglas plates and a single breast, positioned directly above the coil, was imaged with

the subject lying on her side. The subject reported this positioning as comfortable. Using a fast 3D GRE sequence, with TE= 4.2 ms fat/water in-phase, TR values of 19 ms and 30 ms (TR = 30 ms provided images with more signal), and a slice thickness of 2 mm, high SNR images were obtained.

Anatomical features were clearly identifiable on these single coil images, and artifacts due to respiratory and cardiac motion were minimal, although some aliasing was observed. Chemical shift at tissue boundaries in the S/I frequency encode direction was also observed, but did not appear to be problematic. Signal intensity drop-off with distance from the coil was also observed. This signal profile is exhibited in figure 4.4.

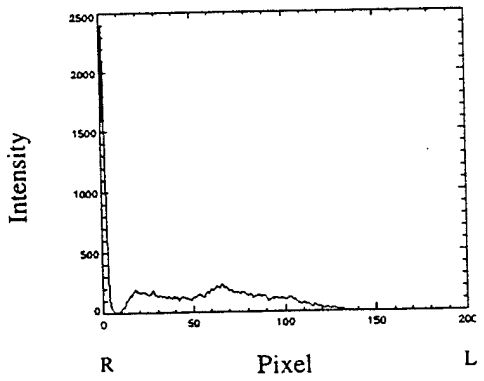

Figure 4.4 Histogram of RF surface coil image showing the intensity profile in the M/L direction

The mean of the intensity falls from about 145 to 40, thus some anatomical information is not visible. This intensity drop-off is typical of flat surface coils and the signal correction is addressed in section 4.2.3.2. This simple study indicated that a flat surface coil could provide suitable imaging of the breast, and that a single surface coil was sufficient for breast imaging since high resolution images could be obtained.

The next step in designing the imaging compression device was to determine the optimal positioning of the imaging coil. Since multiple breast compressions and MRI acquisitions were necessary and patient motion had to be limited, subject positioning and comfort had to be taken into consideration in designing the compression device.

For the positioning, shown in figure 4.5(a), the subject lies on her side with the upper body slightly elevated. The surface coil is placed on the bottom plate and the breast lies above the surface coil. This allows full coverage of a single breast and provides medial-lateral compressions only. It was decided to perform medial-lateral (M/L) compressions since subjects experienced less discomfort with this positioning. The specially designed coil holder and compression device is shown in figure 4.5(b).

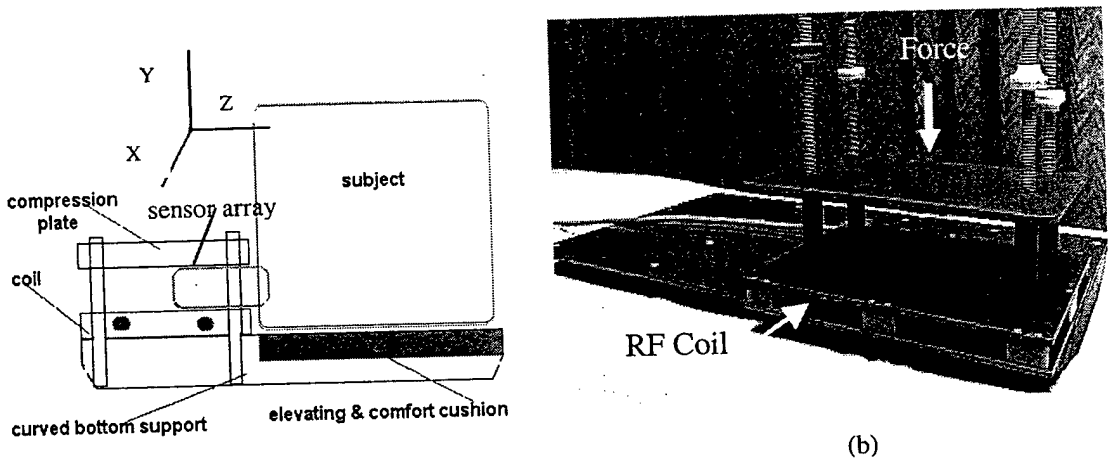

Figure 4.5 (a) Schematic of imaging-compression device (b) Photo of coil-compression device designed to perform medial-lateral compression and whole breast imaging.

The top compression plate moves vertically along posts to supply a uniaxial compression force, and the imaging is done by a receiver-only flat surface coil, which is attached underneath the bottom plate of the compression device. Mechanical stops control the compression and deformation width. Both plates contain a series of registration fiducial markers to localize landmarks and register images.

The top compression plate is positioned on the breast to be imaged, with its edge against the rib cage. This movable top plate pushes lightly into the chest wall and separates the left breast from the right breast to allow full coverage of only one breast. As

shown in figure 4.5(a), the surface coil is placed so that it rests up against the side of the chest wall beneath the breast, and the breast lies close to the surface coil.

Using the mechanical stops to control the distance between the top compression plate and the bottom plate, subjects could be imaged with a range of compressions. The mechanical stops ranged in height from 5.08 cm (2 inches) to 11.43 cm (4.5 inches). With these compression levels, no discomfort, other than that due to the need to remain immobile for the duration of the study, was perceived by the volunteers.

4.2.3.2 *Signal Correction Algorithms*

As mentioned earlier, a disadvantage of imaging with a single surface coil is signal drop-off. High signal intensity is observed on the MR images along the edge of the coil. Flat surface coils are known to produce spatial intensity variations, which can complicate image segmentation and visualization. Signal corrections are possible by filtering out the transfer function of the coil.

The inhomogeneous signal sensitivity profile of the RF surface coil produces intensity variations that spatially lower contrast and limit optimal display. Because signal intensity varies with distance from the coil, some anatomical features are not clearly distinguishable on images. Furthermore, the large signal variation is prohibitive for

automatic image processing and image segmentation, which rely on signal intensity. Signal correction is possible by dividing out the transfer function of the coil such that,

$$\hat{I}(x,y) = \frac{I(x,y)}{h_{cp}(x,y)} \qquad \textbf{4.3}$$

where $\hat{I}(x,y)$ is the corrected image, $I(x,y)$ is the original image and $h_{cp}(x,y)$ is the estimated surface coil's sensitivity profile.

Initially a low pass filtering technique [Murakami 1996] was used to estimate h_{cp}. As shown in figure 4.6, with this method some signal correction is observed but the contrast is still low. This method also introduces additional noise into the image. This extra noise is probably due to the fact that the existing noise is divided by small numbers.

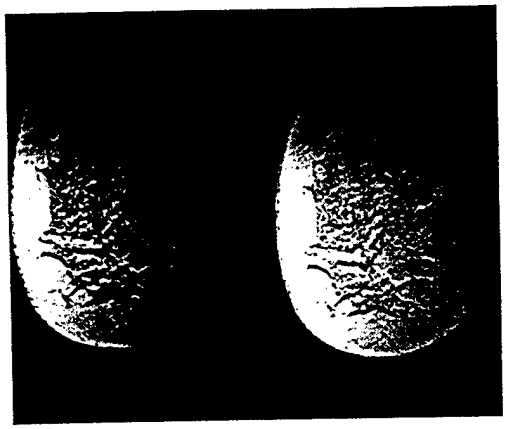

Figure 4.6 Surface intensity correction using a hanning filter. Surface coil image on the left, corrected image on the right.

Another correction technique was developed to compensate the surface coil images and increase tissue contrast. The new method used a homogeneous phantom and patented external markers [Charakes, 1998]. External registration markers were placed on the plates of the compression device and h_{cp} was found from images of a uniform gelatin phantom, such that h_{cp} = the phantom image. The phantom images were smoothed with an averaging filter to help reduce noise, and the images of the breast and the phantom were aligned slice by slice using the external markers. An example of the image correction with this method is shown in figure 4.7. It should be noted that if the uncorrected image is smoothed before applying the Hann filter, noise can be reduced and the former correction method yields results similar to the latter phantom technique.

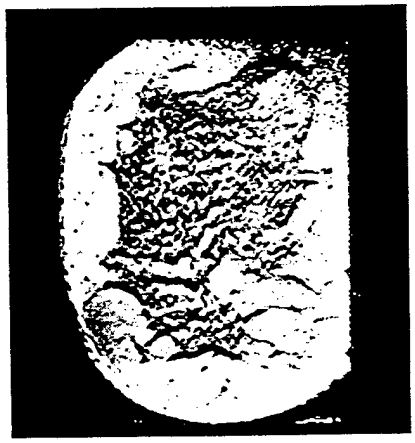

Figure 4.7 Breast image illustrating surface coil intensity correction using fiducial markers and uniform phantom.

4.3 Landmark Selection and Registration

The long term goal of this research was to map displacement of individual tissue regions between the uncompressed and compressed breast and at different compression levels. In this thesis, we explored various approaches as of how this mapping might be accomplished, which involved localization of external and tissue internal landmarks. Internal anatomic landmarks were identified in the human breast and fiducial markers were investigated for their use as external landmarks.

Further, it was necessary to separate displacement due to elastic compression from displacement (translation, rotation) due to subject movement. A rigid image registration algorithm was explored for this purpose. Criteria for the selection of external and internal landmarks and rigid registration are discussed in this section.

4.3.1 Internal Landmarks

The initial MR images indicate that anatomy characteristics suitable for landmark identification were best observed on high contrast *T1* weighted, high resolution images. In anatomy, landmarks are characterized as points that have anatomical names, such as nipple, as well as other geometric locations [Bookstein, 1991]. Landmarks are used to link the geometry of the data, the mathematics of deformation and the forces which act on

the landmarks. The three principal types of landmarks used in biology are: I.) juxtapositions of tissues, (*e.g.*, points in space at which three structures meet), II.) maxima or minima of curvature, such as tips of extrusions and valleys of vaginations, and III.) extremal or tangential points. These three landmark types are shown below in figure 4.8

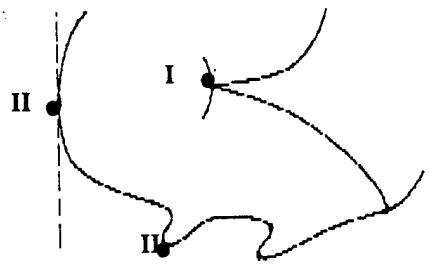

Figure 4.8. Three types of biology landmarks used as internal anatomy landmarks. Type I: Tissue intersections; Type II: Points of curvature; Type III: Tangential points.

Anatomical features such as the rib cage, fatty tissue, boundaries between glandular and fatty tissue and the nipple were used to define internal tissue landmarks, because these features are clearly distinguishable on the MR images. The corresponding landmarks are found in both the undeformed and deformed breast images.

4.3.2 External landmarks

Various MR-visible materials that could be safely placed on the surface of the breast were investigated as potential external landmarks. Besides acting as localization markers, external landmarks also serve as fiducial registration markers and have to be convenient enough to be arranged in a mesh or grid pattern.

Various materials, which could be safely placed in an MRI system, were tested to ascertain their suitability as positional markers. Among the materials tested for suitability as landmarks were vitamin E capsules, lip balm, water-based paints, paints with metallic content, and metallic stickers. These materials were placed on a gelatin surface and imaged with *T1* and *T2* weighted spin echo and gradient echo MR imaging sequences. Materials such as the capsules and the lip balm contain a large oil content that increases the signal intensity on MR images, so that such materials appeared very bright. The materials with metallic content cause susceptibility effects on the MR images and generate small local signal voids.

In the phantom tests using the prosthesis breast model, the model was marked with both the vitamin E capsules and the metallic polish. Figure 4.9 shows two slices of the prosthesis with vitamin E capsules. The oval-shaped vitamin capsules were taped in a grid pattern to the elastic surface enveloping the prosthesis. The metallic polish was

placed in a grid pattern, with lattice points about 2.5 cm (one inch) apart, on both the inner (chest wall) and outer sides of the prosthesis. The model was imaged in the supine position with a T1 weighted spin echo sequence. The vitamin E markers provide a large signal-to-noise ratio, and are good identifiable landmarks. However, the size of the capsules, (3mm), makes for a bulky grid.

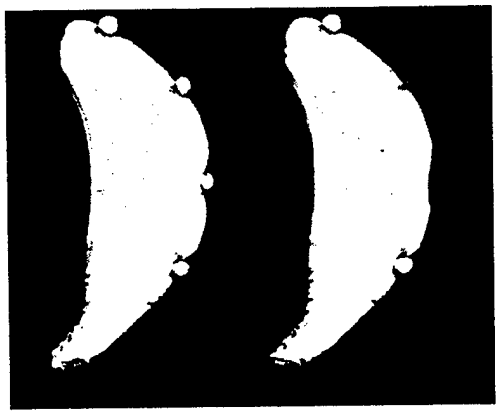

Figure 4.9 Deformable prosthesis with vitamin E external markers. The markers appear as very bright oval objects

With the metallic polish, the voids due to signal aliasing are a problem when the size of the polish points are about 5 to 10 mm. When this happens, the signal starts to overlap, creating voids that are much larger than the lattice points of metallic polish. This problem was solved by using smaller spots of polish and making the grid lattice points wider than one inch apart. Thus the initial tests indicated that the nail polish containing

metallic material was the most suitable external marker, both in terms of marking out the various grid points and for the size of local changes.

In the human breast studies, the metallic polish was brushed onto adhesive bandages and placed in a circular pattern around the breast. The size of the polish point on the bandage was about 2 mm, and the size of the signal void was about 4 to 6 mm. An image of the breast with the metallic polish is shown in figure 4.10.

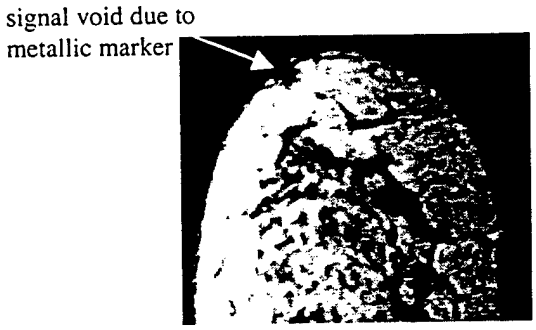

Figure 4.10 Human breast with metallic markers placed on the surface. The small signal voids are due to the external markers.

As discussed earlier, fiducial markers were placed on the breast and the compression plates (top and bottom). From the MR images, it was easy to locate the fiducial markers. Typically six to eight adhesive markers were placed on the breast in a circular pattern, but only two to three could be seen in the same plane (*i.e.*, on the same MR slice at the same A/P position) as the fiducial markers on the plates, see figure 4.11.

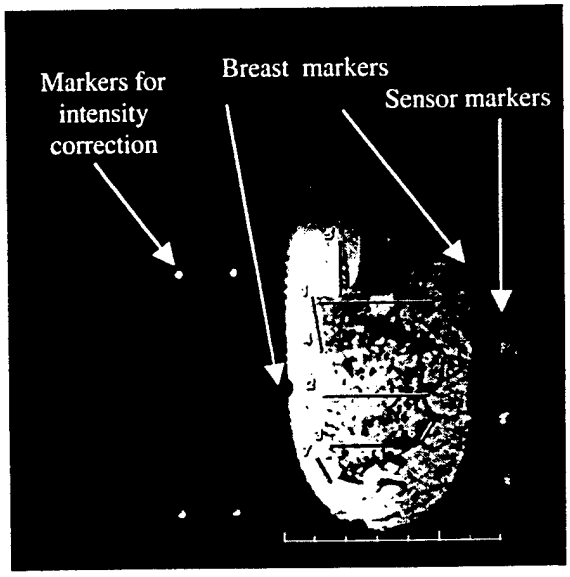

Figure 4.11 Image showing the external markers on the compression plates and the breast in the same A/P plane. The top plate markers are not always visible in the same plane as the breast markers.

The external registration markers for the intensity correction algorithm, discussed in section 4.2.3.2 were placed on the bottom plate and are seen as bright dots to the left of the breast image. The larger dots to the right of the breast are the markers placed on the top compression plate. These markers also helped to localize the individual sensors in the sensor array.

4.3.3 Image Registration

As mentioned above, displacement due to subject motion has to be separated from that due to compression. Although steps were taken to limit subject movement, some finite motion was unavoidable. Therefore, in order to ensure that tissue displacement was due to the external compression force and not to subject movement, a registration technique was employed.

The matching of two or more images acquired at different times or from different imaging modalities is an important research topic in biomedical imaging. The matching or aligning of images is known as image registration. Besides integrating image information from different imaging modalities, image registration can be used to study the growth or movement of tissues and organs and to correct for displacements and rotations due to gross patient movement over the course of multiple image acquisitions.

Image registration has become an useful clinical tool in noninvasive medical imaging. For example, by matching images acquired using computer tomography (CT) to those acquired using MRI, improved diagnostic information can be obtained. Also, in breast cancer imaging the matching of serial mammograms, obtained over the years, has proven very beneficial in detection and diagnosis of lesions.

A variety of registration techniques has been developed over the years. For most practical needs, registration methods should be accurate, insensitive to noise, applicable to many modalities and robust. Registration falls into two categories, rigid registration and nonrigid (or elastic) registration. Rigid registration employs rigid transformation algorithms of rigid body theory, and elastic registration utilizes deformable body theory.

Two dimensional image registration can be divided into three techniques. They are 1) intensity based methods, 2) feature based methods, and 3) elastic model based methods. Most registration techniques have a combination of the methods. Intensity based methods include the Fourier transform, correlation and voxel similarity techniques. Such methods can align similar contrast images with subpixel accuracy, but are limited by their sensitivity to variations in illumination between the images [Alexander, 1996, Liang, 1997, Lu 1999]. For feature based techniques, significant image features must first be extracted and used for matching, such as control point pairing. This method is limited by the necessity for features that are invariant to external conditions and that can convey information about the object being imaged. Rigid registration methods are based on intensity and feature methods only.

Nonrigid registration, known as elastic registration, allows nonrigid transformation and yields better results than rigid registration techniques [Lu, 1999]. However, elastic registration methods require some pre-alignment by rigid

transformation to remove large differences. The elastic registration approach can be extended to 3D registration, such as in brain tomograms. Several elastic registration methods in the literature are surface based techniques and physically based techniques [Pecker, 1999]. In surface based techniques, the deformation of the volume of the original object is interpolated to agree with precomputed surface warps.

In physically based techniques, the nonrigid transformations are modeled as deformations of elastic materials such as solids or fluids [Pecker, 1999]. In such registration, physical parameters such as force, displacement, or strain, are derived from the image data and then applied to deform the source image until it aligns with the target image. It must be noted that usually the physical forces are not *true* forces but are convenient to use to make smooth transformations. Such transformations, however, follow the valid mathematical principles of the hypothetical forces.

For the registration of our coronal images, we employed a robust, rigid, 2D featured based technique that matched external (fiducial markers) and internal (anatomical features) landmarks between images. The method was based on the Procrustes rigid body approach, which finds the least squared solution by minimizing the root mean square distance among all of the paired landmarks. The equations for the registration technique are expressed in equations 4.4 to 4.11. The minimization of error of the sum of squares (MSE) of the distances between paired points, P_{1i} and P_{2i} (where

x_{1i}, y_{1i} and x_{2i}, y_{2i} are the coordinates) in the compressed and uncompressed images is expressed as

$$\sum_{i=0}^{n-1} \left(x_{2i}\cos\theta - y_{2i}\sin\theta + t_x - x_{1i}\right)^2 + \left(x_{2i}\cos\theta - y_{2i}\sin\theta + t_y - y_{1i}\right)^2 \qquad \textbf{4.4}$$

where t_x and t_y are the translations in the x and y directions respectively, θ is the angle of rotation, and n is the number of points used (i = 0 to n). Minimizing the error by a least squares approach yields,

$$t_x = (X_1 - X_2 \cos\theta + Y_2 \sin\theta)/n \qquad \textbf{4.5}$$

$$t_y = (Y_1 - X_2 \sin\theta + Y_2 \cos\theta)/n \qquad \textbf{4.6}$$

and

$$\tan\theta = (X_1Y_2 - X_2Y_1 - A)/(-X_1X_2 - Y_2Y_1 - B) \qquad \textbf{4.7}$$

where

$$X_1 = \sum_{i=0}^{n-1} x_{1i} \qquad X_2 = \sum_{i=0}^{n-1} x_{2i} \qquad \textbf{4.8}$$

$$Y_1 = \sum_{i=0}^{n-1} y_{1i} \qquad Y_2 = \sum_{i=0}^{n-1} y_{2i} \tag{4.9}$$

and the constants A and B are defined as

$$A = \sum_{i=0}^{n-1} \left(x_{1i} y_{2i} - x_{2i} y_{1i} \right) \tag{4.10}$$

$$B = \sum_{i=0}^{n-1} \left(x_{1i} x_{2i} - y_{2i} y_{1i} \right) \tag{4.11}$$

As an example, the transformations between the undeformed state and the first compression obtained using the coordinates of the fiducial markers of visually matched coronal slices of are given in table 4.2.

Table 4.2 Transformations using rigid registration technique				
Exam #	Direction	Subject A	Subject B	Subject C
t_x (cm)	R/L	0.46	0.10	0.48
t_y (cm)	S/I	1.37	1.3	1.5
θ	n/a	1.95°	0.58°	0-2.2

Table 4.2 Transformations using rigid registration technique

In all cases, subject motion appeared to be less between images at different compression levels. As can be seen from the tabulated data, motion in the R/L (medial-lateral) direction and rotation are minimal. This is expected since with the compression-imaging device placed inside the bore of the MR magnet, the degree of movement is very limited. The fact that the translation value (1.3 – 1.5 cm) in the S/I direction is about the same for subjects indicates that there is negligible subject motion in this direction. Recall, translation in the A/P direction (t_z) was obtained manually by visually matching slices so that t_z = 0.21 mm, 0.42 mm and 0.7 mm for subjects A,B and C, respectively.

Full registration of deformed breast images will ultimately require 3D elastic registration. However, the aim of the work in this thesis was to explore how far simple rigid registration could go as initial correction prior to initial determination of displacement. To further simply the problem, coronal slices were visually matched (*i.e.*, z-translation) and a 2D in-plane rigid registration algorithm used.

4.4 **Quantification of Tissue Deformation Using MR Images**

The mechanical complexity of breast tissue is clearly represented on the sectional MR images. Substantial tissue deformations are observed even under the mildest of compression. We examined deformation between prone-supine views and uncompressed-compressed views. Examples of prone-supine deformation are shown in figures 4.2 and

4.3. Prone-supine deformation is extremely large and although some internal landmarks are distinguishable, it is difficult to accurately map corresponding landmarks between the images. Because of this, it was decided to use small incremental compression deformation to analyze the material properties of breast tissue. With the mechanical stops the right breast was deformed (*i.e.*, compressed) so that the breast thickness ranged from 35 cm to 60 cm. The thickness can be related to the percent of compression, that is the amount of deformation from the original undeformed state. The overall breast thickness and percent compression or deformation in the medial-lateral direction obtained for different subjects are given in table 4.3.

Table 4.3 Total Deformation in Direction of Compression				
Subject	A	B	C	D
Uncompressed width (mm)	55	77	85	66
Compressed width (mm)	35	57	60	48
% Compression	36	26	30	27

Table 4.3 Total Deformation in Direction of Compression

The uncompressed-compressed deformation is shown in figures 4.12 and 4.13. Figure 4.12a demonstrates in sections near the nipple where compression is the least, that the tissue appears to have rotated. Similar rotation is observed in most subjects. This specific type of movement is assumed to be associated with medial-lateral compression because in this direction, the entire medial surface of the breast is not always in direct

contact with the surface of the compression plate. However, the contact area increases with deformation (*i.e.*, compression). Shown in figure 4.12b are MR sections closer to the chest wall, where tissue deformation is clearly distinguishable.

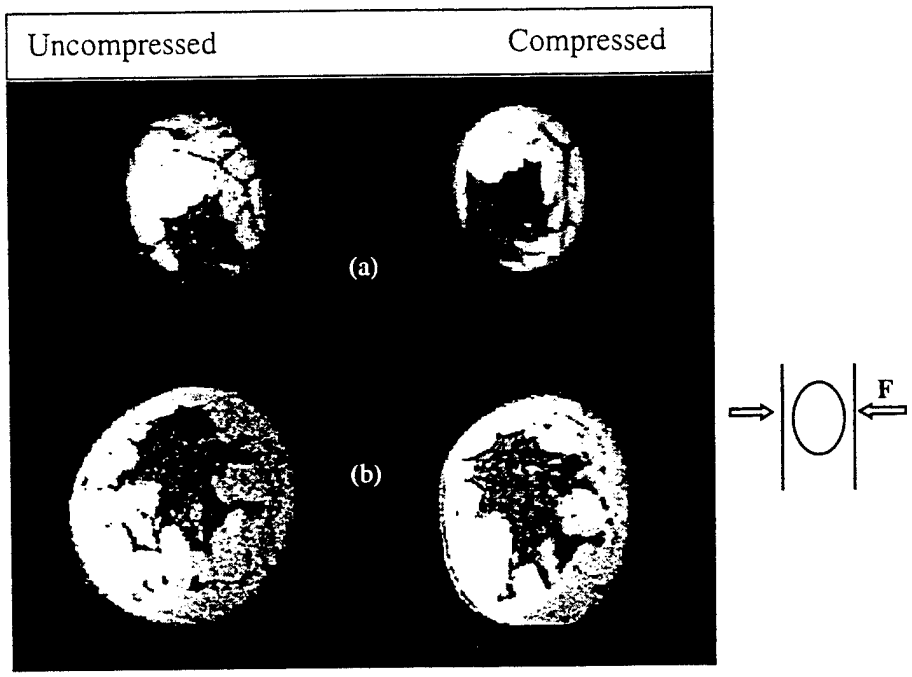

Figure 4.12 (a) Anterior views (near the areola) of sectional MR images. (b) posterior views (closer to chest wall) depicting tissue deformation under mild static compression. (side diagram shows force loading geometry.)

The overall compression (or deformation) in figure 4.12 is about 26%, and the tissue displacement is substantial, although not as large as that of prone-supine deformation. Figure 4.13 shows the deformation for small incremental compressions of

5% to 20%. With small incremental deformations (<10 % in thickness), corresponding tissue internal landmarks can be easily mapped between deformed (compressed) and undeformed (uncompressed) images.

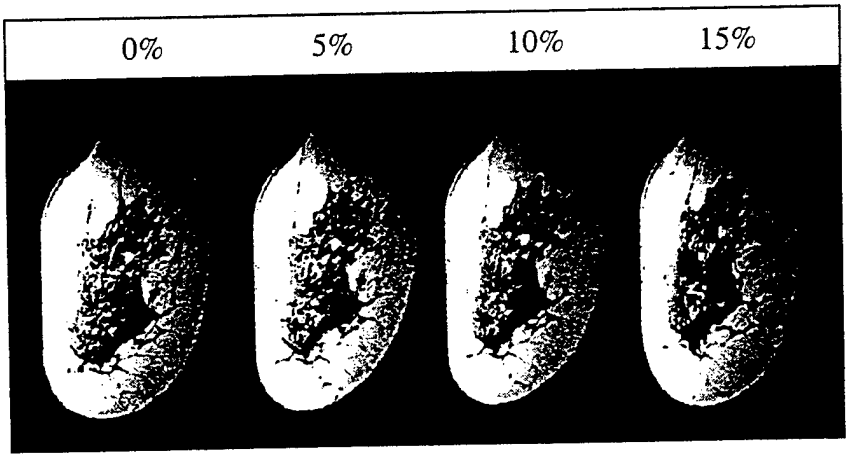

Figure 4.13 Images of varying amounts of compression, from 5 to 15 % obtained by adjusting width of the compression device from 4 to 3 inches in incremental steps of 1/4 inch.

4.4.1 Initial Attempts to Visualize 3D Displacement

The initial data indicated that tissue deformation occurs in three dimensions. Thus we attempted to use three dimensional volume visualization to identify internal landmarks in 3D. Several methods of 3D volume visualization were investigated to determine which technique would best represent breast tissue. We found that the interactive visualization software, the Visualization Toolkit (VTK version 2.0, Kitware,

New York, 1996), provided a versatile approach to rendering medical MR datasets. VTK is an object oriented software package that uses both C and TCL programming languages. The programs used to generate the volumes are given in the appendices.

The image in figure 4.14(a) displays a sagittal section of the entire breast obtained with a ray casting volume rendering technique. In such a method, rays are cast for each pixel in the image plane through the volume to compute pixel values. The basic idea is that the value of each pixel in a rendering is determined by sending the ray through each pixel in a volume and the data encountered along the ray are evaluated. Although the representation using this technique is a good display of the breast volume, it is not found to be appropriate for obtaining displacement data because it does not display out of plane branching of the ductal systems.

In order to better visualize the tissue, our next step was to segment the glandular tissue. Since the adipose tissue has a higher signal than the glandular tissue, this tissue was segmented by a thresholding technique to produce 3D representation of glandular breast tissue. The segmented tissue was volume rendered to produce several different representations. Figure 4.14(b) shows coronal sections of compressed and uncompressed 3D views of segmented data. This volume rendering is performed with the ray casting technique. With this method, the tissue is too dense to adequately locate landmarks, although some extrusion peaks are displayed.

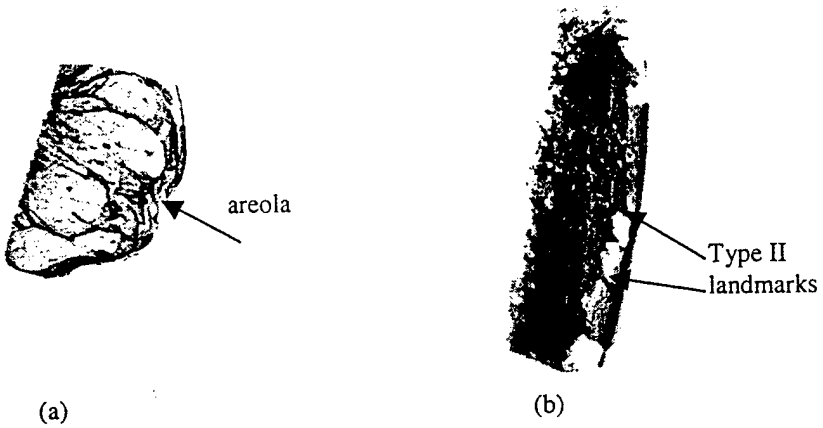

Figure 4.14 (a) Three dimensional representation of selected volume of breast tissue using a ray casting technique. (b) Three dimensional representation of segmented breast tissue using ray casting technique.

Figure 4.15 shows a polygon rendering of the volume of breast tissue in which the volumes are displayed as isosurfaces using the marching cubes algorithm [VTK, Version 2.0, Kitware, New York]. This algorithm is a contouring algorithm that creates 3D contours known as isosurfaces. Basically, the data are contoured and boundaries between regions are created. Each boundary corresponds to a surface (3D contour) of a constant scalar value. This type of rendering offered the best 3D visualization of breast tissue. The out of plane branching of the ductal system is clearly represented in these images. Note that individual ducts cannot be resolved, but the system branching away from the areola is observed. The 3D rendering is very similar to a cross sectional anatomy view of breast tissue.

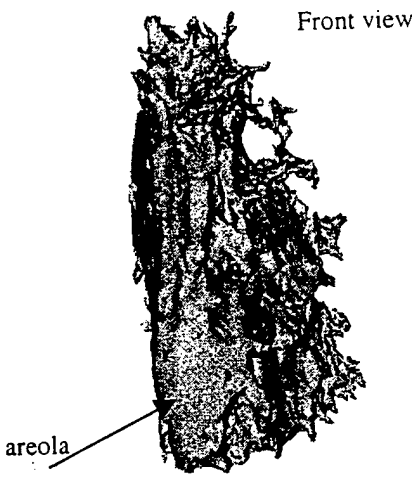

Figure 4.15 Three dimensional representation of segmented breast tissue using marching cubes algorithm. Best representation of breast tissue that shows how the tissue branches away from the areola. Image is similar to cross-sectional anatomy images of breast tissue.

4.4.2 **Displacement Vectors**

As can be seen from the volume renderings, identifying appropriate 3D landmark features from the segmented data is a challenge. Type II landmarks (*i.e.*, extrusion peaks) are distinguishable and are easy to identify in both the uncompressed and compressed volumes. Several such landmarks were selected and manually mapped between uncompressed and compressed volumes for three different compressions of approximately 5%, 10%, and 15%. For more displacement accurate results, the different deformations were registered with the rigid registration technique. Using these

landmarks, the components of the displacement vector, $\boldsymbol{D}$, between the coordinates of the original landmark, P, to the new coordinates of the displaced landmark, P', were calculated. Recall from chapter three, that the components of the displacement vector are $u = x' - x$, $v = y' - y$, and $w = z' - z$. The coordinate system is defined such that compression is in the y direction (medial-lateral orientation). The x axis is in the subject's inferior to superior direction, and the z axis points from the nipple to the chest wall (anterior – posterior direction, see figure 4.5(a)). In the y direction, a negative v value represents displacement opposite to the direction of the applied compression force, (that is, the displacement is elongated instead of contracted or compressed). Along the x and z axes, negative values of u and w represent displacement that increases from an arbitrarily chosen origin.

Graphs of the x, y and z components of the displacement vector are shown in figure 4.16. The graphing of the components of the displacement provides quantitative information into the 3D compression displacement. The graphs show that as compressive loads increase, more contraction (or compression) is observed along the y (medial-lateral) direction. In the superior-inferior direction, the x displacement is observed to decrease as the applied loading increases. As we shall show in chapter five, this is similar to what occurs for transverse strain. The z displacement (*i.e.*, anterior-posterior, out-of-plane deformation) is more complex and significant. It was once assumed by earlier works in soft tissue mechanics, that this displacement could be neglected [Gallagher,

1982, Park, 1992, Sumi, 1995]. As observed, even for small compressions with the breast compressed <15%, the out-of-plane displacement can be large.

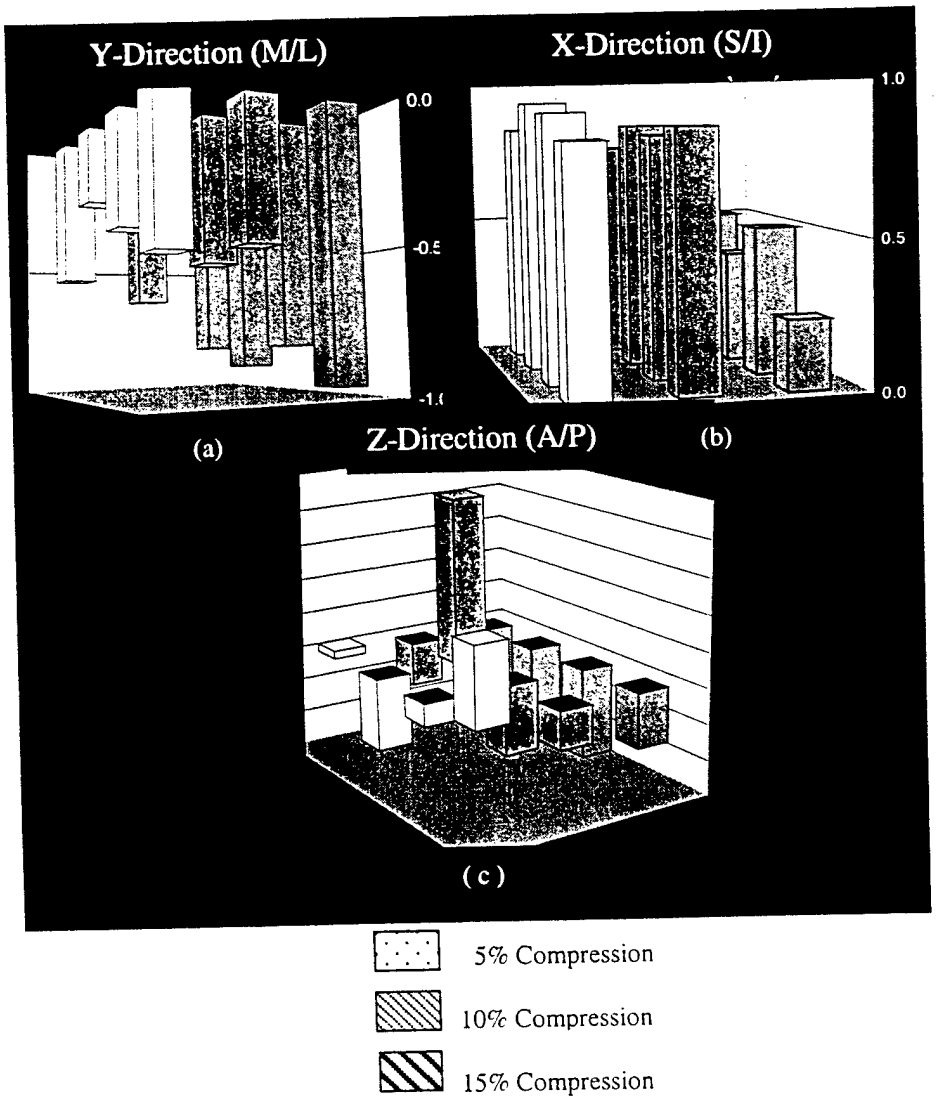

Figure 4.16 Components of displacement vector (a) in the direction of compression, (M/L, medial/lateral); (b) in the transverse (S/I) direction; and (c) in the out-of-plane (A/P) direction.

Localization of internal anatomy, using the external landmarks, has been very promising. From the initial deformation data, we found that MR imaging can provide *in vivo* biomechanical information about the breast when incremental compression is used. We observed that because of the connectivity of the duct system, shear deformation occurs at regions far from the point of contact of the applied force.

Our initial attempts to use displacement vectors to obtain 3D strain data has been very useful in so far as it illuminates the complexity of the problem and can assist and direct future research. From our initial study it is clear that full 3D elastic registration algorithms are needed. Finding matching paired points in the corresponding volumes was difficult to accomplish, and the use of the rigid image registration method and not a more accurate elastic registration technique introduced some error in displacement measurements. Without elastic registration, the selected internal landmarks on the 3D rendered volumes were not always invariant to stimuli other than the external compressive force, and it is very difficult to manually locate internal landmarks. We chose therefore to use the stretch ratio, λ_i to measure the displacement and SEDF theoretical models estimate the 3D stress. By using line segments to evaluate the stretch ratio, error due to image registration was overcome because of the invariant properties of lines.

CHAPTER 5

IN VIVO STRESS STRAIN ANALYSIS

With the design and development of the MR compatible RF coil and compression device completed, preliminary force-deformation studies of the breast were initiated. The compression device deformed the breast in the medial-lateral direction with a static uniaxial compressive force. From this configuration, the stretch ratio λ (*i.e.*, displacement in the ML direction) and the corresponding axial stress, σ_y, of *in vivo* breast tissue were experimentally determined using pressure sensors and anatomical landmarks. The design of the uniaxial compression experiment was such that it could only accommodate the in-plane states of strain, (*i.e.*, the medial-lateral and superior-inferior directions).

To obtain the deformation data, the top plate of the coil-compression device was moved to a first position to obtain a total compression that was <10%, (*e.g.*, the breast was deformed such that thickness of the breast in the M/L direction changed only about 10%). With such small incremental deformations, corresponding internal anatomical landmarks could be mapped easily between sequentially deformed (compressed) and

undeformed (uncompressed) images. Furthermore, with these compressive forces no discomfort was reported by the subjects other than that due to the need to remain immobile for the duration of the study.

After compressing the breast, normal pressures (*i.e.*, force/area) measured by sensors placed on the surface of the breast were recorded and immediately following, the subject was placed inside the magnet bore and imaged for about seven minutes. This compression and imaging routine was performed for at least three different compressive steps on each subject. One hundred and twenty four coronal images of the breast were acquired, and regions of interest were manually localized using both fiducial markers and internal anatomical landmarks on both the uncompressed and compressed MR images. The volume of breast imaged was 20 cm x 20 cm x 8.4 cm, with the volume of interest typically extending from the areola to the middle of the breast in the anterior-posterior direction. Because of imaging artifacts due to cardiac and respiratory motion, images closer to the chest wall were too noisy to give any suitable data and were not used in the analysis.

5.1 Force-Displacement Studies

To measure the total force exerted by the top plate of the coil-compression device, (shown in figure 4.5(b)), weights in increments of 500 grams were stacked on top of the plate until the breast of a subject was compressed a specific amount. The total weight, including the weight of the plate itself, ranged between 2460 to 3960 grams (*i.e.*, 23.8 to 38.4 N). This total weight varied from subject to subject, as was expected, but positioning of the breast also played a significant role. As in mammography, subject positioning contributed to the amount of compressive force needed to obtain a specific deformation width or breast thickness. For instance, if the subject was placed so that some of the pectoral muscle was under the compression plate, then the total force increased. Also if such positioning occurred, patient motion was likely to increase because of the extra discomfort associated with this positioning.

We had sought to use the total compressive force across the top plate and the total area of the breast to evaluate the Cauchy or "true" stress (defined as the ratio of force to the deformed cross-sectional area of the breast). However, because of the variability of the total force, this stress could not be used in the stress-strain analysis.

To obtain a rough estimate of the force-deformation relationship of the breast, we used an approach similar to that mentioned above. We placed standard weights ranging

from 4.5 to 61.7 N on the top plate and measured the breast thickness. The force-deformation curves obtained from this experiment are shown in figure 5.1.

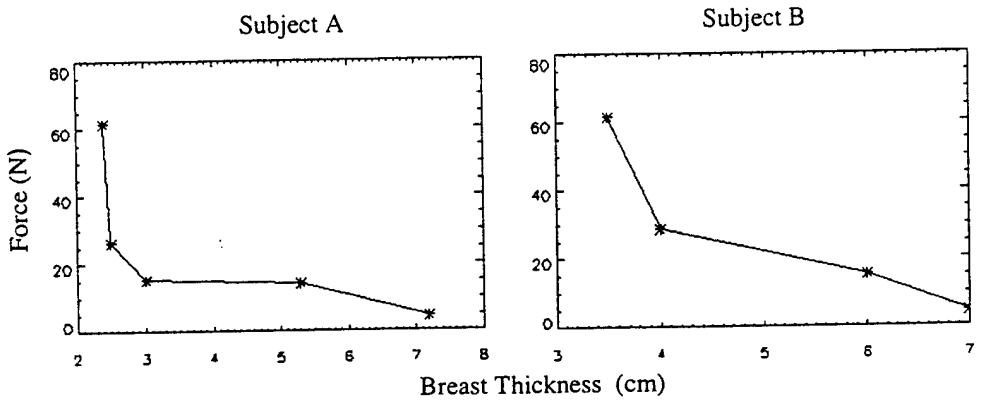

Figure 5.1 Force displacement curves of force versus breast thickness for two subjects, A and B. Subject A has denser breast tissue. The curves are nonlinear. * = experimental data points

The curves exhibit a nonlinear relationship, which indicates that the mechanical behavior is nonlinear. The compressive loads in this particular study were larger than those typically used with the coil-compression device, and thus gave us preliminary insight into the mechanical behavior of the breast at loads approaching those of conventional mammography.

5.1.1 Stress Sensors

To measure axial stress, various pressure and load sensors were investigated. Versatile, economic MR-compatible sensors were required because an array of sensors had to be capable of being safely placed into the bore of the imaging magnet in close contact with the skin without causing any harmful heating effects or introducing any large image artifacts (*i.e.*, susceptibility effects). Traditional load cells used to measure force and pressure are metallic, inflexible and costly. Miniature load cells can cost as much as $1,000 each. After much investigation into load sensors, we found the nonmetallic Uniforce© (Force Imaging Technologies, Chicago, IL) sensor to measure compressive pressure at various positions along the breast.

The Uniforce© sensor, as shown in figure 5.2a, is constructed of two layers of a nonconductive substrate, such as polyester or polymide film, with layers of a silver-colored conductive material applied to each substrate. The circular sensing area, which has a diameter of 6.35mm with an area of 3.16×10^{-5} m^2, is made of a pressure sensing resistive material. The conductive material extends from the sensing area to a connector assembly with conductive leads for connecting the sensor to a circuit. The standard sensor is 14 mm wide and 114 mm long.

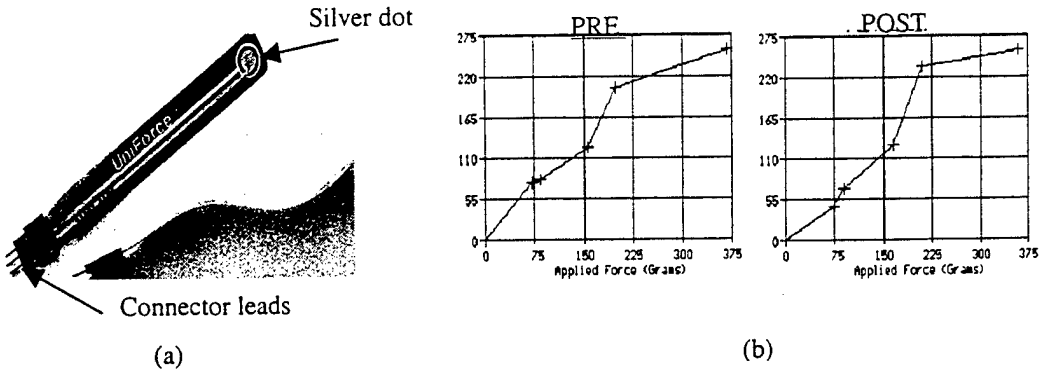

(a) (b)

Figure 5.2 (a) Pressure sensor. The silver dot is the sensing area of 3.1×10^{-5} m^2. The connector leads at the end cause MR susceptibility effects. (b) Pre and post imaging calibration curves.

The sensors are flexible, thin (about 0.076 mm), and capable of detecting static forces only. Sensors capable of detecting forces ranging from 2.2 to 4,448 N are commercially available. The sensors only measure forces normal to the sensing area, (*i.e.*, axial loads). Under the influence of an applied force, the resistance of the sensing material changes and the force can be measured by connecting the sensor leads to an ohmmeter and measuring the change in resistance. Alternatively, the sensor can be plugged into a parallel port input/output (PPIO) card in a computer to provide a convenient digital output, which is calibrated in units of pounds, grams or newtons.

For our experiments, we knew that our forces would be mild to moderate, so we used two sets of sensors with a force range of 0 to 2.2 N and 0 to 4.4 N. Before beginning the studies to measure pressure, sensors were evaluated to see if the sensors and connecting cables could be safely used in conjunction with MRI. Two main issues that needed to be addressed were that: 1.) alternating magnetic fields may produce currents and potentially harmful heating leading to skin burns, and 2.) the presence of conductors might lead to imaging artifacts.

To address these safety concerns, tests were conducted with two sensors taped to the hand of a subject, who had given informed consent. The subject's hand was placed inside a head coil and imaged for up to 6 minutes. The subject indicated no sensation of increased temperatures near the sensors, and no heat burns were observed.

To address the susceptibility issue, sensors with and without the connector assembly (consisting of the conducting leads and connecting cable wires) were attached to a gelatin phantom and imaged. The circular sensing area produced no effect, but small susceptibility effects, due to the conductive material on the substrate, led to signal voids of a few millimeters. For sensors with the connector assembly, 2 x 2 cm signal voids were observed. We concluded that for the *in vivo* stress studies, the sensor connectors must be at least 2 cm away from the breast.

Before MR imaging, sensors were calibrated and preconditioned with weights to obtain the typical calibration curve shown in figure 5.2(b). After imaging, the sensors were recalibrated and pre-imaging and post-imaging calibration curves were compared to verify that there was no damage due to the high magnetic field. The thinness and flexibility of the sensors permitted the sensors to be placed between the top plate of the coil-compression device and the breast. The sensors were adhered underneath the top plate so that the pressure sensing area of each sensor was in contact with the surface of the breast. Since the sensors could not be seen on the MR images, external markers were used to give the locations of the sensors on the MR images. Up to six sensors were used in the studies and sensor readings were recorded one at a time using a single cable that connected the sensor leads to the computer card.

As the width between the top and bottom plate decreased during incremental compressions, it became difficult to reach the connector leads of each sensor to attach to the cable of the PPIO card, because of the narrow gap between the plates. A switching assembly was designed to try to connect all of the sensors to the PPIO card, but this produced too much drift in the sensor measurements. Therefore the sensors had to be arranged in a pattern that could accommodate the size of the breast and yet allow for accessibility to the conductive connector leads. We tried various placements of the sensors, but found that a linear arrangement was our only option in terms of accessibility

of the connector leads, obstruction of the adjusting poles of the coil-compression device, and consistency in accommodation for varying breast sizes of the test subjects.

5.1.2 Pressure Distribution

Initially the linear set of sensors consisted of four sensors, two with a range of 0 to 4.4 N, and two with the range of 0 to 2.2 N. Since we did not know which range would be suitable for our experiments, we used both types of sensors. The data later indicated that for the external forces exerted on the breast by the experimental setup, sensors with a range of 0 to 2.2 N were sufficient. The sensors were numbered consecutively, starting from the superior position. The sensor set gave an estimate of the distribution of the total force that was exerted on the breast by the top plate. Table 5.1 lists force readings in grams. Force was obtained in grams because sensors were calibrated with standard gram weights. As can be observed, the force tended to decrease in the superior-inferior direction.

TABLE 5.1 Sensor Measurements for Compression Studies				
Compression Width		3.0 inch spacer	2.25 inch spacer	2.0 inch spacer
Sensor #	(S/I) location	Force (grams)	Force (grams)	Force (grams)
1A	S = 3 3.3 mm	4	5	16
2A	S = 16.9 mm	n/a	n/a	n/a
3A	I = 5.0 mm	3	4	15
4A	I = 24.9 mm	1	1	9
		3.75 inch spacer	3.0 inch spacer	2.25 inch spacer
2B	S = 23.4	0	1	14
3B	S = 2.3	4	2	13
		3 inch spacer	2.5 inch spacer	2.0 inch spacer
1C	S = 28.7	1	13 (11)	30 (31)
2C	I = 16.3	1	10 (4)	26 (15)
3C	I = 55.7	1	1 (0)	11 (9)

TABLE 5.1 Sensor Measurements for Compression Studies
Subjects, A, B and C; ( ) indicates readings from sensors on the bottom plate

The readings from sensor number two in the array on subject A were consistently zero, because the subject's breast never came into contact with this sensor. From this study it was noted, that positioning of the sensors would have to vary with the size of the breast and that sensors would have to be placed in a row. The sensors were fairly fragile, and we found that too much handling could easily damage a sensor. When sensors were moved to accommodate a larger breast, subject B, two of the sensors in the array failed because of damage. The readings from this study were inconsistent due to the damaged sensors. A later study was performed on subject C, with three sensors each on the top and bottom plates.

The force readings from the sensors were converted to axial stress, ($\sigma_y = \sigma_2$), using the equation

$$\sigma_y = \text{Force/Area} \ (N/m^2) \qquad 5.1$$

where area is the cross-sectional area of the sensor. As defined in chapter 3, the axial stress is similar to the nominal stress, which is defined as the ratio of the force to the original cross-sectional area [Farshad *et al*, 1998, Mendis *et al*, 1995].

Since only two to three data points were obtained from the initial force measurements, these force data in the S/I direction were interpolated to provide an estimation of a distribution curve of the force with respect to position along the breast. A quadratic interpolation was used according to the schematic outlined in figure 5.3(b). The coronal images were reformatted, (see figure 5.3 (a)), to depict the sagittal slice of the volume directly underneath the top plate, and points, in the superior-inferior direction, at which the contact between the plate and breast went to zero were used as boundary-end values. Since the theoretical distribution function is continuous, then the function goes to zero at the end points, such that $f(x_+) = f(x_-) = 0$. The pressure distribution curve is shown in figure 5.3(c).

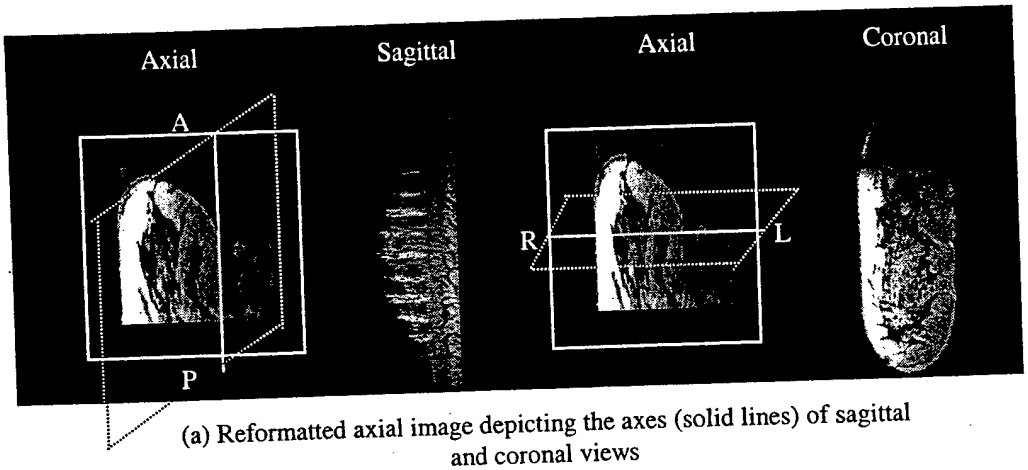

(a) Reformatted axial image depicting the axes (solid lines) of sagittal and coronal views

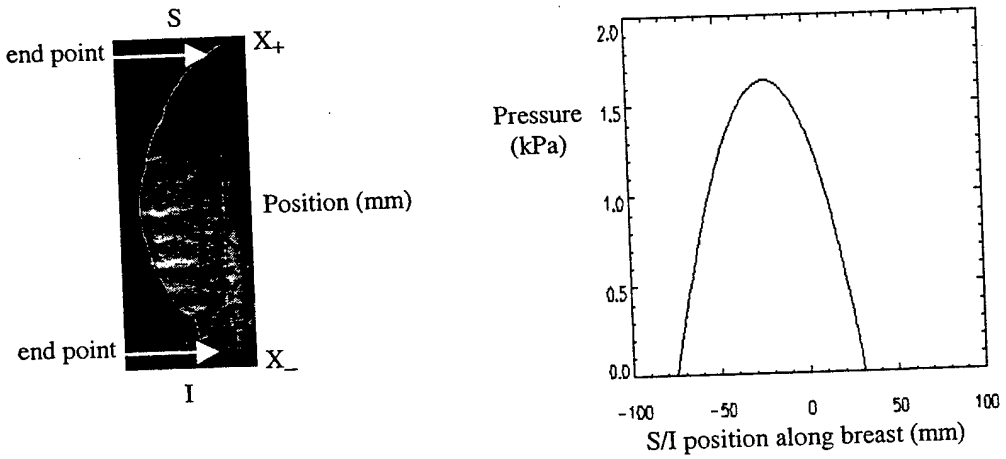

(b) Schematic and plot of pressure distribution along the S/I surface

Figure 5.3 (a) Reformatted images of Exam 3032, Subject A, depicting axial, sagittal and coronal sections. (b) Sagittal MR slice of the breast that is in contact with the top compression plate, and plot of force (pressure) distribution function.

5.1.3 Strain Analysis

The next step in the force-deformation analysis was evaluation of the strain from the displacement of regions of interest. Line segments in the region of interest were used to analyze displacement because of their invariance to patient motion. The invariant properties of line segments include the line ratio and the line angle ratio. Strain, ε, was calculated using the ratio, λ, of the length of line segments between matched points in corresponding (*i.e.*, matching compressed and uncompressed) MR images. As shown in figure 5.4, the paired end points of the line segments were tangential points and juxtapositions along the boundary of the glandular tissue (*i.e.*, at the glandular/adipose tissue interface).

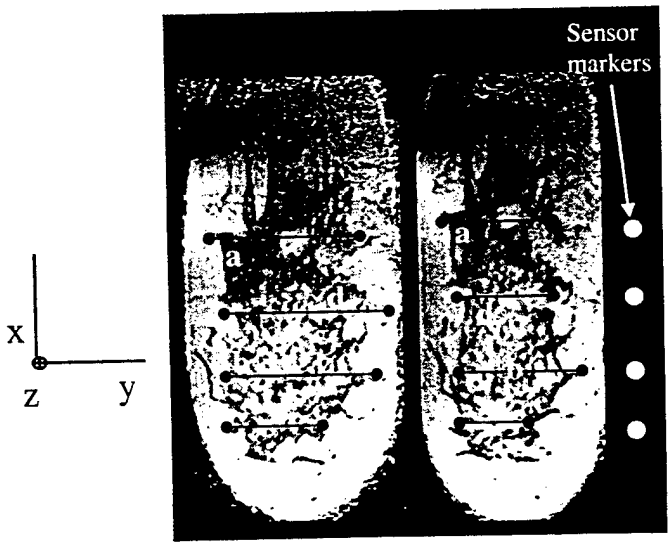

Figure 5.4 Coronal MR images showing some of the line segments used to calculate strain. Length of each line segment measured from tangential points along glandular tissue. The side diagram is the coordinate axes.

The tangential points were at positions along the breast in the S/I direction at which the resultant applied pressures were known. These pressure positions included the measured data points obtained directly from the sensors as well as the interpolated pressure points. Recall that fiducial markers, (*i.e.*, vitamin E capsules) were used to localize the sensors and segments beneath the sensors are lines a, b, c, and d in figure 5.4.

The lengths and angles of the line segments were measured and the line lengths separated into their *x, y* components. Lengths in the direction of the applied load (medial-lateral direction) were used to calculate the stretch ratio, λ_2 (λ is still called the stretch ratio eventhough the experimental data were compressive and not tensile, also the index 2 represents the principal axis in the direction of the applied uniaxial force, which in our experimental set-up is the *y* axis. The parameter, λ_2, was defined as the ratio of the *y*-component of a line segment in the deformed volume, to the *y*-component of the corresponding line segment in the undeformed volume. Line segments perpendicular (*i.e.*, superior-inferior) to the direction of the applied compression were used to calculate λ_1, which is the ratio of the *x*-component of the line segment in the deformed volume to the corresponding line segment in the undeformed volume. Using these stretch ratios, the axial (ε_y) and the in-plane transverse (ε_x) strains were calculated using the equations

$$\varepsilon_y = 1 - \lambda_2 \quad \text{and} \quad \varepsilon_x = 1 - \lambda_1 \qquad \textbf{5.2}$$

Only in the planes (*i.e.*, A/P position of the MR slices) where the sensor markers appeared, were the lengths of segments recorded. As shown in figure 5.5, the length, L_o, of a segment of tissue beneath a sensor was measured in the uncompressed state, and then the corresponding segment was measured in the deformed (compressed) state to give the deformed length, L. The stretch ratio was then evaluated using the ratio of L/L_o, and the axial strain calculated using equation 5.2. Each segment was measured three times and the average value was used.

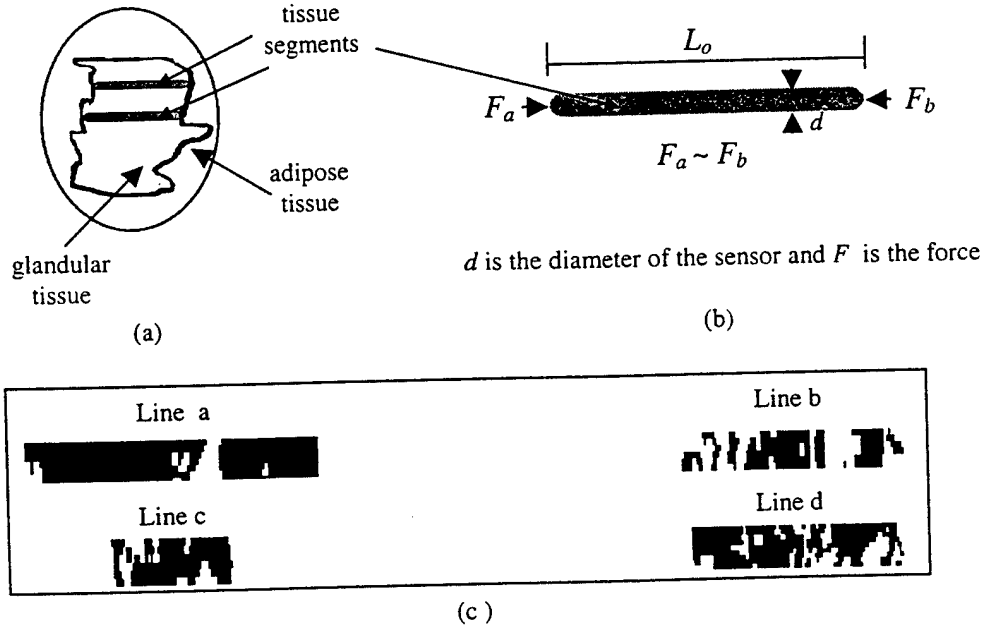

Figure 5.5 (a) Diagram of tissue segments used to evaluate strain. (b) Schematic of uniform force across segments. (c) Magnified images of uncompressed segments shown in figure 5.4. The white regions are adipose tissue and the dark regions are glandular tissue.

5.2 General Assumptions Used In Analysis

As shown in figure 5.5(b), the total force across each tissue segment is assumed equal to the load on the sensor. In order for this experimental force-deformation relationship to hold, several other assumptions must be made. The first is that the breast undergoes uniaxial compression with negligible friction at the plates. That is, the breast tissue is assumed to be a freestanding column that is not rigidly attached or confined. This is of course not true for breast tissue *in vivo* which is attached to the chest wall. However in order to begin modeling complex biological structures, and given the constraint of acquiring *in vivo* data, such simplifying assumptions must be made. They may perhaps be justified because the tissue in the regions of interest is far enough away from the chest wall. Also the anatomy of the breast is such that breast tissue is not rigidly attached to the chest wall or the pectoral muscle.

Furthermore, we assume the plates are sufficiently smooth such that friction is negligible. Also the layer of fatty tissue underneath the surrounding skin may lead to finite slipping at the plates. We tried to verify the assumption of negligible friction by compressing and imaging first without and then with a lubricant gel, which was placed on both the plates and the breast. However the data were inconclusive because the lubricant often interfered with the displacement markers (*i.e.*, the external markers adhered to the skin would fall off).

The second assumption is that there is a uniform distribution of force across each segment. This assumption was first tested by placing additional sensors on the bottom plate of the coil compression device using a breast phantom. Sensors were placed directly above and below the breast in only one *in vivo* breast study. That force distribution is given in table 5.1, with the force readings placed in parentheses. The similarity of the sensors readings above and below the breast indicates that the assumption is acceptable.

The last assumption is that the tissue is homogeneous. Recall from the anatomy of breast tissue, discussed in section 2.1, that breast tissue is not homogeneous. There is a mixture of various tissues in the breast. From mammograms, the breast appears like a honeycomb structure with pockets of fatty tissue and glandular tissue. The glandular tissue contains the branching lobular and ductal systems, and within these systems there is adipose tissue. The MR images shown in figure 5.4, used to evaluate stain for subject A, clearly show that there is some adipose tissue mixed in with the darker glandular tissue. Since this tissue cannot be separated *in vivo*, the tissue segment had to be modeled as homogenous. More complex analysis would allow separation of adipose and glandular tissue, however matching individual force measurements is not possible *in vivo*.

A scale was made to rate the tissue segments according to figure 5.5(c). In figure 5.5(c), images of the segments were enlarged and thresholded so that the adipose areas were set to a value of 1 and appear white, while the glandular areas were set to a value of

0 and appear black. If the segment was composed of at least 50% or greater of the darker glandular tissue, then the segment was modeled as glandular. Other segments were classified as adipose tissue. Segments classified as adipose were not used in the stress-strain analysis because adipose tissue has different mechanical properties than glandular tissue. The material properties of adipose tissue were investigated in a single study using subject C, but the results were inconclusive.

5.3 **Experimental Force-Deformation Data**

From the strain data given in table 5.2, positive strain values indicate that the undeformed length component is larger than the deformed length. That is, the components of the line segments in the deformed volume are contracted. Negative values indicate the opposite effect; that is, the line segments in the deformed volume are elongated. It is observed in breast tissue that at low compressions, some elongation of lines occurs along the direction of the applied force (M/L direction). Likewise, in the superior-inferior direction (shown in table 5.3), some contraction (*i.e.*, compression) of lines is observed. It is not known what causes this response, but such line segments are generally located in regions of the breast images where there is a greater content of adipose tissue, or at an adipose and glandular tissue boundary. One possible explanation may be the stretching and deformation of the net-like Cooper's ligaments [Cardenosa, 1995].

TABLE 5.2 Examples of Axial (medial-lateral) Strain								
Subject A Exam 3032			Subject B Exam 3033			Subject 3 Exam 8740		
segment label	% compression		segment label	% compression		segment label	% compression	
	9%	27%		15%	36%		14%	35%
1A*	15.9	29.5	2A*	33.3	36.0	3A*	12.2	34.2
1B*	15.4	38.5	2B*	12.5	37.5	3B	19.2	36.2
1C*	6.2	25.0	2C	16.3	24.8	3C	15.6	28.9
1D	-12.5	12.5	2D	20.8	31.5	3D*	8.7	32.6
1E	2.4	23.6	2E	4.9	19.1	3E	3.0	42.4
1F	-24.0	6.2				3F*	11.1	66.7

TABLE 5.2 Examples of Axial (medial-lateral) Strain
* Denotes measurements acquired with a corresponding force reading.

TABLE 5.3 Transverse (Superior-Inferior) Stain (Subject A Exam 3032)		
Line Label	% compression	
	9%	27%
1G	12.8	8.26
1H	-74.3	-39.9
1I	-18.9	-7.4
1J	16.4	10.9

TABLE 5.3 Transverse (Superior-Inferior) Stain (for Subject A Exam 3032)

Figure 5.6 shows bar graphs depicting the axial (medial-lateral) and transverse (superior-inferior) strains calculated for two compressions, moderate and high. The absolute values of strain are plotted in order to observe the general affinity of strain with compression. The overall trend for axial strain is that it increases as compression is

increased from a moderate compression to a higher compression, whereas the overall trend for the transverse strain is to decrease as compression varies from moderate to high. This decrease in transverse strain is likely due to the fact that the pectoral muscle limits transverse displacement. We observed a similar response in an initial assessment of 3D displacement of compressed tissue, (see section 4.7) [Williams et al., 1999].

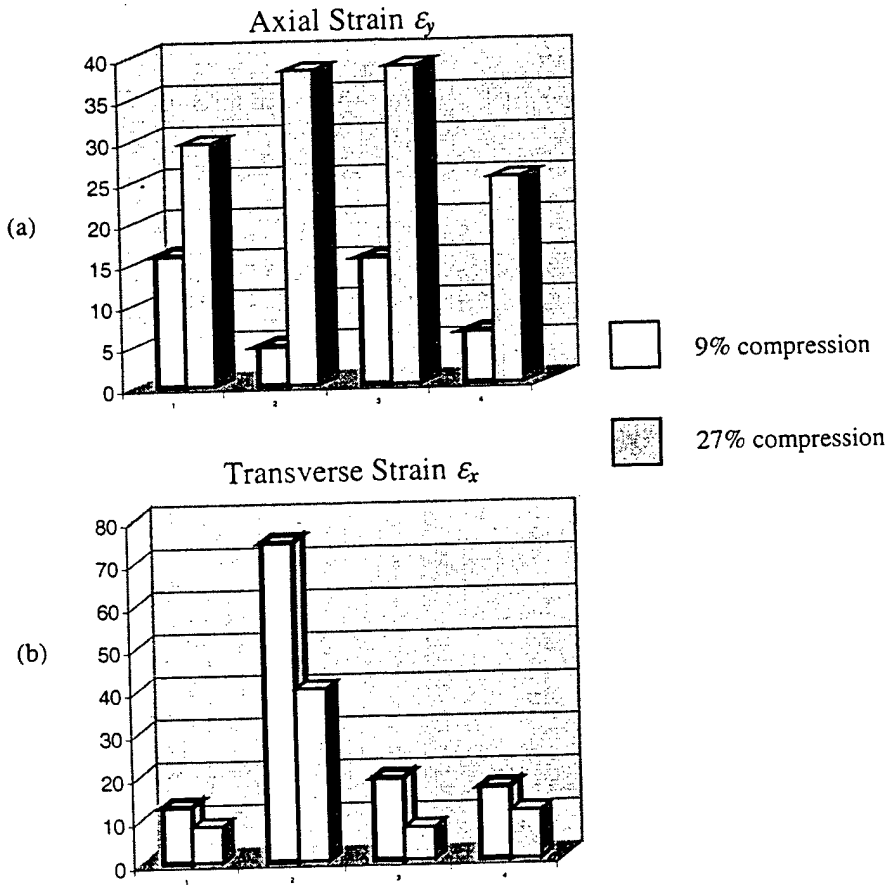

Figure 5.6 (a) Bar graph of axial strain for mild and moderate compressions. Axial strain increases as compression increases. (b) Bar graph of transverse strain for mild and moderate compression. Unlike the axial strain, transverse strain does not increase as the amount of compression increases.

5.3.1 Stress-Strain Relationship

The stress-strain relationship is obtained by fitting the stress (σ_y) and strain (ε_y) data using a least-square polynomial technique, where $\sigma = a + b\varepsilon + c\varepsilon^2$, and plotting the normal stress against the normal (axial) strain. As discussed earlier, stress and strain values evaluated directly from the readings and locations of the sensors represent data obtained manually, while the stress values obtained from the pressure distribution curve represent interpolated data. The stress and strain data are given in table 5.4.

TABLE 5.4 Axial Stress-Strain Data					
Subject A		Subject B		Subject C	
STRESS (KPA)	STRAIN	STRESS (KPA)	STRAIN	STRESS (KPA)	STRAIN
3.39	3.85	0.395*	3.03	1.97*	8.70
1.63	4.76	0.077	7.69	3.69*	12.2
0.345*	6.25	4.02	10.81	3.46	12.96
1.56	9.68	0.473	14.0	3.72	18.52
1.30*	15.38	0.483 *	16.0	3.99	19.23
1.57*	15.91	3.64*	21.21	3.88	21.28
2.68	22.22	0.267	23.81	4.03	24.53
1.68*	25.0	0.497	25.58	7.79	27.91
5.41	29.03	0.753	30.77	5.36	32.61
5.29*	29.55	0.119	31.58	8.35	33.33
1.63	29.73	4.28	32.0	8.36*	34.15
4.91	30.56	4.73	33.33	9.17*	36.17
4.35*	38.46	4.64*	36.0	8.84	38.30
5.56	43.24	4.85	39.5	9.29*	66.7

TABLE 5.4 Axial Stress-Strain Data
(* Denotes directly measured force data, all other values were interpolated as described in figure 5.3)

The stress-strain plots for both the manual and interpolated data, shown in figures 5.7, 5.8 and figure 5.9, were obtained for subjects for whom there was a significant variability in the amount of glandular breast tissue. The breast images are shown next to the stress-strain curves in figures 5.7 (c), 5.8 (c), and 5.9 (c). The curves do not go through zero, because of the initial stress due to body weight and gravity as the subject lies on her side with the breast resting on the bottom plate of the coil-compression device. From the pressure sensors placed on the bottom plate, this initial stress typically ranged from 0.619 to 1.0 kpa.

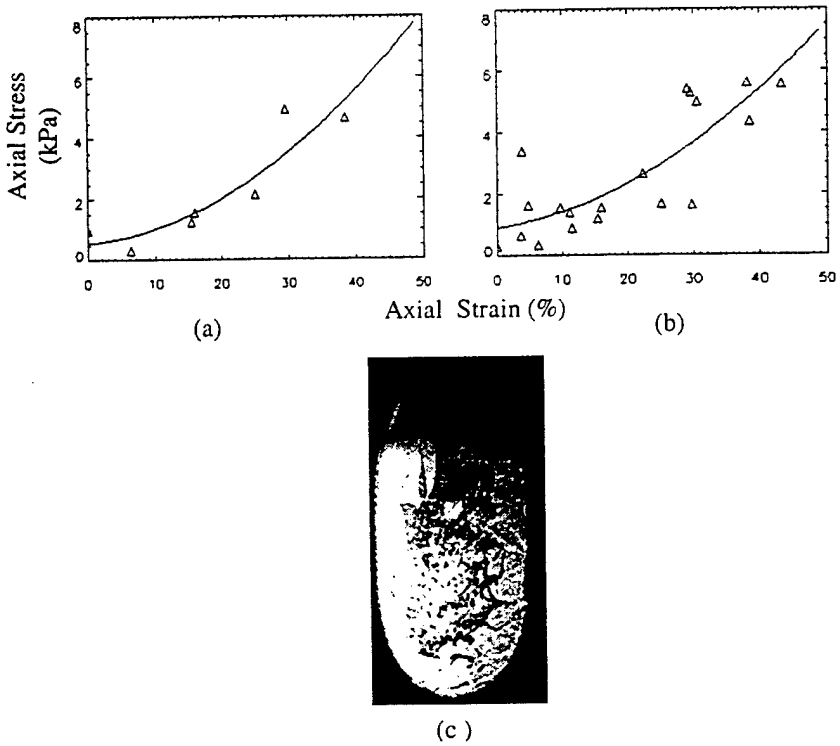

Figure 5.7 Stress-strain curves for uniaxial static compression for subject A. Data fitted using least squares method.(a) Stress data measured directly (manual). (b) Interpolated stress data. (c) Image of breast tissue. Δ - represent experimental data.

The standard deviation of the data fit of figure 5.7 (a) is 0.917 kPa, with a mean error estimate of ±0.581 kPa. With additional interpolated data, shown in figure 5.7(b), the standard deviation of the data fit is 1.18 kPa and the mean error is 0.456 kPa. Hence, the interpolated data obtained from the pressure distribution function provide an acceptable method to obtain additional data indirectly. As shown in the breast image, subject A has a mixture of glandular and adipose tissue, while subject B, shown in figure 5.8(c), has very little glandular tissue.

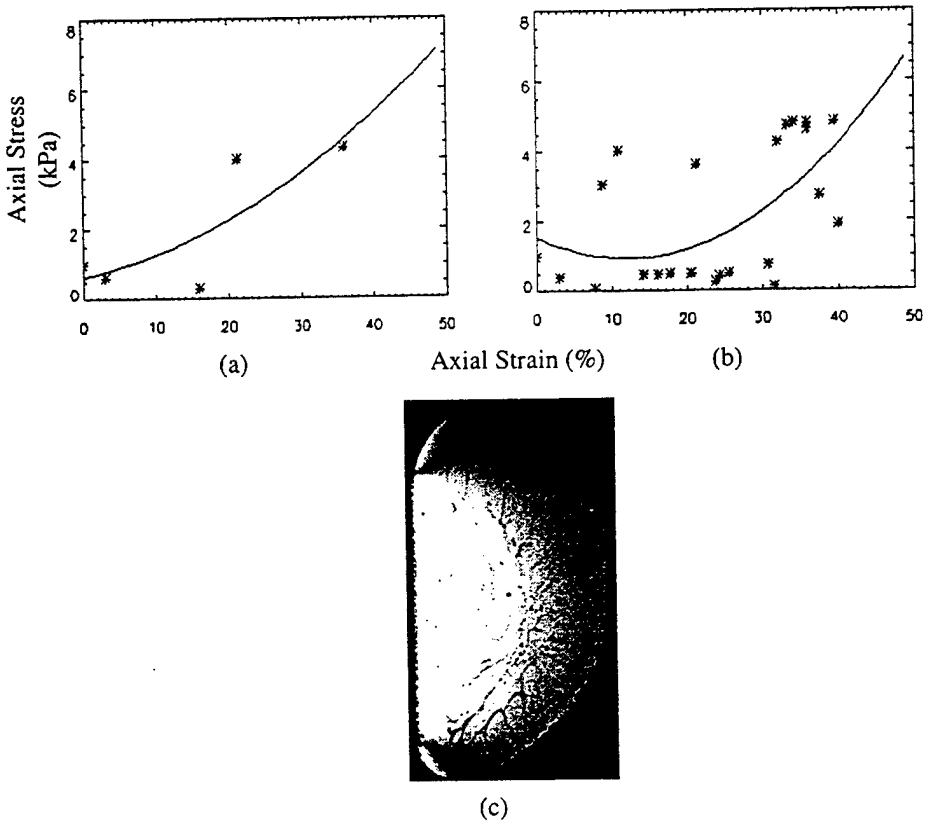

Figure 5.8 Stress-strain curves for uniaxial static compression for subject B.(a) Stress data for adipose tissue. (b) Interpolated stress data (automatic). (c) Image of breast tissue. * - represent experimental data.

Data on subject B were very limited to the fact that during the course of the study, two of the pressure sensors failed. Also, there was not insufficient amount of glandular tissue to measure strain. For these reasons, we decided to try to use subject B to obtain information about *in vivo* adipose tissue using the same techniques. The data in figure 5.8 is for adipose tissue only. The data fit of the stress-strain curves for figure 5.8 (a) and (b) are 1.604 kPa and 1.64 kPa with mean errors of 1.22 kPa and 0.558 kPa, respectively.

Subject C had denser breast tissue than both subjects A and B, and the stress-strain curves for the dense tissue are shown in figure 5.9

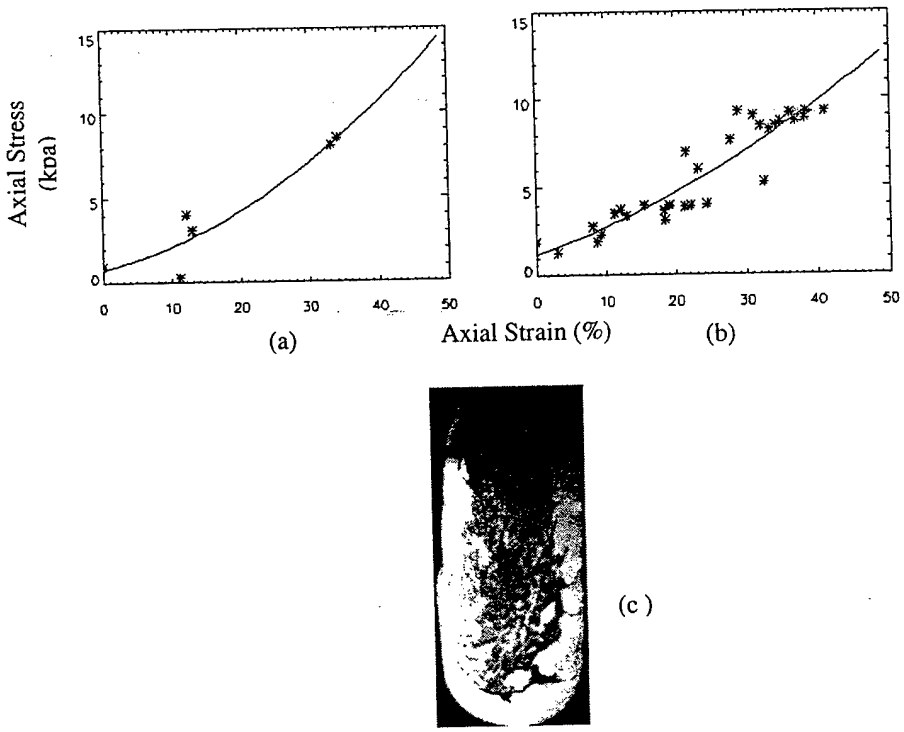

Figure 5.9 Stress-strain curves for subject C. (a) Manual data. (b) Interpolated stress data (automatic). (c) Image of breast tissue. *- represents experimental data.

The data fit has a standard deviation of 1.477 kPa and mean error of 1.020 kPa for the manual data in figure 5.9(a). With the interpolated data, the standard deviation and mean error of the data fit are 1.45 kPa and 0.402 kPa, respectively. There is less scatter in the data for subject C with an error estimate less than 0.5 kPa.

The stress-strain curves exhibit characteristics typical of soft tissue and represent, to our best knowledge, some of the first data in the literature of the *in vivo* stress-strain response of normal breast tissue. The curves are similar to other connective tissues that possess orientable collagen fiber networks, such as skin and aorta [Silver, 1987]. The strain at which the collagen fibers are fully straightened varies from tissue to tissue. As seen from the curves, breast tissue, like most connective soft tissue, exhibits low modulus at low strains, (<10%). It is not known what dominates this behavior, the aligning of collagen fibers, or the deformation of other components such as elastic fibers [Silver, 1987]. The adipose stress-strain curve has a longer low modulus region than glandular breast tissue. The stress of *in vivo* adipose tissue does not begin to increase until strains greater than 30 % are obtained. This prolonged low modulus region is likely due to the deformation of elastic fibers.

At higher strains, the modulus increases. For breast tissue, the increased stress response at higher strains in the medial-lateral direction is most likely due to the aligning of the collagen fiber network. At high strains when the collagen fibers are aligned, all

connective tissues behave similar to tendon [Silver, 1987]. Although little work in this area exists on breast tissue, it is well known in standard mammography that stronger forces are required for medial-lateral compression than for cranial-caudal [Watmough, et al., 1993, Sullivan et al., 1991]. This indicates that there is more resistance to deformation in the medial-lateral direction. Whether this response is due to the fact that such loading is along the collagen fiber axis, or simply the resistance of the pectoral muscle, is unknown.

5.4 **Theoretical Modeling**

There are many examples in the literature that model the nonlinear property of materials, as well as the compressibility. Four of these models are described in the Theory and Definitions section in chapter 3. Material parameters for breast tissue were estimated by fitting our experimental data to the Mooney-Rivlin, Ogden, Blatz and Vito SEDF models. The models are expressed in the following equations (for $N=1$):

$$\sigma_{y,\ \text{Mooney-Rivlin}} = 2C_{10}\left(\lambda - \frac{1}{\lambda^2}\right) + 2C_{01}\left(1 - \frac{1}{\lambda^3}\right) \qquad \textbf{5.3}$$

$$\sigma_{y,\text{Ogden}} = \frac{2A}{B}\left(\lambda^{B-1}\right) \quad \text{or} \quad \frac{2A}{B}\left(\lambda^{B-1} - \lambda^{\frac{-B}{2}-1}\right) \qquad \textbf{5.4}$$

$$\sigma_{y,Blatz} = \frac{\gamma}{\alpha+1}\left[\lambda\exp\left[\alpha\left(\lambda_1{}^2-1\right)\right]-\frac{1}{\lambda^2}\exp\left[\alpha\left(\frac{1}{\lambda}-1\right)\right]\right] \qquad \textbf{5.5}$$

and

$$\sigma_{y,Vito} = 2A\left(\lambda-\frac{1}{\lambda^2}\right)\left(B+\frac{C}{\lambda}\right)\exp\left[B(I_1-3)+C(I_2-3)\right] \qquad \textbf{5.6}$$

where λ is the stretch ratio in the direction of the applied compressive force.

Recall that the various coefficients of the SEDF models, which represent the material parameters, are different for each constitutive relationship. The coefficients were determined by a curve fit technique that uses a gradient-expansion algorithm to compute a nonlinear least squares fit to the SEDF function using statistical (Poisson) weighting, (*i.e.*, Weights $(i) = 1.0/Y_i$, where Y_i are the stress values). Fits were also performed with uniform weighting. In this IDL curve fitting routine, the partial derivatives with respect to the coefficients of the SEDF are supplied to the algorithm and iterations are performed until the chi square changes by a specified amount, or until a maximum number of iterations have been performed. The coefficients of the four constitutive expressions are shown in table 5.5.

TABLE 5.5 Material coefficients of SEDF models with the Standard Deviation			
	COEFFICIENTS ± STANDARD DEVIATION		
	SUBJECT A	SUBJECT B	SUBJECT C
Mooney-Rivlin	C_{10} = -2.91± 0.31 C_{01} = 1.05± 0.17	C_{10} = -0.61± 0.939 C_{01}= 0.203 ± 0.616	C_{10} = -5.75± 0.77 C_{01} =2.22± 0.514
Ogden (w/ λ_2,λ_3)	A = -1.54 ± 0.28 B = 1.85 ± 4.8	A = -0.229 ± 0.007 B = 3.48 ± 3.29	A = -3.98 ± 1.53 B =2.14 ± 13.5
Ogden (w/o λ_2,λ_3)	A = -1.99± 0.04 B = 1.31 ± 0.36	A =-1.83 ± 0.29 B =4.75 ± 3.71	A = -4.81 ± 0.31 B =2.04 ± 1.67
Vito	A = 2.97 ± 1.18 B = -0.86 ± 0.19 C = 0.178 ± 0.22	A = -0.645 ± 0.46 B = 2.26 ± 1.26 C = 0.912 ± 0.65	A = -13.0 ± 3.4 B = 0.465 ± 0.13 C = -0.19 ± 0.059
Blatz	γ =-1.79 ± 0.25 α = -0.74 ± 0.15	γ =-1.78 ± 0.27 α =0.607 ± 1.28	γ =-7.11 ± 1.00 α =-1.69 ± 0.31

TABLE 5.5 Material coefficients of SEDF models with the Standard Deviation

From the standard deviation values, the data from subject C can only fit the Mooney-Rivlin, Ogden and Blatz models, while the data from subject A can fit all of the models. However, the experimental data from subject A is more scattered than the data from subject C. For subject A, the Vito and Mooney-Rivlin models provide the best fits to the experimental data. Subject C had very dense breast tissue, with more glandular tissue than adipose. Subject A had more of a mixture of glandular and adipose tissue. Since the Vito SEDF was designed to model connective tissue, these data seem to indicate that exponential forms of the SEDF cannot model dense tissue very well.

Recall that the Ogden model can be expressed in two ways (see equation 5.4). The second expression in equation 5.4 involves λ_2, λ_3, where

$$\lambda_2 = \lambda_3 \sim 1/\sqrt{\lambda_1} \qquad 5.7$$

The Ogden SEDF was designed to provide good data fit to uniaxial test data, thus the model represents a suitable fit to various densities of glandular breast tissue, within the confines of the limited data and testing methods. Because the powers of B_i (λ^{Bi} in the Ogden SEDF equation) can be user-defined, the Ogden model is reported to provide a closer and more stable fit to test data.

The model that best fits adipose tissue is the Mooney-Rivlin model. The Mooney-Rivlin model is the simplest form of a polynomial SEDF where N=1. The expression in equation 5.3, is the compressible form of the classical Mooney-Rivlin law that has two finite elasticity constants [Fung,1972].

Figures 5.10, 5.11 and 5.12 show the results of the curve fitting of the SEDF models, where the least squares error for the fits ranges from 4.5 to 6.4 for subject A (mixture of adipose and glandular tissue); 6.3 to 22.5 for subject B (adipose tissue); and 0.905 to 1.265 for subject C (dense glandular tissue).

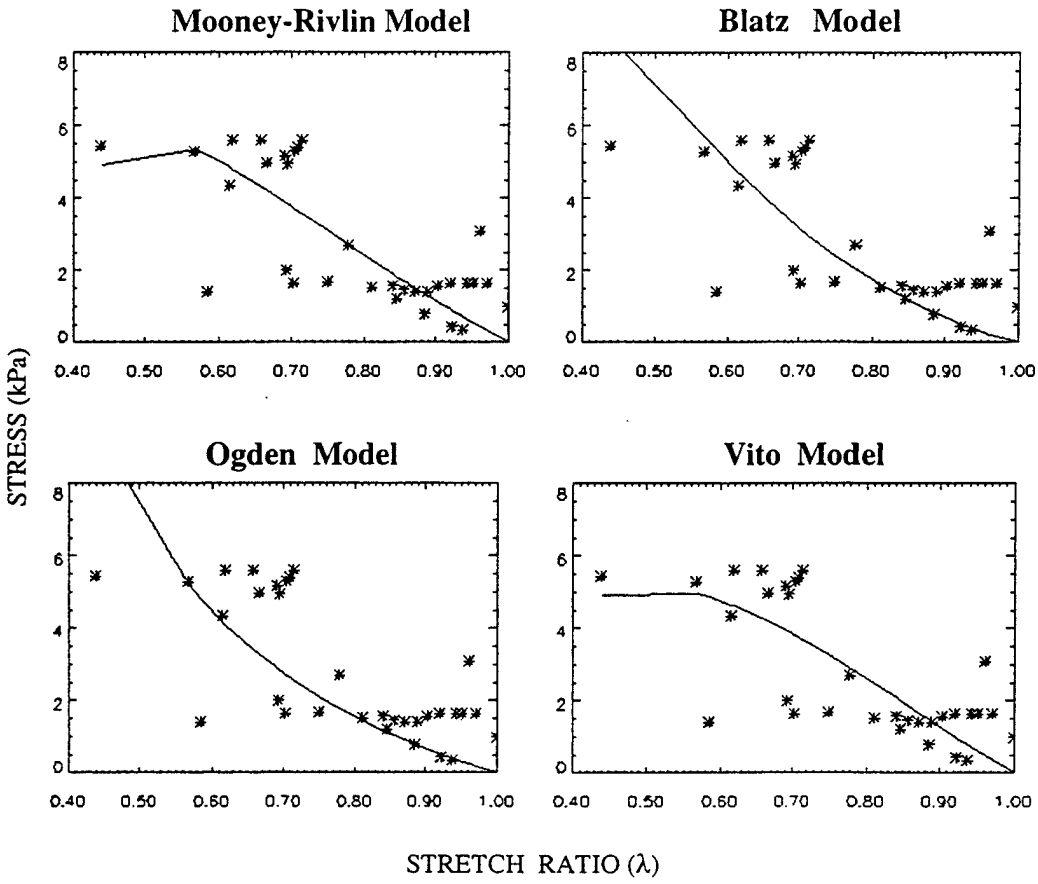

Figure 5.10 Modeling of breast tissue from figure 5.7(c) subject A using SEDF models.* represents experimental data, and ____ represents theoretical SEDF models

While the coefficients of the Mooney-Rivlin and Vito models have small standard deviations and represent good fits to the test data, as shown in figure 5.10, the models only fit the experimental data at low stress values ($\sigma_y < 3$ kPa). The theoretical models for adipose tissue are below shown in figure 5.11.

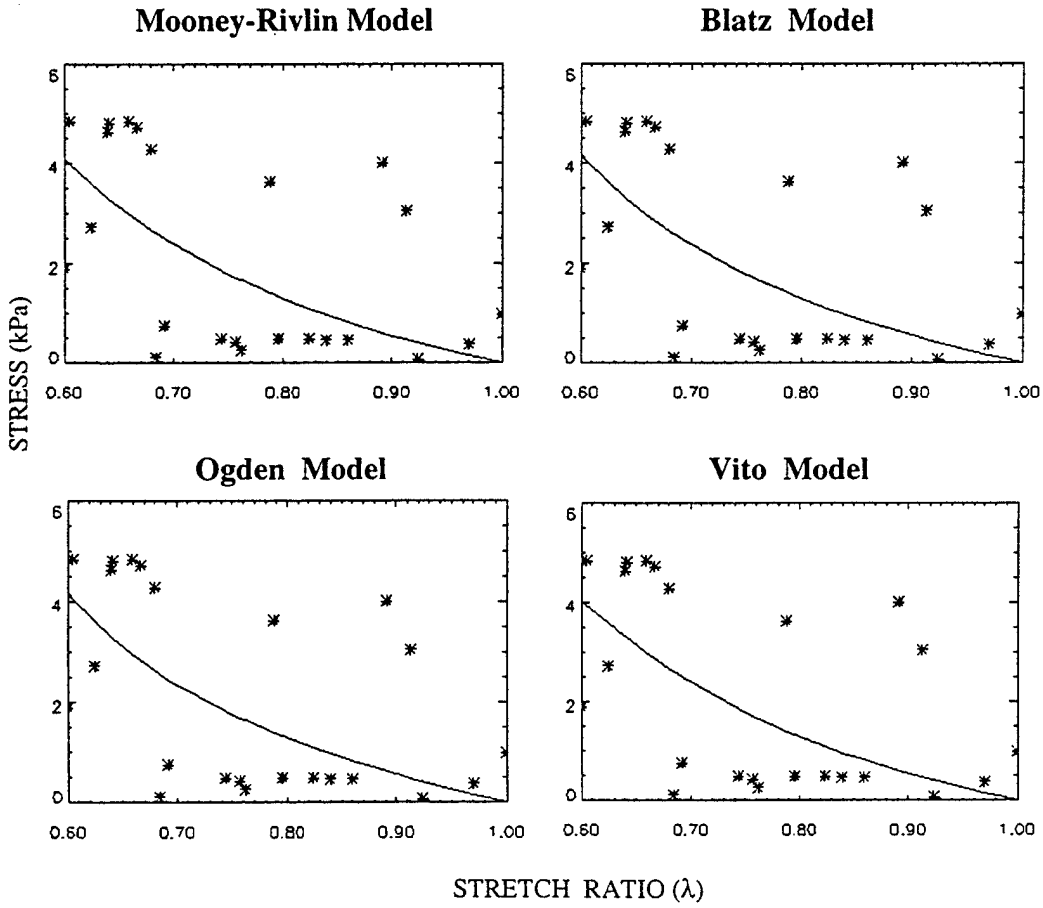

Figure 5.11 Modeling of breast tissue from figure 5.8(c) subject B using SEDF models.* represents experimental data, and ____ represents theoretical SEDF models

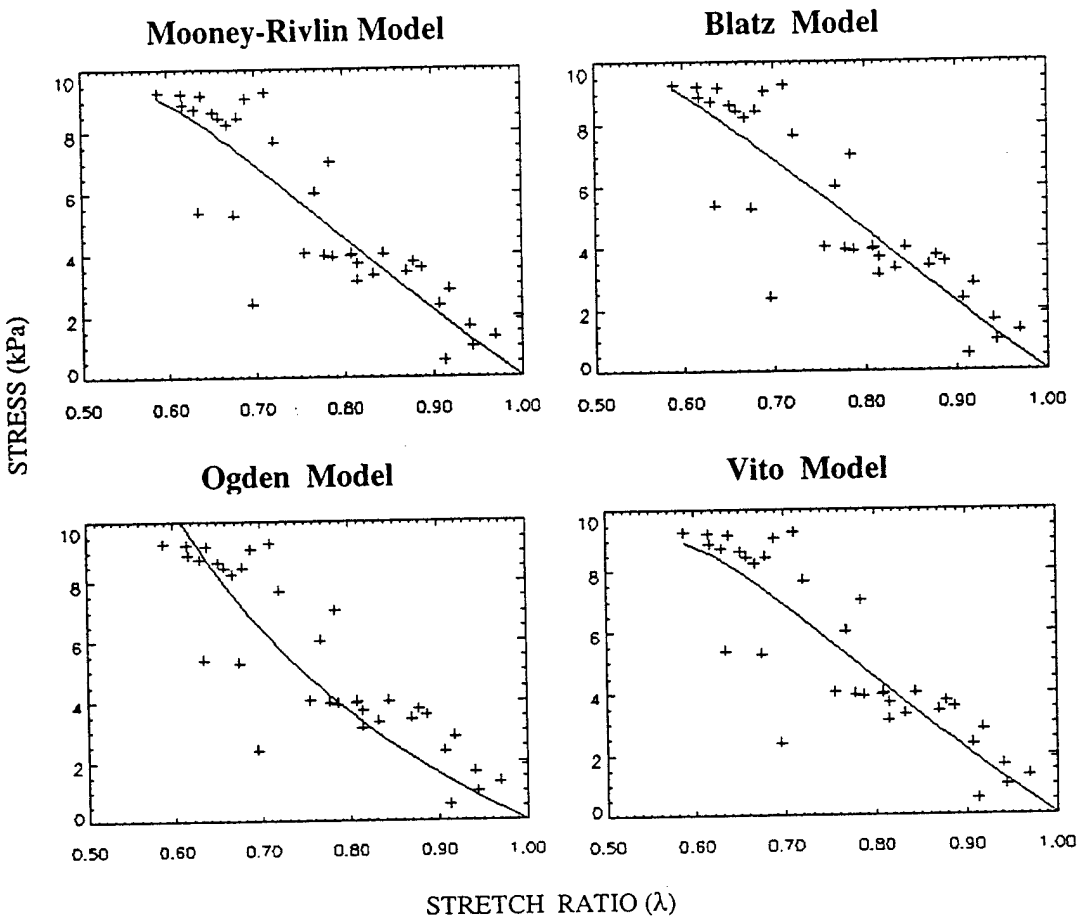

Figure 5.12 Modeling of breast tissue in figure 5.9(c) subject C using SEDF models. + represents experimental data, and ____ represents theoretical SEDF models

From figure 5.11, the Mooney-Rivlin, Blatz and Vito models aptly represent the static behavior at small stress values of adipose tissue undergoing uniaxial compression. For dense glandular tissue, the Blatz and Ogden curves both appear to fit the uniaxial test data, but the coefficients of the Ogden model have a better statistical fit. Further experimentation will be needed to better assess the usefulness and validity of a specific mechanical model. However, these data offer an encouraging first step on the way to obtaining mechanical modeling parameters.

This initial investigation into the force-deformation behavior of normal breast tissue provides some of the first *in vivo* data on breast tissue under loading conditions similar to those occurring in diagnostic examinations. We have demonstrated a viable method for obtaining *in vivo* deformation data suitable for studying the static mechanical properties of dense glandular breast tissue. Substantial tissue deformations are observed even under the mildest of compression. In conventional mammography, the medial-lateral breast compressive force over the entire breast and compressive breast thickness can range from 70 N -140 N and 60 mm - 30 mm, respectively [Sullivan *et al*, 1991]. In this study, the maximum compression force was 39 N (total area of the plate) and 1 N per sensing area, with a maximum breast thickness of 60 mm. Our data indicate that under static compressive loading, glandular breast tissue exhibits features similar to other

connective soft tissues, such as skin and aorta, and by using the strain energy density functions (SEDF) the static, uniaxial, compression behavior of *in vivo* breast tissue can be appropriately modeled.

CHAPTER 6

COMPUTER SIMULATIONS OF DEFORMATION

A major constraint of modeling of soft tissue is that the model should correctly represent the deformability of real tissue undergoing pressures similar to those occurring in real-life applications. Image morphing is useful in displaying deformation because the displacements can be smooth from one position to another. Image morphing is useful in displaying deformation because the displacements can be smooth from one position to another. Control points such as those used in finite element models may be warped and morphed. Points and lines guide the morphing process, and when the control points are warped, deformation of the material is generated. While existing computer algorithms can efficiently simulate deformation for image morphing, they largely ignore the physical principles of deformation. These computer algorithms use geometric primitives such as triangles to compute deformations.

A simple morphing algorithm commonly used is free form deformation (FFD) in which point features are organized on a rectilinear mesh. In FFD, displacement is

associated with a deformation parallelepiped box. The points of the face of the box are expressed in the coordinate system of the box. The positions of the points are updated when the coordinates of the box are displaced.

Another morphing algorithm, known as feature-based morphing, uses both points and lines as features. The defined control points and lines drive the displacements by using such factors as the distance to the nearest line segment and the length of the nearest line segment. As the number of control points increases, the generated morph becomes more accurate.

A major problem of image morphing is foldover. If many-to-one correspondences occur between the source and the target at some point during a morph, then the resulting morph contains undesirable wrinkles or distortions in the images. When feature movements are small, most existing morphing algorithms can produce one-to-one mapping. However for large displacements, foldover can occur. Foldover is defined as the overlapping of control points that induces distortions and undesirable wrinkles into the resulting images. The foldover-free technique constructs a triangulation over a given set of features. As the features move, the triangulation changes its structure and no edges in the triangulation may cross line features [Fujimura, 1997].

6.1 **Initial 2D Morphing Study**

We began our study by investigating two-dimensional image processing because of the abundance of literature and availability of techniques in 2D morphing. Computer morphing techniques such as free form deformation (FFD) and feature-based morphing were used to simulate 2D deformation of breast tissue. The morphing algorithms mapped landmarks from the source image to the target image, and control points were chosen according to the internal and external landmark studies discussed chapter four.

In a preliminary study, a 2D feature based computer morphing algorithm was employed to map internal anatomical landmarks from prone breast images obtained with a commercial breast coil (the source image) to supine breast images obtained with a body coil (the target image). As shown in figure 6.1, the prone breast images have higher resolution than the supine images. Also, because supine images were acquired with the body coil, the images were noisy, due to cardiac and respiratory motion.

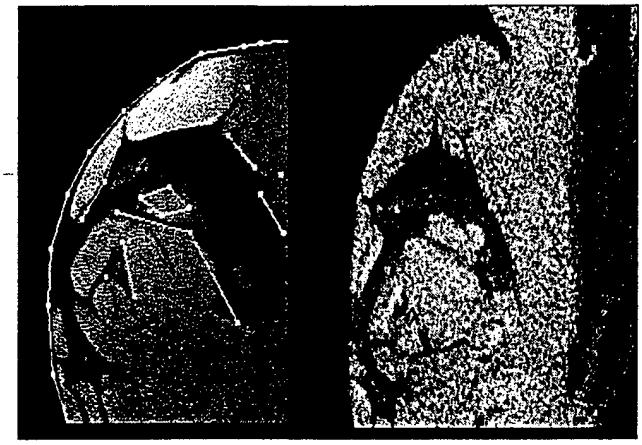

(a) (b)

Figure 6.1 (a) Prone (source) image with control points and lines.
(b) Supine (target) image

Image control features that guide the morphing process are shown in figure 6.1(a). The point and line features in figure 6.1(a) are drawn at locations classified as type II (tips of extrusions and valleys of vaginations) and type III landmarks (tangential points).

The morph, generated with the algorithm, is shown in figure 6.2. The morph was generated within three to four minutes and the image is less noisy than the original supine image, however some areas of the generated supine image are not correctly morphed using the feature based algorithm.

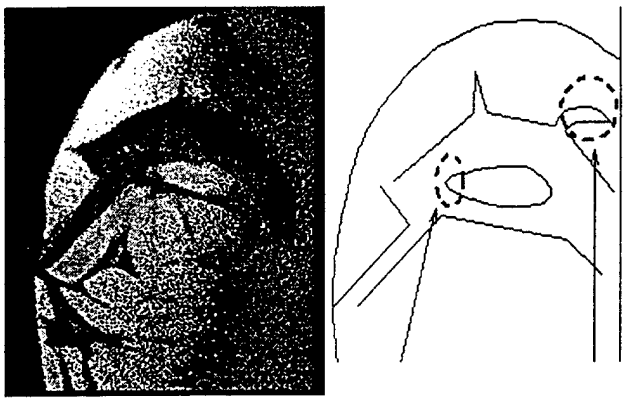

(a) (b)

Figure 6.2 (a) Morphed image resulting from feature-based morphing algorithm. (b) Incorrectly morphed areas.

To generate a better morph, a 2D foldover-free computer algorithm was employed. This morphing algorithm can be found in the reference, Fujimura, 1997. The morph generated with the algorithm is shown in figure 6.3. The 2D foldover-free algorithm provides a better one-to-one mapping and generated a better image.

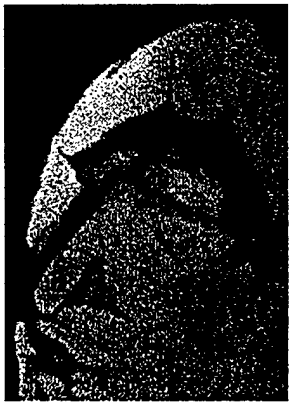

Figure 6.3 Morph generated with foldover-free algorithm

Noting that prone to supine imaging of the breast exhibited very large deformations while providing little mechanical information, we decided to use smaller controlled finite deformations of the breast to better evaluate the mechanical properties of breast tissue. By applying static compression forces in small incremental steps using the coil-compression device, small finite deformations are obtained. The compressed and uncompressed images are shown in figure 6.4. A 2D feature based morphing algorithm was employed on these images with image features controlling the morphing process. For the morphing process, the uncompressed image is the source image (*i.e.*, the beginning of the morphing process) and the compressed image is the target image (*i.e.*, the end of the morphing process.

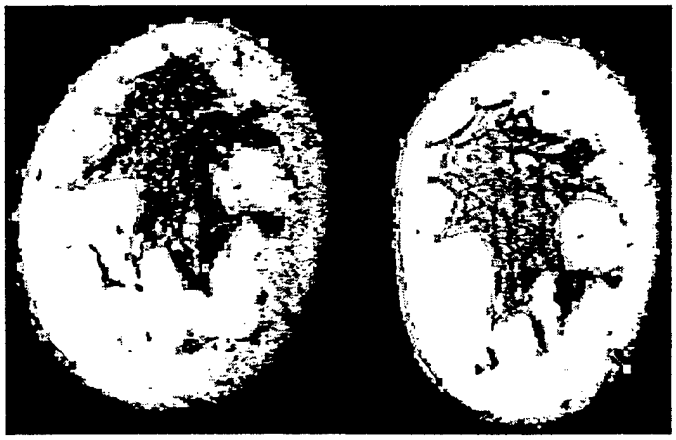

(a) (b)

Figure 6.4 (a) Source (uncompressed) image with identifying feature control points and lines. (b) Target (compressed) image

The generated morphs are shown in figure 6.5. Some areas of the target image are not correctly morphed. As more control points are defined, a better image is generated and the correlation between the morph and target improves.

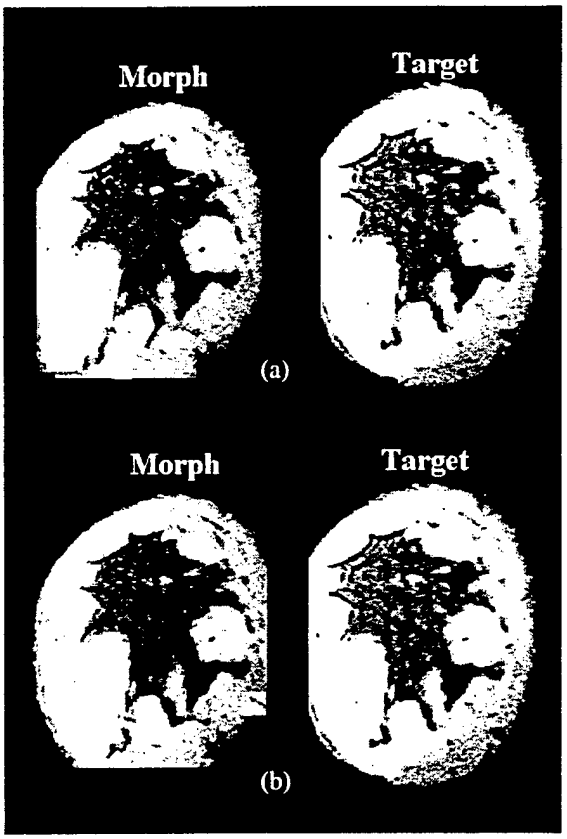

Figure 6.5 Morph images resulting from feature based algorithm generated with (a) 20 Control Points, (b) 42 Control Points.

When feature movement or shape deformation is small, most morphing algorithms can produce a one-to-one mapping between source and target. For large

deformations, however, overlapping between control points can occur. The foldover-free algorithm can provide better one-to-one mapping, eliminate overlap, and generate a better image.

6.2 **3D Morphing**

Although volume (3D) based morphing techniques are not as widely available as 2D morphing, they are more suitable for 3D data because 2D morphing cannot display out of plane deformations. Our initial data indicate that tissue deformation occurs in three dimensions (see section 4.4.2 on the 3D displacement vectors of selected landmarks; the volume is shown in figure 4.15).

As can be seen from the volume images, identifying appropriate 3D landmark features from the segmented data to drive the morphing algorithm is a challenge. To perform 3D morphing, appropriate features that could be mapped to the target image are required. Type II landmarks (*i.e.*, extrusion peaks) are favored because they are easier to identify. Slice by slice 2D morphing of the volume data can be easily accomplished, but 3D morphing is more problematic. A mesh free form deformation (MFFD) algorithm was investigated for preliminary 3D studies, but yielded unsatisfactory results. In an MFFD algorithm, the object is not deformed directly, but it is embedded in a space that is

deformed. The effects of deforming that space are then propagated to the object. We found that the algorithm only worked for symmetrically shaped objects, such as spheres or cubes.

As stated earlier, the 2D morphing techniques such as free form deformation (FFD) and feature-based morphing are abundant and widely used in image morphing. However, such morphing algorithms can only accurately simulate very small deformations. For larger deformations, foldover can occur. In addition, while existing 2D morphing algorithms efficiently simulate small deformation, they ignore physical principles of deformation and therefore are difficult to incorporate into real-life and real-time applications. One way of overcoming the limitations of morphing algorithms is by employing finite element models.

6.3 **Finite Element Modeling**

Finite element models are the most widely employed deformable tissue models used because they can model a continuum. The finite element method describes a volume or surface as a set of basic elements, such as tetrahedra, triangles, and other polygons. Splines can be seen as finite elements with a definite shape function. Spline interpolation represents a type of mesh deformation model whereby application of moving groups of control points generates deformation.

Finite element models are capable of simulating a wide variety of materials, real-situation loadings (*e.g.*, static or dynamic), and boundary conditions. With FEM, material properties can be incorporated into the model by using experimental deformation data. FEM describes a volume or surface as a set of basic elements. The volume of an object is divided into subregions of finite elements, and each element possesses the material properties of the object.

6.3.1 Finite Element Analysis

Abaqus [Hibbitt, Karlsson & Sorenson, Inc. Pawtucket, RI.] FE software was employed for our deformation simulations because of its capability to simulate a wide variety of material properties The finite element model was designed to represent the large deformation of breast tissue undergoing static compressive loading. The material parameters of *in vivo* breast tissue were derived from uniaxial test data, which were obtained by using MR measurements of deformation. To verify the capabilities of Abaqus as well as simulate the procedure of compressing the breast between two plates, a simple nonlinear, large deformation FE model was developed using static loads and prescribed initial and boundary conditions.

The static compression procedure was modeled using two approaches: one with the skin, glandular and adipose tissues, and the other with the glandular tissue standing

alone. The skin was modeled with membrane elements. Membrane elements are generally used to represent thin surfaces of sheets in space (*e.g.*, the thin rubber sheet that forms a balloon). Such elements offer strength in the plane of the element but have no bending stiffness or transverse shear stiffness. The only nonzero stress components are those parallel to the middle surface of the membrane.

The element mesh, shown in figure 6.6, was modeled with 75, eight-node membrane elements. Inside the skin membrane mesh, another mesh was generated using 1225, eight-node hexahedral continuum (solid) elements to represent breast tissue, with the glandular tissue attached to the skin at the areola, (*i.e.*, nodal contact interaction between the nodes of the membrane and solid elements at the front of the two meshes). In the FE model, the glandular tissue was surrounded by fatty (adipose) tissue that was given a different material stiffness.

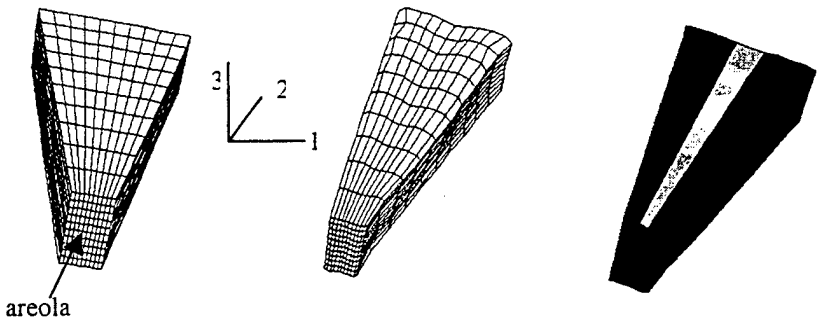

Figure 6.6 (a) Simple mesh of wedge of breast tissue using membrane and solid elements to model the skin and breast (glandular and adipose) tissue, respectively. (b) Deformed model (c) Contour model showing the glandular tissue in the center of the model

In Abaqus, solid or continuum elements are used for complex nonlinear stress and finite strain analysis involving large deformations. In general, such well-shaped elements should be used in critical regions of the mesh where the analysis is done. While tetrahedron, triangular, and wedge elements can be used to model complex shaped volumes, they are usually avoided because they tend to introduce numerical singularities in FE analysis [Mendis, 1995].

To model some of the mechanical contact between the different types of materials (*i.e.*, skin, adipose and glandular tissue) surface contact interactions were defined. The model was designed so that the nodes of the skin mesh and tissue mesh were matched. As

stated before, the front nodes of the skin mesh were in direct contact with the nodes of the glandular tissue to model the region of the areola. This allowed a simulation of contact between the two deformable bodies. For the skin and tissue interface and gland and adipose interface, contact surfaces were defined and given the property of finite sliding. Since adipose tissue has less material stiffness than the skin or glandular tissue, it was used as the slave surface. In Abaqus, the nodes of the slave surface are constrained so as to not penetrate into the master surface, but the nodes of the master surface can penetrate into the slave surface.

Finite sliding permitted the arbitrary motion of the contact surfaces, however it was computationally expensive and we observed no discernable difference in the FE analysis between modeling with and without glandular/adipose interface surfaces.

To simulate the compression plates, boundary conditions were applied so that the lateral nodes of the mesh were constrained in the direction of compression and a body force of 1.6 to 3 kPa was applied to the left (lateral) side of the mesh, where the breast rests on the bottom plate. A distributed force representing the uniaxial compressive force was applied to the right (medial) side of the mesh. The body force was estimated from a single sensor placed on the bottom compression plate and by using the breast mass and lateral area of the breast in contact with the plate. These bottom sensor measurements ranged from 1.8 kPa to 2.7 kPa. The lateral breast area, measured on the MR images,

ranged from 5000 mm^2 to 6000 mm^2. The weight of the breast resting on the plate was about 8.1 N; therefore the minimum lateral load (or body force) was about 1.6 kPa.

Friction and finite slip were neglected at the surfaces of the top and bottom plates because fiducial markers indicate that this movement is negligible. However, to more accurately simulate mammography loading, finite slip could be added to the Abaqus model. To simulate finite slip boundaries, the nodes on the right and left sides of the mesh were constrained in the x and z directions of the global coordinate system (shown as 1 and 3, respectively, in Figure 6.6). The back nodes of the membrane or skin mesh were constrained in the x, y, and z directions to simulate the attachment of the skin to the chest wall. Also, an initial stress was placed on the membrane elements in the x degree of freedom, since the elements tended to buckle under compressive loading.

To model the material properties in the simple FE model, the modulus of glandular tissue was set in the range of 100 to 250 kPa, [taken from reference Azar, 1998]. The modulus of skin was set in the range 300 –500 kPa [Azar, 1998, Fung, 1972], and the modulus of adipose tissue was placed as least ten times less than glandular tissue. All tissue types were modeled as incompressible with Poisson's ratios of 0.43 to 0.45. This simple model provided a good representation of the approach to simulate the compression of breast tissue.

With Abaqus, unique modeling of material properties could be achieved, however the software is limited in generating complex geometrical mesh shapes that are required for displaying the out-of-plane branching of breast tissue. To build a more complex breast model, several methods were investigated to import the geometry data of breast tissue directly into the FE processor. Geometry files such as IGES (initial graphics exchange specification), STL (stereo lithography), and DXF (AutoCAD) were created since Abaqus had some limited preprocessing and automatic meshing capabilities. However the input data files were too large and complex for Abaqus to handle. To translate the geometry of the breast tissue into a format readable by Abaqus, a coordinate file was generated by obtaining the coordinates of points along the edges of segmented glandular tissue for each MR slice. The model was made by stacking up the slices in the z (*i.e.*, anterior-posterior) direction. The high complexity of the tissue model was reduced by decreasing the resolution of the MR data. The model consisted of 15 slices with an in-plane resolution of 0.8 x 0.8 cm and an out-of-plane (A/P) resolution of 3.5mm. The model, shown in figure 6.7, contained 1011, eight-node solid elements and 1361 nodes.

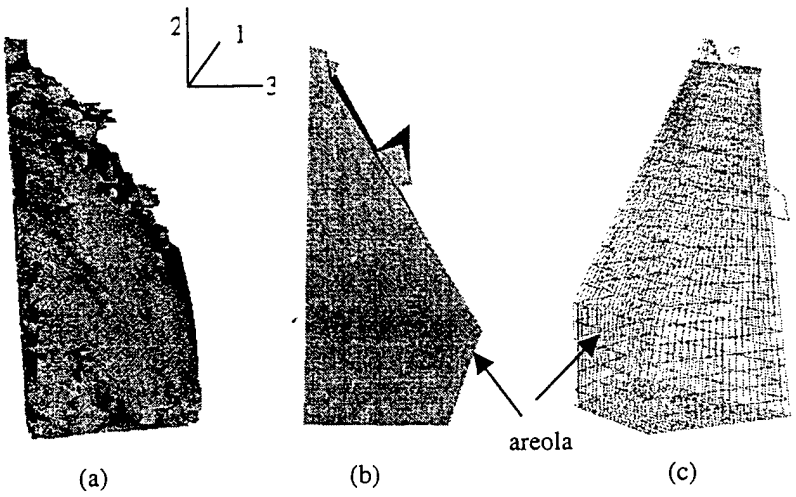

Figure 6.7 (a) Volume of segmented tissue (lateral view). (b) Corresponding reduced resolution FE model. The center extrusion was enhanced in the model. (c) Front view of FE model. 1 – M/L, 2 – S/I, 3 – A/P directions

As can be shown in the model, only extrusions could be readily differentiated because of the low resolution. The most visible extrusions were located at the top and on the medial side of the model. A smaller extrusion was observed on the front of the model and adjusting the z coordinate enhanced it. Each extrusion was represented by only one volume element, in order to analyze their displacement.

In the simple model, the various tissue parameters used were taken from the literature and did not involve *in vivo* breast tissue data. To model the large deformation of *in vivo* breast tissue, uniaxial test data were acquired (as outlined in chapter 5) and used as material parameters to ascertain a constitutive relationship for FE modeling of breast tissue. The constitutive models investigated were all based on the strain energy density function (SEDF) and incorporated the mechanical properties of soft tissue.

Soft tissue is defined as a nonlinear, incompressible, viscoelastic material, and the SEDF models listed in chapter 5 incorporate all of the material properties except viscoelasticty. That is, the SEDF models are not functions of strain rate. This limitation of the SEDF models is overcome somewhat by modeling soft tissue as a hyperelastic material. Materials that undergo large elastic deformations under static loading conditions can be characterized as hyperelastic. Such a method has been used to model brain tissue under large deformations [Mendis, 1995].

Abaqus offers two forms of a strain energy density functions to model hyperelastic materials. They are the polynomial SEDF and the Ogden SEDF. For N=1, the polynomial SEDF reduces to the Mooney-Rivlin SEDF. Figures 6.8 to 6.10 show the comparisons between the nominal stress-strain relationship predicted by the hyperelastic finite element model and the experimental compression data.

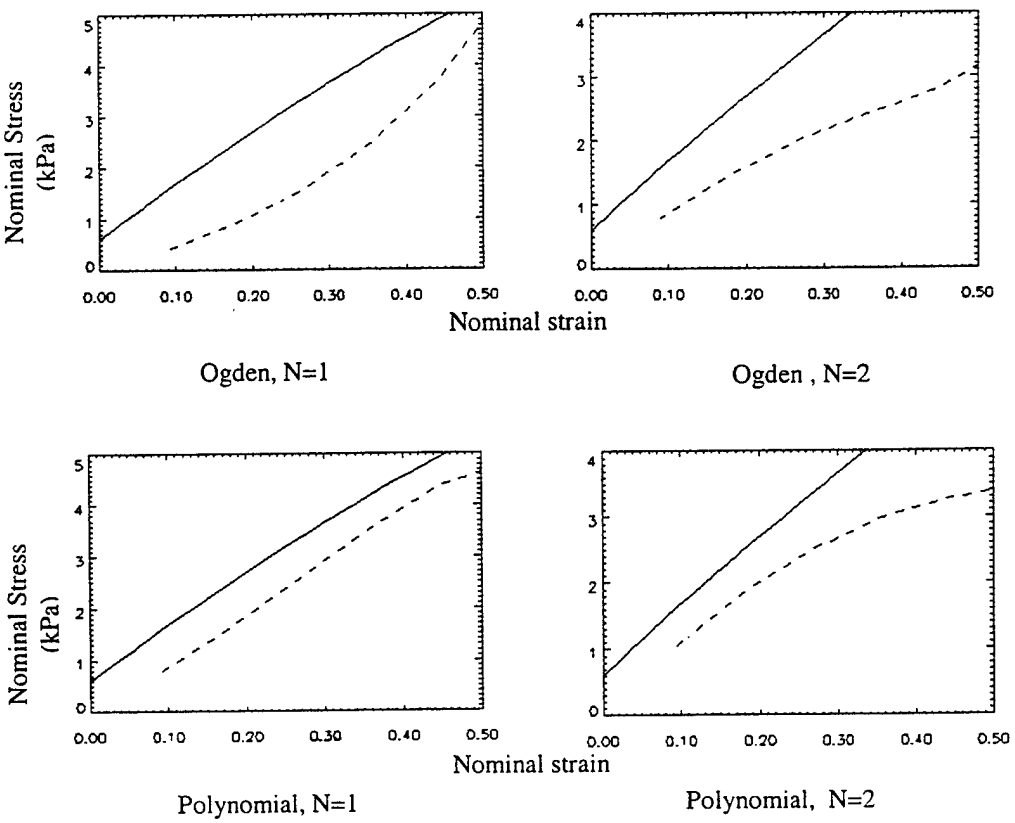

Figure 6.8 Comparison of uniaxial stress-strain results using experimental data (solid line) and the Abaqus finite element model (dashed line). Exam 3032 Subject A

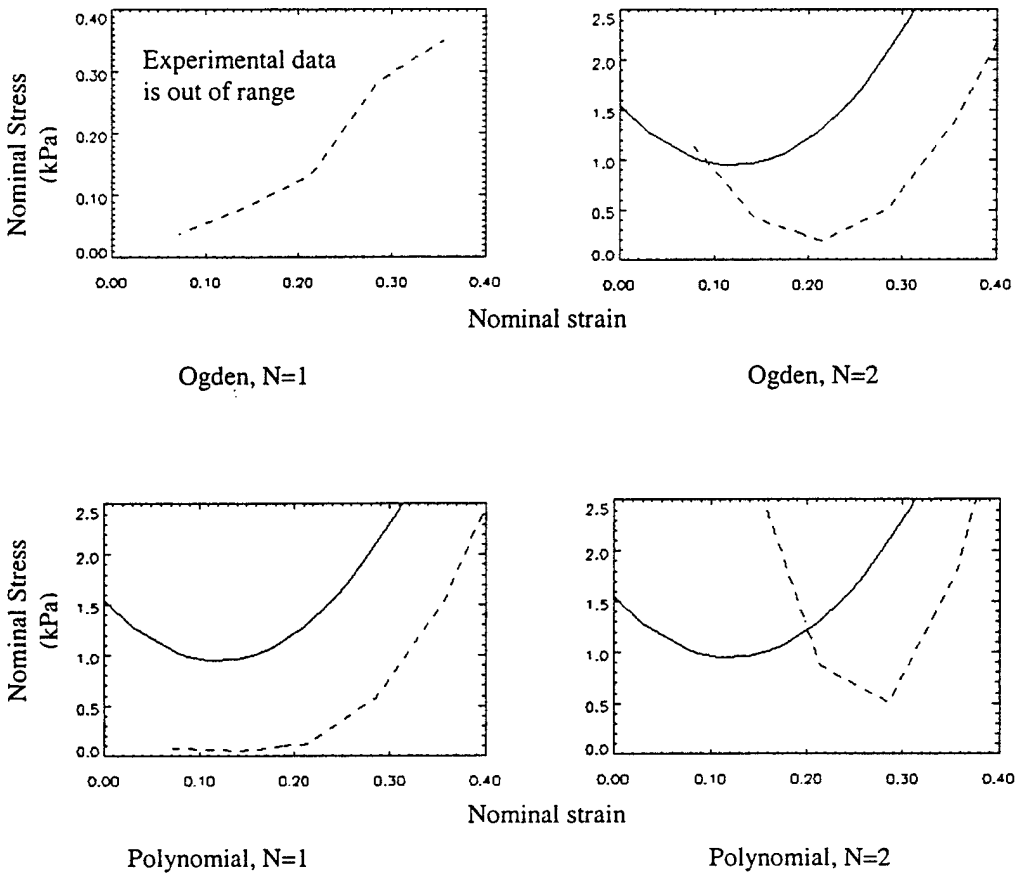

Figure 6.9 Comparison of uniaxial stress-strain results using experimental data (solid line) and the Abaqus finite element model (dashed line). Exam 3033 Subject B

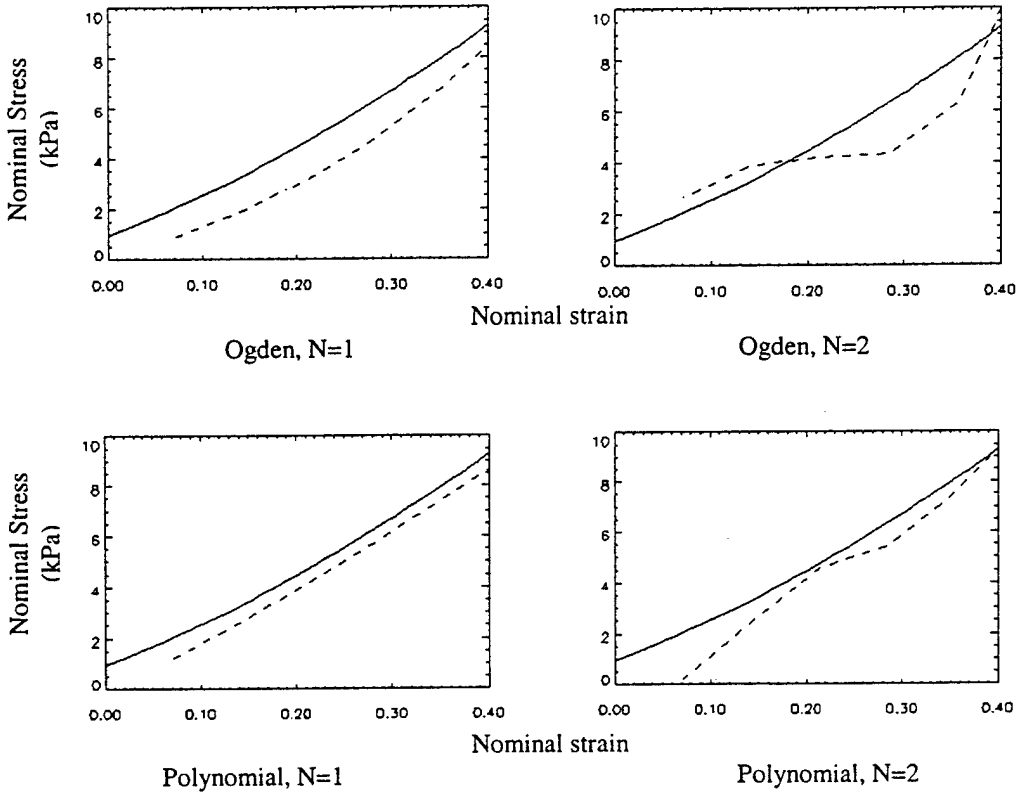

Figure 6.10 Comparison of uniaxial stress-strain results using experimental data (solid line) and the Abaqus finite element model (dashed line). Exam 38740 Subject C

These curves indicate that the Mooney-Rivlin strain energy density function provides the best constitutive relationship for FE modeling of breast tissue, especially for dense breast tissue (figure 6.10). This is in good agreement with the stress predicted by

the theoretical SEDF models in chapter 5 (see table 5.5). However, neither SEDF provides a good fit to the adipose data. The adipose tissue analysis is really inconclusive because the deformation data is not very reliable. The experimental adipose data does not even fall in the same range as the Mooney-Rivlin FE model. Recall for this data set, both the stress and stretch ratio measurements were limited.

Abaqus fits the stress-strain data by a least squares method that minimizes the relative error in stress using the following equation

$$E = \sum_{i=1}^{n} \left(1 - \sigma_i^{th} / \sigma_i^{test} \right)^2 \qquad \textbf{6.1}$$

where n is the number of stress-strain pairs in the test data, σ^{test} is the stress value from the test data, and σ^{th} is the theoretical stress evaluated from the SEDF relation.

Although the Mooney-Rivlin model provides a better fit than the Ogden model, the hyperelastic polynomial model becomes unstable when the nominal strain in uniaxial compression becomes less than 0.41. In order for stability to hold, the following criteria must be met:

$$d\boldsymbol{\sigma}:d\varepsilon>0$$

$$d\varepsilon\cdot\mathbf{D}:d\varepsilon>0 \qquad \textbf{6.2}$$

where $d\sigma$ is the change in stress due to an infinitesimal change in strain, $d\varepsilon$, and $\boldsymbol{D}$ is the tangential material stiffness. For the material stability to be satisfied, $\boldsymbol{D}$ must be positive definite. For the polynomial SEDF, in terms of the principal stresses and strains, the stability relation in equation 6.2 reduces to

$$d\sigma_1 d\varepsilon_1 + d\sigma_2 d\varepsilon_2 > 0 \qquad \textbf{6.3}$$

such that for the material stability criterion that D be positive definite, it is necessary that

$$D_{11} + D_{22} > 0$$

$$D_{11}D_{22} - D_{12}D_{21} > 0 \qquad \textbf{6.4}$$

The accuracy and stability of the FE model could be improved by using additional deformation modes, such as biaxial test data. The polynomial and Ogden models in Abaqus perform best when several deformation test data are used. However, our experimental approach could only yield uniaxial test data.

Using the Mooney-Rivlin constitutive relationship to model breast tissue and applying the initial and boundary conditions outlined earlier, the FE analysis yielded the deformation shown in figure 6.11.

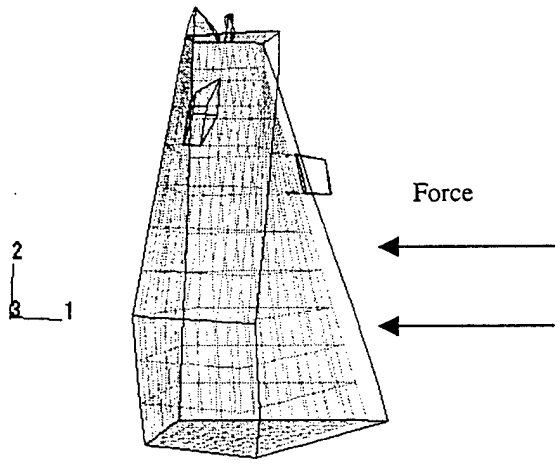

Figure 6.11 Deformation resulting from uniaxial compression. Undeformed model is superimposed on the deformed model. The heavy dark lines represent the undeformed model.

As can be seen, there is more deformation at the top of the model than at the bottom (*i.e.*, the superior-inferior direction). This is in agreement with the observation that the pressure decreases along the S/I direction. Also the prediction that the deformation is larger along the back (posterior) of the model than in the front (anterior) is consistent with medial-lateral compression of the breast. The displacements of the extrusions are given in figures 6.12 to 6.14.

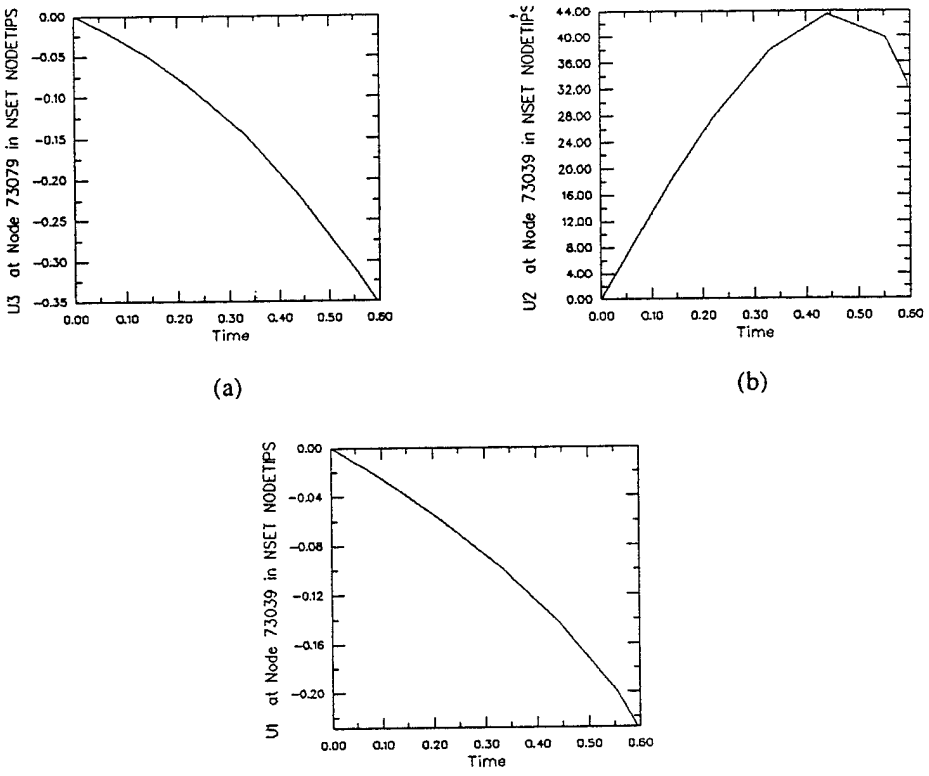

Figure 6.12 Displacement of superior extrusion at the specified fixed time increments in the simulation. (a) U3, (b) U2, and (c) U1.

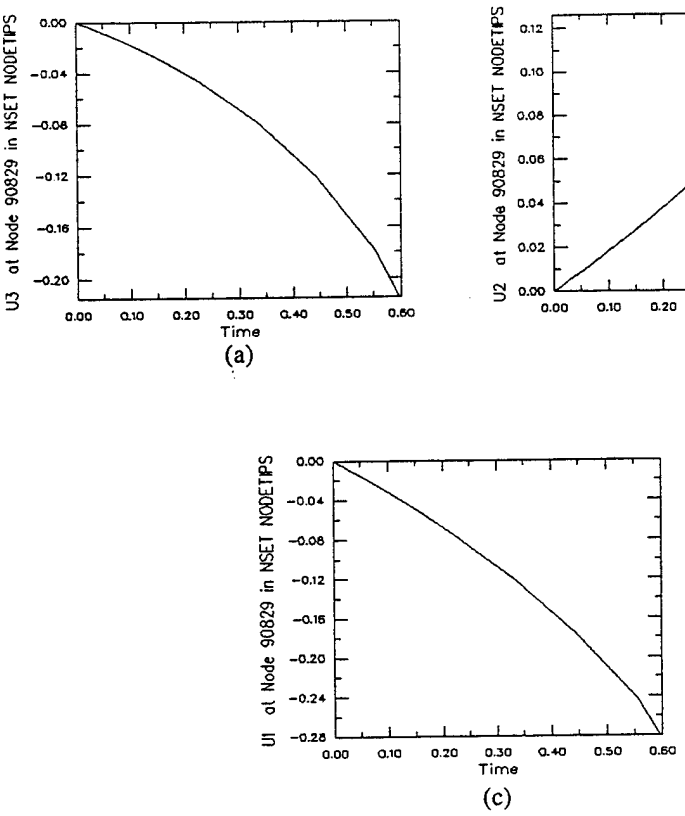

Figure 6.13 Displacement of medial extrusion at the specified fixed time increments in the simulation. (a) U3, (b) U2, and (c) U1.

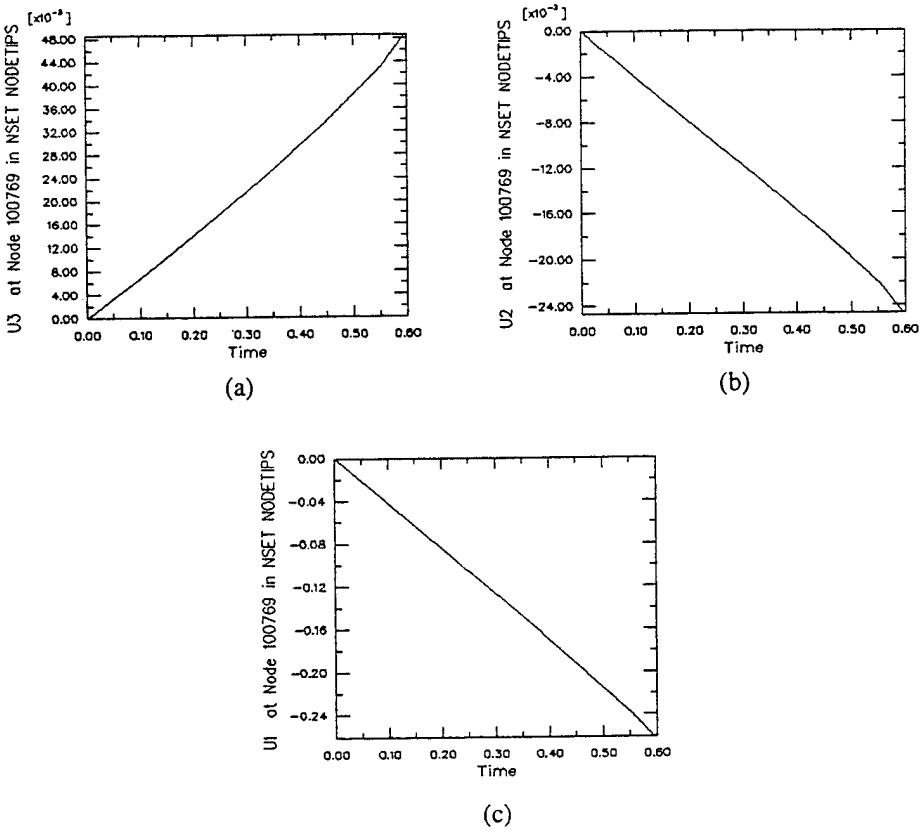

Figure 6.14 Displacement of center anterior extrusion at the specified fixed time increments in the simulation. (a) U3, (b) U2, and (c) U1.

The nodal displacement curves indicate that the S/I extrusion is displaced by amounts of -0.35, 0.032 and –0.20 in the 1,2, and 3 degrees of freedom. From the 3D MR data, the displacement for the corresponding voxel is –0.22, 0.108, and –0.13. The

strain in the direction of compression for each extrusion is given in figure 6.15. The negative values indicate that the strain is compressive, and not tensile.

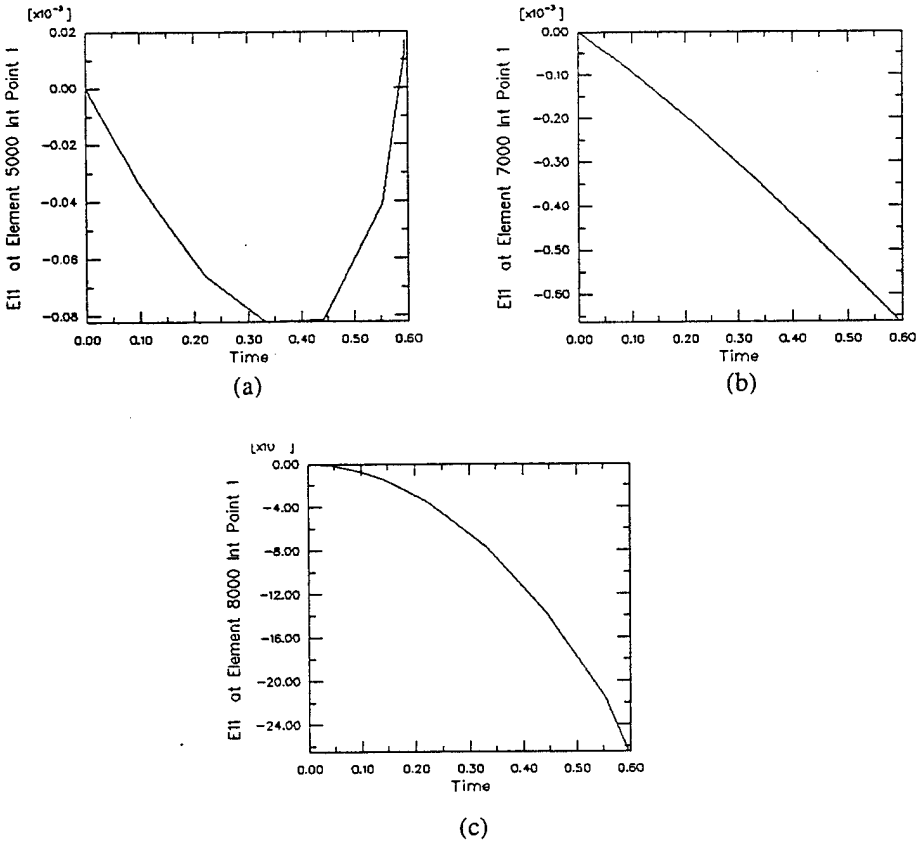

Figure 6.15 Axial strain in direction of compression of the extrusions at the specified fixed time increments in the simulation. (a) superior extrusion, (b) medial extrusion, and (c) anterior extrusion.

From the deformation studies discussed in chapter four, we found that MR imaging can provide quantitative *in vivo* biomechanical information about breast tissue subjected to incremental compressions. From the force sensors, measurements of the normal stress during static compression were obtained and the stress-strain curves evaluated were typical for soft tissue. With these experimental stress-strain data, a constitutive model of breast tissue undergoing mild static compressive deformation was approximated by incorporating the strain energy density function (SEDF) into the finite element modeling.

The FE computer simulations suggest that not only is the hyperelastic Mooney-Rivlin model a viable SEDF model for breast tissue, but the methods used to obtain the *in vivo* test data are also validated. The simulated deformations approximately correspond to the actual deformations, however a closer simulation can be obtained by simply varying the material parameters (*i.e.*, coefficients) of the SEDF hyperelastic model.

CHAPTER 7

CONCLUDING REMARKS

RESEARCH ACCOMPLISHMENTS

Some research accomplishments from this work are:

1. This initial investigation into the force-deformation behavior of normal breast tissue provides some of the first *in vivo* data on breast tissue under loading conditions similar to those occurring in diagnostic examinations.
2. Our results have been very encouraging in that we have demonstrated a viable method for obtaining *in vivo* deformation data suitable for studying the static mechanical properties of breast tissue.
3. We were able to observe substantial tissue deformations under the mildest of compressions. High resolution images can be obtained with MRI, and such images can be used to map tissue displacement.
4. Our data indicate that under static compressive loading, glandular breast tissue exhibits features similar to other connective soft tissues, such as skin and aorta.
5. We found that a hyperelastic, polynomial constitutive relationship provides a good fit to *in vivo* breast tissue. Such a relationship is described by the Mooney-Rivlin strain energy density function.

The information gained from the understanding of biomechanical behavior of *in vivo* tissue may serve as a diagnostic tool in surgery planning, computer aided diagnosis, and mammographic compression by making better breast models. Such models may be useful for predictive computer simulations of tissue displacement, assessing tissue changes in serial mammograms, and aiding elastography (i.e., remote palpation).

The finite element model, developed with the uniaxial experimental data, can be used to predict the mechanical deformations of breast tissue under various clinical procedures, such as the insertion of needles as in biopsy techniques.

The presentations and abstracts from this research are provided in the appendices

BIBLIOGRAPHY

ABAQUS, Ver.5.7, Hibbitt, Karlson & Sorensen, Inc., Pawtucket, RI, 1997.

Alexander, M., Somorjai, R., "The Registration of MR Images Using Multiscale Robust Methods", Magnetic Resonance Imaging, Vol. 14 (5), pp.453-468, 1996.

Almeida, E., Spilker, R., "Finite Element Formulations for Hyperelastic Transversely Isotropic Biphasic Soft Tissues", Computer Methods n Applied Mechanics and Engineering", Vol. 151, pp. 513-538, 1998.

Azar, F., Metaxas, D., Schnall, M., "A Finite Element Model of the Breast for Predicting Mechanical Deformations during Interventional Procedures", 1999 Proceedings of International Society For Magnetic Resonance in Medicine, 70th Scientific Meeting and Exhibition, 1999.

Bassett, L.,"Quality Determinants of Mammography: Clinical Image Evaluation", 81st Scientific Assembly and Annual Meeting of the Radiological Society of North America, RSNA Categorical Course in Breast Imaging, pp.57-68, 1995

Bookstein, Fred, Morphometric Tools for Landmark Data, Cambridge University Press, New York, 1991.

Boyd, N., Lockwood, G., Byng, J., Tritchler, D., Yaffe, M., "Mammographic Densities and Breast Cancer Risk", Cancer Epidemiology, Biomarkers and Prevention, Vol.7, pp.1133-1144, 1998.

Cardenosa, G., Eklund, G., "Breast Anatomy, Histology, and Cancer", 81st Scientific Assembly and Annual Meeting of the Radiological Society of North America, RSNA Categorical Course in Breast Imaging, pp.21-28, 1995.

Chakeres, D., Schmalbrock, P., Clymer, B., Deak, G., Williams, C., "MR Surface Coil Image Correction Using an Integrated Positional Reference System", Radiological Society of North America, 84th Scientific Assembly and Annual Meeting, Radiology,1998.

Chen, E., Alder, R., Carson, P., Jenkins, W., O'Brien, W., "Ultrasound Tissue Displacement Imaging with Application to Breast Cancer", Ultrasound in Medicine and Biology, Vol.21 (9), pp. 1153-1162, 1995.

Cespedes I., Ophir J., Ponnekanti H., Maklad N., " Elastography: elasticity imaging using ultrasound with application to muscle and breast in vivo.", Ultrasonic Imaging , Vol.15(2), pp.73-88, 1993.

Dixon, M, Sainsbury, R., Diseases of the Breast, Churchill Communications Europe Limited, 1998.

Eklund, G., "Tailoring the Mammographic Examination", 81st Scientific Assembly and Annual Meeting of the Radiological Society of North America, RSNA Categorical Course in Breast Imaging, pp.117-120, 1995

Evans, P. "Stereotaxic Fine-Needle Aspiration and Core Biopsy", 81st Scientific Assembly and Annual Meeting of the Radiological Society of North America, RSNA Categorical Course in Breast Imaging, pp.151-160, 1995.

Farshad, M., Barbezat, M., Flueler, P., Schmidlin, F., Graber, P., Niederer, P., "Material Characterization of the Pig Kidney in Relation with the Biomechanical Analysis of Renal Trauma", Journal of Biomechanics, Vol. 32, pp.417-425, 1998.

Fentimen, S., "Technical Report of the International Working Group on Breast Imaging", Journal of Magnetic Resonance Imaging, Vol. 10, pp. 979-981, 1999

Flickinger F., Allison, J., Sherry, R., and Wright, J., "Differentiation of Benign from Malignant Masses by Time-Intensity Evaluation of Contrast Enhanced MRI", Magnetic Resonance Imaging, Vol.11 (5), pp. 617-620, 1993.

Fowlkes JB, Emelianov SY, Pipe JG, Skovoroda, AR, Carson, PL, Adler, RS., Sarvazyan AP., " Magnetic-resonance imaging techniques for detection of elasticity variation.", Medical Physics, Vol.22(11 Pt 1), pp.1771-8, 1995.

Fujimura, K., Mararov, M., Fold-over Free Image Warping", Graphical Models and Image Processing, Vol. 60, pp.100-111, 1998.
Fung. Y.C., Biomechanics: Mechanical Properties of Living Tissues. Springer-Verlag, New York, 1993.

Fung, Y.C., A First Course In Continuum Mechanics. Prentice-Hall, New Jersey 1977.

Fung,Y.C., Biomechanics: Its Foundations and Objectives, Prentice-Hall, New Jersey, 1972.

Gallagher, R., Simon, B., Johnson, P., Gross, J., Finite Elements in Biomechanics, Wiley & Sons, New York, 1982.

Garra BS, Cespedes, EI., Ophir, J., Spratt SR, Zuurbier RA., Magnant, CM., Pennanen, MF., "Elastography of breast lesions: initial clinical results.", Radiology, Vol.202(1),pp.79-86, 1997.

Gordon, P., "US for Problem Solving in Breast Imaging: Tricks for the trade", 81st Scientific Assembly and Annual Meeting of the Radiological Society of North America, RSNA Categorical Course in Breast Imaging, pp.121-132, 1995

Gram, I., Funkhouser, E., Taber, L., "The Classsigication Scheme of Mammigraphic Parenchymal Patterns", European Journal of Radiology, Vol.24,pp. 131-136, 1997.

Greenstein, S., Schnall, M., Powell, C., Hochman, M., Solin, L., Fowble, B., Torosian, M., and Rosato, E., "Staging of Suspected Breast Cancer: Effect of MR Imaging and MR-guided Biopsy", Radiology, Vol. 196, pp 115-122, 1995.

Gribbstad, I., Nilsen, G., Fjosne, H., Kvinnsland, S., Haugen, O., and Rinck, P., "Comparative Signal Intensity Measurements in Dynamic Gadolinium-enhanced MR Mammography", Journal of Magnetic Resonance Imaging, Vol.4, pp.477-480, 1994.

Guo, J., Gai, Y., Wang, Y., "Morphology-Based Interpolation for 3D Medical Image Reconstruction", Computerized Medical Imaging and Graphics, Vol.19(3), pp.267-279, 1995.

Harms, S.E., Flaming, D.P., "MR Imaging of the Breast", Journal of Magnetic Resonance Imaging, Vol.3, p.277-283, 1993.

Harms, S., "Technical Report of the International Working Group on Breast Imaging", Journal of Magnetic Resonance Imaging, Vol. 10, pp. 979-981, 1999

Humphey, JD., YIN, FCP., "On Constitutive relations and Finite Deformations of Passive Cardiac Tissue: I. A pseudo strain-energy Function", Journal of Biomechanical Engineering, Vol.100, pp.299-304, 1993.

Ikelda, D, Birdwell, R., "Fine-Needle Aspiration in the Evaluation of the Nonpalpable Breast Lesion", 81st Scientific Assembly and Annual Meeting of the Radiological Society of North America, pp. 167-172, 1995.

Kaiser, W.A.,MR Mammography (MRM), Spinger-Verlag, New York, 1993.

Kopans, D., "The Etiology of Breast Cancer", 81st Scientific Assembly and Annual Meeting of the Radiological Society of North America ,RSNA Categorical Course in Breast Imaging, pp.29-38, 1995

Kopans, D., D'Orsi, C., Adler, D., Bassett, L., Brenner, R., Dodd, G., "American College of Radiology Breast Imaging Reporting and Data System (BI-RADS), Jefferson (VA), American College of Radiology, 1993.

Kruse, S., "Technical Report of the International Working Group on Breast Imaging", Journal of Magnetic Resonance Imaging, Vol. 10, pp. 979-981, 1999

Lawrence, R., Breastfeeding: A guide for the medical profession, 5th Edition, Mosby, St. Louis, 1999.

Liang, Z., Pan, H., Magin, R., Ahuja, N., Huang, T., "Automated Image Registration by Maximization of a Region Similarity Metric", International Journal of Imaging Systems Technology, Vol. 8, pp.513-518, 1997.

Lu, W., Fitchard, E., Olovera, G., You, J., Ruchala, K., Aldridge, J., Mackie, T., "Image/Patient Registration from (Partial) Projection data by the Fourier Phase Matching Method", Physics and Medical Biology, Vol.44, pp.2029-2048, 1999.

Mendis, K., Stalnaker, R., Advani, S., "A constitutive relationship for large deformation finite element modeling of brain tissue", Journal of Biomechanical Engineering, Vol. 117, pp. 279-285, August 1995.

Nahum, A., Melvin, J., Accidental Injury, Biomechanics and Prevention, Spinger-Verlag, New York, 1993.

Park, J., Lakes, R., Biomaterials, An Introduction, Plenum Press, New York, 1992.

Pecker, W., Schnorr, C., Rohr, K., Stiehl, H., "Parameter-Free Elastic Deformation Approach for 2D and 3D Registration Using Prescribed Displacements", Journal of Mathematical Imaging and Vision", Vol. 10, pp.143-162, 1999.

Piccart, M.J., "The Changing Landscape of Breast Cancer Clinical Research", Annals of Oncology, Vol. 9, pp.133-138, 1998.

Plewes, D., Bishop, J., Soutar, I., and Cohen, E., "Errors in Quantitative Dynamic Three-dimensional Keyhole MR Imaging of the Breast", Journal of Magnetic Resonance Imaging, Vol.5, pp.361-364, 1995.

Ponnekanti, H., Ophir, J., Cespedes, I., "Ultrasonic Imaging of the Stress Distribution in Elastic Media Due to an External Compressor", Ultrasound in Medicine and Biology, Vol. 20 (1) pp.27-33, 1994.

Ponnekanti, H., Ophir, J., Huang, Y., Cespedes, I., "Fundamental Mechanical Limitations on the Visualization of Elasticity Contrast in Elastography" Ultrasound in Medicine and Biology, Vol. 201(4) pp.533-543, 1995.

Porrath, Sarr, A Multimodality Approach to Breast Imaging, Aspen, Maryland, 1986.

Russell, D.G., Ziewacz, J.T., " Pressures in a Simulated Breast Subjected to Compression Forces Comparable to Those of Mammography", Radiology, Vol. 194(2), pp. 383-387, 1995.

Schmid-Schonbein, G. W., Woo, S., Zweifach, B., Frontiers in Biomechanics, Spinger-Verlag, New York, 1986.

Schnall, S., "Technical Report of the International Working Group on Breast Imaging", Journal of Magnetic Resonance Imaging, Vol. 10, pp. 982-990, 1999

Silver, F., Biological Materials: Structure, Mechanical Properties, and Modeling of Soft Tissue, New York University Press, New York, 1987.

Simonetti, G., Cossu, E., Montanaro, M., Caschili, C., Guiliani, V., "What's New in Mammography", European Journal of Radiology 27, pp. S234-S241, 1998.

Slauson, D., Cooper, B., Mechanisms of Disease, Williams & Wilkins, Baltimore, 1990.

Sullivan, D., Beam, C., Goodman, S., Watt, D., "Measurement of Force Applied during Mammography", Radiology, Vol. 181, pp. 355-357, 1991.

Sumi, C., Suzuki, A., Nakayama, K., "Estimation of Shear Modulus Distribution in Soft Tissue from Strain Distribution", IEEE Transactions on Biomedical Engineering, Vol. 2, No.2, pp.193-204, 1995.

Turkat, T., Klein, B., Polan, R., and Richman, R., "Dynamic MR Mammography: A Technique for Potentially Reducing the Biopsy Rate for Benign Breast Disease", Journal of Magnetic Resonance Imaging, Vol.4, pp.563-568, 1994.

Twizell, E., Ogden, R., "Non-Linear Optimization of the Material Constants in Ogden's Stress-Deformation Function for Incompressible Isotropic Elastic Materials", Journal of Australian Mathematics Society, Ser. (B), pp. 424-434, 1983.

Watmough, D.J., Quan, K.M., Aspden, R.M., "Breast Compression: A Preliminary Study", Journal of Biomedical Engineering, Vol.15, pp.121-126, 1993.

Westbrook, C., Kaut, C., MRI in Practice, Blackwell Scientific Publications, Cambridge, MA, 1993.

Wood, W.C., "Surgical Excision Versus Minimally Invasive Techniques", 81st Scientific Assembly and Annual Meeting of the Radiological Society of North America, RSNA Categorical Course in Breast Imaging, pp.173-174, 1995

Williams, C., Clymer, B., Schmalbrock, P., "Biomechanics of Breast Tissue: Preliminary studies into force-deformation relationship", International Society For Magnetic Resonance in Medicine, 70th Scientific Meeting and Exhibition, 1999.

Vito, R, "A Note On Arterial Elasticity", Journal of Biomechanics, Vol.6, pp. 561-564, 1973.

APPENDICES

Appendix A Acronyms

Appendix B Computer Programs

Appendix C MRI Exams

A. ACRONYMS AND SYMBOLS

T - tesla

TR - repetition time

TE - echo time

T1- spin-lattice relaxation time of the magnetization along the longitudinal axis

T2- spin-spin relaxation time of magnetization in the transverse plane.

ETL - echo train length

sec - second

ms - millisecond

mm - millimeter

FSE - fast spin echo

2D - two dimensional

3D - three dimensional

SNR - signal-to-noise ratio

SPGR- spoiled gradient echo

C-C - cranio-caudal

M-L - medial-lateral

A/P - anterior-posterior

S/I - superior-interior

Deformation - $L_o - L / L_o$

L - undeformed length

L_o - Deformed length

N - Newton

Pa - Pascal (N/m^2)

kPa – 10^3 Pascal

B. COMPUTER PROGRAMS

B1. IDL PROGRAMS

PROGRAM TO READ IN MR FILE AND PERFORM INTENSITY CORRECTION

```
; TEST PROGRAM
PRINT,'PROGRAM TO READ BREAST FILE, STANDARD XIMG'
PRINT,'START IMAGE I.., END IMAGE I.., SKIP NUMBER '
READ,N1ST,NLAST,SKIP
PRINT,'PROGRAM TO READ PHANTOM FILE, STANDARD XIMG'
PRINT,'START IMAGE I.., END IMAGE I.., SKIP NUMBER '
READ,FST,LAST,SP
N1ST=FIX(N1ST) & NLAST=FIX(NLAST) & SKIP=FIX(SKIP)
FST=FIX(FST) & LAST=FIX(LAST) & SP=FIX(SP)
ROWS=512
COLS=512
NTIME=(NLAST-N1ST+1)/SKIP
NTIME2=(LAST-FST+1)/SP
A=BYTARR(532192)
H=INTARR(8)
IM=INTARR(COLS,ROWS)
IMS=INTARR(COLS,ROWS,NTIME)
IMS2=INTARR(COLS,ROWS,NTIME2)
;MR FILE
BFILE = '/USR/PEOPLE/CELESTE/IDL/'
PREFIX = 'E3032S2I'
SUFFIX1 = '.MR'
;CORRESPONDING PHANTOM SLICE FOR CORRECTION
PFILE = '/USR/PEOPLE/CELESTE/IDL/'
PREFIX1 = 'E29083S3I'
SUFFIX = '.MR'
J=0
FOR I=N1ST,NLAST,SKIP DO BEGIN
 FILE1=BFILE+PREFIX+STRCOMPRESS(STRING(I),/REMOVE_ALL)+SUFFIX1
 OPENR,1,FILE1
 READU,1,A          ;A=ALL DATA HEADER AND IMAGE
 CLOSE,1
 OPENR,1,FILE1      ;H=HEADER INFO, H(3) HEADER LENGTH
 READU,1,H
 CLOSE,1
 IM=FIX(A,H(3),COLS,ROWS)
```

```
 IM=ROTATE(IM,7)
 IMS(*,*,J)=IM(*,*)
 PRINT,'DONE READING IMAGE ', FILE1
 PRINT,'IT WAS PLACED INTO IMS(*,*,J), J= ',J
J=J+1
ENDFOR

L=0
FOR K=FST,LAST,SP DO BEGIN
 FILE2=PFILE+PREFIX1+STRCOMPRESS(STRING(K),/REMOVE_ALL)+SUFFIX
 OPENR,1,FILE2
 READU,1,A          ;A=ALL DATA HEADER AND IMAGE
 CLOSE,1
 OPENR,1,FILE2      ;H=HEADER INFO, H(3) HEADER LENGTH
 READU,1,H
 CLOSE,1
 IM=FIX(A,H(3),COLS,ROWS)
 IM=ROTATE(IM,7)
 IMS2(*,*,L)=IM(*,*)
 PRINT,'DONE READING IMAGE ', FILE2
 PRINT,'IT WAS PLACED INTO IMS2(*,*,L), L=',L
L=L+1
ENDFOR

FF=N1ST
; DO CORRECTION
FOR TT= 0,J-1,1 DO BEGIN
        BR=IMS(*,*,TT)
        PH=IMS2(*,*,TT)
        PH=ROTATE(PH,90)
        PHS=SHIFT(PH,10,10); SHIFT THE PHANTOM SO THAT POINTS ALIGN IF NECESSARY
        TVSCL,BYTSCL(PHS+BR, MIN=0,MAX=150)
        MBR=BR GE 10
        MPH=PHS GE 5
        MASK=MBR*MPH
        CBR=BR*MASK+1-MASK
        CPH=PHS*MASK+1-MASK
        FPH=SMOOTH(CPH,5); SMOOTH THE PHANTOM
        TTEMP=MASK*CBR*1.0/FPH
        FINAL=BYTSCL(TTEMP,MIN=0,MAX=2.5)
        ; SEGMENT OUT THE DATA
        ;IMM=FINAL
        ;IMM=(IMM LE 170) AND (IMM GE 0)
        ;HH=BYTSCL(BR,MIN=0,MAX=35)
        ;HHH=2*HH
        ;IMG=IMM*FINAL
        ;TVSCL,IMG
        ;IMG(340:511,*)=0 ; REMOVE X-SIDE
        ;IMG(0:175,*)=0
        ;IMG(*,0:120)=0 ; REMOVE Y-SIDE
        ;IMG(*,375:511)=0
        ; EXTERNAL LANDMARK IF NECESSARY
```

```
        ;IMG(182:192,190:213)=0
        ;TVSCL,IMG
        ;IMAGE=REBIN(IMG,256,256)
        ; WRITE THE SEGMENT DATA TO A FILE
        ;FILENAME= 'E321_UN'
        ;SUFFIX = '.'
        ;FF=N1ST+1
        ;F_SEG=FILENAME+SUFFIX+STRCOMPRESS(STRING(FF),/REMOVE_ALL)
        ;OPENW,1,F_SEG
        ;WRITEU, 1, IMG
        ;CLOSE,1
        FF=FF+1
ENDFOR
END
```

SEDF CURVE FITTING PROGRAMS

```
; FITTING CURVES
;SEDF MODELS FOR 3 EXAMS
;EXAM 37840 (BIN)
STRAIN=[0.0,3.03,5.56,5.88,8.11,8.7,9.3,11.3,12.2,12.96,15.56,16.67,18.5,18.6,19.15,19.23,21.28,21.6,2
2.2,23.26,24.5,27.9,28.89,30.43,31.1,32.08,32.6,33.3,34.15,34.88,36.17,36.61,37.04,38.3,38.46,41.15]
STRESS=[1.89,1.30,0.989,1.66,2.83,0.542,2.34,3.54,3.74,3.41,4.0,3.33,3.68,3.13,4.0,3.97,3.90,7.01,3.97,
6.01,4.02,7.68,9.28,2.40,9.08,8.48,5.28,8.24,8.47,8.65,9.17,5.38,8.74,8.89,9.24,9.27]
; EXAM 3032
STRAIN1=[0.0,2.86,3.85,4.76,5.71,6.25,7.69,7.89,9.68,11.11,11.54,12.82,14.29,15.38,15.91,18.92,22.22,
25.0,28.57,29.03,29.55,29.73,30.56,30.77,30.95,33.33,34.21,38.1,38.46,41.46,43.24,56.10]
STRESS1=[0.989,1.639,3.08,1.63,1.64,0.345,0.45,1.64,1.56,1.4,0.79,1.41,1.47,1.2,1.57,1.515,2.69,1.68,5.
59,5.41,5.3,1.63,4.96,2.0,5.16,4.98,5.60,5.59,4.35,1.405,5.28,5.44]
;EXAM 3033
STRAIN2=[0.0,3.03,7.69,8.70,10.81,14.0,16.0,17.65,20.45,20.51,21.21,23.81,24.32,25.58,30.77,31.58,32.
0,33.33,34.09,35.9,36.0,37.5,39.53,40.0]
STRESS2=[0.989,0.3949,0.0771,3.067,4.025,0.472,0.4835,0.4909,0.4956,0.4968,3.645,0.2665,0.4296,0.4
975,0.7534,0.118,4.2815,4.7334,4.84,4.8169,4.6396,2.736,4.844,1.9078]
;FIND THE RATIOS
STR=STRAIN/100.0
RATIO=1.0-STR
STR1=STRAIN1/100.0
RATIO1=1.0-STR1
STR2=STRAIN2/100.0
RATIO2=1.0-STR2
;DEFINE THE PARAMETERS
XTHEO=INDGEN(100)/99.0
;X=XTHEO
X=RATIO; EXAM 38740
;X=RATIO1; EXAM 3032
;X=RATIO2; EXAM3033
; MR MODEL COEFFICIENTS FOR THE 3 EXAMS
A=[-4.60561,1.59226];E38740
;A=[-2.282.,0.81317];E3032
;A=[-0.744956,0.460954];3033
KXX=(-1/X^2) + X
```

```
K11= 1-(1/X^3)
BB=A(1)
FMR = 2*((A(0)*KXX)+(A(1)*K11))
; BLATZ MODEL
B=[-3.97686,-0.073017]
;B=[-1.55721,-0.39737]
;B=[-0.667833,-1.19420]
KX=-1 + X^2
K1=-1 + (1/X)
P1=EXP(B(1)*KX)
P2=EXP(B(1)*K1)
FBL = (B(0)/(B(1)+1))*((X*P1)-(P2/X^2))
;VITO MODEL
C=[-3.98766,1.34164,-0.600936]
;C=[1.67581,-1.53656,0.517927]
;C=[-0.0693182,-2.20366,2.96975]
I1=(2/X)+X^2
I2=2*X+(1/X^2)
V1=I1-3
V2=I2-3
KV=X-(1/X^2)
EE=EXP((C(1)*V1)+(C(2)*V2))
FVITO=2*C(0)*KV*(C(1)+(C(2)/X))*EE
;ODGEN MODEL
D=[-3.97906,2.14108]
;D=[-1.54160,1.84994]
;D=[-0.22969,3.4792]
X11= X^(D(1)-1)
EP=(-2.0-D(1))/2.0
X22= X^(EP)
FOGD=((2.0*D(0))/D(1))*(X11-X22)
;EXAMPLES OF PLOTS
PLOT,X,FOGD
OPLOT,RATIO,STRESS,PSYM=1
END
```

SEDF FUNCTIONS WITH THE PARTIAL DERIVATIVES WITH RESPECT TO THE COEFFICIENTS.

```
;BLATZ MODEL
PRO FUNCT, X, A, F, PDER
  KXX=-1 + X^2
  K11=-1 + (1/X)
  B=A(1)+1
  P1=EXP(A(1)*KXX)
  P2=EXP(A(1)*K11)
  F = (A(0)/(A(1)+1))*((X*P1)-(P2/X^2))
   IF N_PARAMS() GE 4 THEN BEGIN
   PDER = FLTARR(N_ELEMENTS(X), 2)
   PDER[*,0]= ((X*P1)/B) - (P2/(B*X^2))
```

```
  PDER[*,1]=(-(A(0)*X*P1)/B^2)+((A(0)*X*KXX*P1)/B)+((A(0)*P2)/((X^2)*(B^2)))-
((A(0)*K11*P2)/(B*X^2))
 ENDIF
END

; MOONEY_RIVLIN MODEL
PRO FUNCT, X, A, F, PDER
 KXX=X-(1/X^2)
 K11= 1 - (1/X^3)
 B=A(1)
 ;P1=EXP(A(1)*KXX)
 ;P2=EXP(A(1)*K11)
 F = (2*A(0)*KXX)+(2*A(1)*K11)
  IF N_PARAMS() GE 4 THEN BEGIN
  PDER = FLTARR(N_ELEMENTS(X), 2)
  PDER[*,0]= 2*KXX
  PDER[*,1]= 2*K11
 ENDIF
END


;ODGEN SEDF MODEL
PRO FUNCT, X, A, F, PDER
  X11= X^(A(1)-1)
  EP=(-2.0-A(1))/2.0
  X22= X^(EP)
  F=((2.0*A(0))/A(1))*(X11-X22)
  FTERM=(ALOG(X)/A(1))*(X11+(0.5*X22))
  STERM=(X22-X11)/(A(1)^2)
  IF N_PARAMS() GE 4 THEN BEGIN
  PDER = FLTARR(N_ELEMENTS(X),2)
  PDER[*, 0]= (2.0/A(1))*(X11-X22)
  PDER[*, 1]=2.0*A(0)*(FTERM+STERM)
  ENDIF
END

;VITO SEDF MODEL
PRO FUNCT, X, A, F, PDER
 KV= X-(1/X^2)
 I1=(2/X)+X^2
 I2=2*X+(1/X^2)
 K1=I1-3
 K2=I2-3
 EE=EXP((A(1)*K1)+(A(2)*K2))
  F=2*A(0)*KV*(A(1)+(A(2)/X))*EE
  IF N_PARAMS() GE 4 THEN BEGIN
  PDER = FLTARR(N_ELEMENTS(X), 3)
  PDER[*, 0]= 2*KV*(A(1)+(A(2)/X))*EE
  PDER[*, 1] = 2*A(0)*KV*EE*((A(1)*K1)+1+(K1*(A(2)/X)))
  PDER[*, 2] = 2*A(0)*KV*EE*((A(1)*K2)+((A(2)/X)*K2)+(1/X))
 ENDIF
END
```

B2. VTK Program

VOLUME RENDERER

```
CATCH {LOAD VTKTCL}
# GET THE INTERACTOR UI
SOURCE C:/VTK/EXAMPLESTCL/VTKINT.TCL
SOURCE C:/VTK/EXAMPLESTCL/COLORS.TCL

# CREATE THE RENDERWINDOW, RENDERER AND BOTH ACTORS
#
VTKWORLDPOINTPICKER PICK
VTKRENDERER REN1
VTKRENDERWINDOW RENWIN
  RENWIN ADDRENDERER REN1
VTKRENDERWINDOWINTERACTOR IREN
  IREN SETRENDERWINDOW RENWIN
  IREN SETPICKER PICK
# CREATE PIPELINE
#
VTKVOLUME16READER V16
V16 SETDATADIMENSIONS 256 256
[V16 GETOUTPUT] SETORIGIN 0.0 0.0 0.0
V16 SETDATABYTEORDERTOBIGENDIAN
V16 SETFILEPREFIX "C:/VTK/MRI/MRDATA/E321_UN"
V16 SETIMAGERANGE 35 99
V16 SETDATASPACING 0.8 0.8 0.7
V16 UPDATE

VTKMARCHINGCUBES ISO
ISO SETINPUT [V16 GETOUTPUT]
ISO COMPUTEGRADIENTSOFF
ISO COMPUTENORMALSOFF
ISO SETVALUE 0 300.5

VTKDECIMATE DECIMATOR
  DECIMATOR SETINPUT [ISO GETOUTPUT]
  EVAL DECIMATOR SETINITIALFEATUREANGLE 60
  EVAL DECIMATOR SETMAXIMUMITERATIONS 5
  DECIMATOR SETMAXIMUMSUBITERATIONS 0
  DECIMATOR PRESERVEEDGESON
  DECIMATOR SETMAXIMUMERROR 1
  DECIMATOR SETTARGETREDUCTION .95
  EVAL DECIMATOR SETINITIALERROR 0.002
  EVAL DECIMATOR SETERRORINCREMENT 0.002

VTKSMOOTHPOLYDATAFILTER SMOOTHER
  SMOOTHER SETINPUT [DECIMATOR GETOUTPUT]
  EVAL SMOOTHER SETNUMBEROFITERATIONS 5
  EVAL SMOOTHER SETRELAXATIONFACTOR 0.1
  EVAL SMOOTHER SETFEATUREANGLE 60
  SMOOTHER FEATUREEDGESMOOTHINGOFF
```

```
  SMOOTHER BOUNDARYSMOOTHINGOFF;
  SMOOTHER SETCONVERGENCE 0

VTKPOLYDATACONNECTIVITYFILTER CONNECT
CONNECT SETINPUT [SMOOTHER GETOUTPUT]
CONNECT SETEXTRACTIONMODETOLARGESTREGION

VTKPOLYDATANORMALS NORMAL
NORMAL SETINPUT [CONNECT GETOUTPUT]
EVAL NORMAL SETFEATUREANGLE 60

VTKSTRIPPER STRIP
STRIP SETINPUT [NORMAL GETOUTPUT]

VTKPOLYDATAMAPPER ISOMAPPER
ISOMAPPER SETINPUT [STRIP GETOUTPUT]
ISOMAPPER SCALARVISIBILITYOFF

VTKACTOR ISOACTOR
ISOACTOR SETMAPPER ISOMAPPER
EVAL [ISOACTOR GETPROPERTY] SETCOLOR $CORAL
EVAL [ISOACTOR GETPROPERTY] SETDIFFUSE 2.0
EVAL [ISOACTOR GETPROPERTY] SETSPECULAR 0.05
EVAL [ISOACTOR GETPROPERTY] SETSPECULARPOWER 5


# ADD THE ACTORS TO THE RENDERER, SET THE BACKGROUND AND SIZE
#
#REN1 ADDACTOR ISO2ACTOR
REN1 ADDACTOR ISOACTOR
REN1 SETBACKGROUND 1 1 1
RENWIN SETSIZE 300 300


# RENDER THE IMAGE

RENWIN RENDER
IREN SETUSERMETHOD {WM DEICONIFY .VTKINTERACT}
#
# VTKPOLYDATASTLWRITER WRITE
# WRITE SETFILENAME "UNC.STL"
# WRITE SETINPUT [NORMAL GETOUTPUT]
# WRITE UPDATE

#RENWIN SETFILENAME "MCUBES.TCL.PPM"
#RENWIN SAVEIMAGEASPPM

# PREVENT THE TK WINDOW FROM SHOWING UP THEN START THE EVENT LOOP
WM WITHDRAW .
```

B3. ABAQUS Programs

```
SIMPLE MESH WITH MEMBRANE ELEMENTS
* heading
skin deformation
** inclusion with two meshes,without contact
*node,nset=ends,system=r
1, 4.,0.,0.
101,4.,0.,2.
5011,2.,10.,0.
5111,2.,10.,2.
2001,5.,0.,0.
2101,5.,0.,2.
7011,7.,10.,0.
7111,7.,10.,2.
**skin
*ngen,nset=lhs
1,101,10
*ngen,nset=rhs
2001,2101,10
*ngen,nset=rhs2
7011,7111,10
*ngen,nset=lhs2
5011,5111,10
*nfill,nset=front
lhs,rhs,10,200
*nfill,nset=rsnodes
rhs,rhs2,10,501
*nfill,nset=lsnodes
lhs,lhs2,10,501
**
**back nodes
*nfill,nset=back
lhs2,rhs2,10,200
** fatty tissue nodes
*nfill,nset=midnodes
lsnodes,rsnodes,10,200
**
** adipose elements*
*element,type=C3D8RH
5001,1,201,702,502,11,211,712,512
5601,1201,1401,1902,1702,1211,1411,1912,1712
*elgen,elset=adipose1
5001,10,10,10,4,200,100,10,501,1000
*elgen,elset=adipose2
5601,10,10,10,4,200,100,10,501,1000
*elset,elset=adipose
adipose1,adipose2
*solid section,elset=adipose,material=fatty
*material,name=fatty
*hyperelastic,n=1,ogden
```

```
0.16365,2.6526,0.0
**
** glandular inclusion
*element,type=C3D8RH
5401,801,1001,1502,1302,811,1011,1512,1312
*elgen,elset=inclusion
5401,10,10,10,2,200,100,10,501,1000
*solid section,elset=inclusion,material=gland
*material,name=gland
*hyperelastic,n=1,ogden
1.372,1.607,0.0
**
** tumor
*elset,elset=lesion
10441,10451
*solid section,elset=lesion,material=tumor
*material,name=tumor
*hyperelastic,n=1,ogden
4.0,3.0,0.0
**
*element,type=M3D4R
1,1,201,211,11
1001,2001,2502,2512,2011
3000,1,502,512,11
*elgen,elset=areola
1,10,10,10,10,200,100
*elgen,elset=rside
1001,10,10,10,10,501,100
*elgen,elset=lside
3000,10,10,1,10,501,100
*elset,elset=skinall
areola,rside,lside
*membrane section,elset=skinall,material=skin
0.25
*material,name=skin
*elastic
0.30,0.43
*boundary
lsnodes,1
rsnodes,2,3
back,2
*initial conditions, type=stress
rside, 0.5,0.5
areola,0.5,0.5,1.0
lside,-1.0,-1.0
adipose,0.25,0.25
**inclusion,0.25,0.25
**lesion,0.25,0.25
** step 1
*restart,write
*step,nlgeom,inc=50
*static
```

```
1.e-18,1.0
**0.05,1.0,0.01,0.2
*dload
rside,p,-2.
**lside,bx,-5000.
*energy print
*el print,elset=areola,position=averaged at nodes,summary=yes
s,e
NE
s11,e11
*node print,nset=rsnodes
u,rf
*output,field
*element output,elset=lesion
s,e
*node output
u,rf
*output, history,frequency=1
*node output, nset=rsnodes
u
*element output,elset=lesion
s,e
*end step
```

COMPLEX TISSUE MODEL

```
* heading
glandular deformation
*node, nset=ends,system=r
21,6.7,0.14,3.7
1021,6.83,8.86,0.498
61,7.26,0.048,0.002
1061,7.0,8.8,0.023
31041,8.65,9.04,0.794
30041,8.66,0.066,3.9
30081,11.55,0.41,0.59
31081,8.45,8.88,0.1
** read in cooedinate file
*read "file.inp"
**make extrusion nodes
*node,nset=nodetips,system=r
40021,6.98,9.5,0.45
40061,7.0,9.6,0.023
52029,7.2,9.35,0.476
52069,7.2,9.35,0.073
70037,7.69,9.27,0.80
73039,7.79,9.27,0.80
70077,7.76,9.43,0.35
73079,7.86,9.43,0.35
```

```
60823,7.19,7.36,2.33
60723,7.19,6.9,2.65
90829,7.7,7.66,2.65
90729,7.7,6.9,2.65
100769,10.07,6.183,2.0
100773,10.08,6.183,1.8
100669,10.3,5.498,1.304
100673,10.3,5.498,1.104
**left side end nodes
*ngen,nset=left1
21,321,50
*ngen,nset=left2
321,1021,50
*nset,nset=left
left1,left2
*ngen,nset=lhs2
61,1061,50
**right side end nodes
*ngen,nset=rig1
30041,30341,50
*ngen,nset=rig2
30341,31041,50
*nset,nset=rig
rig1,rig2
*ngen,nset=rhs2
30081,31081,50
**
**fill side nodes
*nfill,nset=lsnodes
left,lhs2,20,2
*nfill,nset=rsnodes
rig,rhs2,20,2
**
**middle nodes
*nfill,nset=midnodes
lsnodes,rsnodes,20,1501
**
**center front nodes
*ngen,nset=leftcen
321,15331,1501
*ngen,nset=rigcen
15331,30341,1501
*ngen,nset=midcen
15331,16031,50
**
**front nodes
*nset,nset=top
leftcen,rigcen
*ngen,nset=bottom
21,30041,1501
*nfill,nset=leftfront
left2,midcen,10,1501
```

```
*nfill,nset=rigfront
midcen,rig2,10,1501
*nfill,nset=areola
bottom,top,6,50
**back nodes
*nfill,nset=back
lhs2,rhs2,20,1501
**
**tissue elements
*element,type=c3d8rh
1,21,3023,3027,25,121,3123,3127,125
*elgen,elset=tissue
1,10,3002,1,10,100,10,10,4,100
**
**
**make extrusions
*ngen,nset=el1
1021,40021,19500
*ngen,nset=el2
1061,40061,19500
*ngen,nset=er1
13029,52029,19500
*ngen,nset=er2
13069,52069,19500
*nfill,nset=elhs
el1,el2,2,20
*nfill,nset=erhs
er1,er2,2,20
*nfill,nset=tip1
elhs,erhs,2,6004
** extrusion elements
*element,type=c3d8rh
3000,1021,7025,7045,1041,20521,26525,26545,20541
5000,16031,19033,19073,16071,70037,73039,73079,70077
7000,60723,90729,12729,6725,60823,90829,12829,6825
8000,30669,100669,100673,30673,30769,100769,100773,30773
*elgen,elset=extip1
3000,2,6004,1,2,19500,10,2,20,100
**make element set
*elset,elset=extips
5000,7000,8000,extip1
*elset,elset=alltiss
tissue,extips
*elset,elset=rside,generate
10,910,100
20,920,100
40,940,100
30,930,100
50,950,100
60,960,100
70,970,100
80,980,100
```

```
90,990,100
100,1000,100
*solid section,elset=alltiss,material=gland
*material,name=gland
*hyperelastic,n=1,ogden
3.963,2.6606,0.03823
*boundary
lsnodes,1
rsnodes,2,3
**back,1,3
**initial conditions,type=stress
**STEP 1
*restart,write
*step,nlgeom,inc=50
*static
1.0e-8,1.0
*dload
rside,p4,-2.0
*energy print
*el print, position=averaged at nodes, summary=yes
s11,e11
nep
dgp
*EL FILE
S,E
NEP
*NODE PRINT
U,RF
*NODE FILE,FREQUENCY=2
U,RF
*output,field
*element output,elset=rside
S
E
*node output,nset=rsnodes
U,RF
*output,history,frequency=1
*node output,nset=rsnodes
u,rf
*element output,elset=rside
s,e
*end step
```

C. MRI EXAMS

TABLE C1 List of MR Imaging

Exams	Date	Disk	Seq.	Purpose	Results
E27300	1/17/97	47B		Identify external markers	Signal voids
E22798	2/8/97	39B	1	Breath hold imaging with body coil to reduce supine artifacts	16 Fov too small so increased to 24. Images improved.
E22430	5/4/97	41A	2	Using breast coil to develop optimal protocol	Studied 2D SE,IR,SPGR
E22431	5/4/97	41A	3	Made TR longer to get all slices in a single pass	More SNR
E22432	5/4/97	41A	4		
E22433	5/4/97	41A1		Identify external landmarks	Nail polish seen but fairly large and dark thus not ideal for automatic detection
E23071	?	42A	5	Tests of various fast sequences .for breast imaging	Spgr better sequence. For the SE seq. a TE=30 is good.
E23072	?	42B	6	Tests of fast seq.	
E26370	12/2/97	46A	7		
E28536	3/20/98	49B	8	Magic box	
E28537	3/21/98	49A	9	Compressed and uncompressed imaging with CC device	Using breast coil
E28534	3/21/98	49A	10	Compressed/Unc	Slice thickness decreased from 2 to 1.4
E28434	3/21/98	49A	11	Compressed/Unc	Better images using 60 degrees and 1.4 thickness
E28723	3/23/99	49B		Phantom	
E29083	4/18/98	49		Phantom, played with TR to get rid of noise	Better low noise phantoms
E29082	4/18/98	49		Phantoms	
E29234	4/25/98	49B	12	HR images for segmentation	Uncompressed
E29235	4/25/98	49B	12	HR images for segmentation	Compressed with 3.5 inch spacer
E32190	9/20/98	52A	13	Deformation study	Smaller compressions
E32192	9/20/98	52	10	Phantom force study	Placement of sensors
E32930	10/25/98	52B	10	Deformation of markers	
E32931	10/25/98	52B	14	Breath hold study	
E33058	10/31/98	48A	10	Bread matrix phantom with markers	Obtained Rigid transformations

E28965		49A		Magic coil with prosthesis	
E30189	6/14/98	51		Testing of sensor artifacts	Large artifacts near the connector end (2 cm)
E34330	1/9/99	53B	10	Force compression data	Used 2 sensors
E35861	3/23/99	55B	10	Force compression data with sensor switch	Caused to much drift of signal
E3032	4/99	Zip	10	Force compression data	Multiple sensors
E3033	4/99	Zip	10	Force compression data	Multiple sensors
E38740	8/99	55B	10	Force compression data	Multiple sensors

TABLE C1 List of MR Imaging

Sequences

1. 3DFGRE, TR 14 msec, TE 2.8 msec, 20 degrees, BW 32, matrix, 512x128, FOV 32 x 16,scan time 30 secs. Breath hold for only 15 secs,

2. 2DFSE, fat sat., TR=7000,TE=102, 16 degrees, matrix 256 x192, FOV 20 x 20, thickness 5, NEX =2, time=5:36-------- 2DFSGPR, TR=11.2, TE= 4.2, 25 degrees, NEX=4, time=2:37. (coronal and sagittal)

3. Sagittal 2DSE with axial localizer, TR=700, TE=11, BW = 32, 512 X 256, FOV 20,, time=3:09. 1 pass

4. 2DSE, (SAME AS 3) 2 passes

5. SE-fast, TR=700, TE= 90, 60, 30, FOV = 16 x16, 36,18, PFOV=1, interleave=0, acq matrix= 128. ------ 3DSPGR-fast, TR=min, TE=in-phase: ----- IR-fast, TI=150 AND 30

6. IR-fast, TE=min, T1=160, fat sat.------EFGRE 3D, min TR min TE, FOV 16------ SIMCAST

7. 3d-fast gre, TR and TE min, 25 degrees, BW = 16, FOV=20, 512 x 256.

8. 3 inch coil, CC device

9. 3D FSPGR, TR=100, TE=4.2 in phase, 60 degrees, coronal orientation ,TR=25, zip2, time 6:50

10. SAME AS 9

11. 3Dgre-fast, TE=4.2, 25 degrees---------3D SPGR, 40, 60 degrees, thickness 1.5 AND 1.4.

12. 3DSPGR, TE in-phase, FOV 20, 15 degrees, TR=25, time=13:10---- for maximal contrast.

13. 3D SPGR, TR=45, angle=60, time = 12:18, spacers 4.5, 4.0, 3.75, 3

14. efgre 3D, TR min, TE min, angle 45, FOV 28 x 14

Segmentation Issues - less contrast with the surface coil.
Intensity correction algorithm increased noise so obtained better phantom images using shorter flip angle.

TABLE C2 Data of Signal Contrast Using FSPGR Sequence				
θ	max S_{tissue}	max S_{fat}	TR (msec)	T1 (msec)
15	0.1368	0.2029	35	800 for gland, 300 for fat
20	0.1572	0.2403	40	
20	0.2493	0.2491	45	
15	0.1248	0.1856	25	
60	0.05173	0.1283	25	

TABLE C2 Data of Signal Contrast Using FSPGR Sequence

The first data set was obtained using flip angle = 60, and TR=25
This gives a ratio of

$$\max S_{fat} / \max S_{tissue} = 2.48$$

For these set of images the contrast was low, but the acquisition time was under seven minutes.

With a new imaging technique using flip angle $15 <= \theta <= 25$ and TR =25, the imaging time is under 14 minutes, but the phantom images were less noisy. The signal ratio is 1.48. Signal is greater using GRASS sequence, as θ increases, the signal increases.

APPENDIX D

PUBLICATIONS/PRESENTATIONS

1. Williams, C., Clymer, B., Schmalbrock, P., *"Biomechanics of Normal Breast Tissue: Preliminary study of in vivo force-deformation relationship"* ,submitted to Journal of Biomechanics, June 2000.

2. Williams, C., Clymer, B., Schmalbrock, P., *"Biomechanics of Normal Breast Tissue: Preliminary study of in vivo force-deformation relationship"*, Poster at DoD Era of Hope Breast Cancer Conference, June 2000.

3. Williams, C., Clymer, B., Schmalbrock, P., "*Biomechanics of Breast Tissue: Tissue deformation and visualization"*, Presentation at 1999 Proceedings of 70th Scientific Meeting and Exhibition of the International Society for Magnetic Resonance in Medicine, May 1999.

4. Williams, C., Clymer, B., Fujimura, K., Schmalbrock, P., "*Preliminary Study of Shape Deformation of Normal Breast Tissue"*, ", Poster at 84th Scientific Assembly and Annual Meeting of the Radiological Society of North America, p.524, April 1998.

5. Williams, C., Clymer, B., Fujimura, K., Schmalbrock, P., "*Preliminary Study of Shape Deformation of Normal Breast Tissue"*, Presentation at 1998 Annual Fall Meeting of the Biomedical Engineering Society, October 1998.

6. Williams, C., Clymer, B., Schmalbrock, P., "*Preliminary Study of Shape Deformation of Normal Breast Tissue"*, Poster at Women's Health Conference, The Ohio State University, 1997.